Development and Application of Technologies for Liquid Manipulation on Droplet Microarrays

Zur Erlangung des akademischen Grades eines

DOKTORS DER NATURWISSENSCHAFTEN
(Dr. rer. nat)

von der KIT-Fakultät für Chemie und Biowissenschaften
des Karlsruher Instituts für Technologie (KIT)

genehmigte

Dissertation

von

Dipl. -ing. Joaquín Eduardo Urrutia Gómez

Dekan: Prof. Dr. Martin Bastmeyer

Referent: Prof. Dr. Pavel Levkin

Korreferent: Prof. Dr. Moritz Kreysing

Tag der mündlichen Prüfung: 10.12.2024

To Janna Meyer, whose endless patience has helped me get this far in one piece. Not just in this process, but throughout the last several years of my life.

Kurzfassung

Diese Doktorarbeit untersucht die Entwicklung und Anwendung von Strategien zur Flüssigkeitsmanipulation auf Droplet Microarrays (DMAs), einer Plattform, die einen einzigartigen Ansatz zur Begrenzung stationärer Flüssigkeiten in einem planaren, parallelen und miniaturisierten Format bietet. Im Gegensatz zu anderen mikrofluidischen Systemen, die typischerweise kontinuierliche Strömungen, geschlossene Kompartimentierung oder den Einsatz komplexer Komponenten erfordern, bieten DMAs ein einfacheres, offenes System. Dieses System positioniert Proben als Nanoliter-Tropfen in einem statischen, leicht indizierbaren 2D-Array-Format, das dem vertrauten Format von Well-Plates ähnelt, jedoch die Kapazität bietet, 0,4 bis 31,8 Experimente pro Quadratzentimeter durchzuführen. Diese Ähnlichkeit erleichtert die Integration und Anpassung sowohl standardisierter als auch neuer Laborprotokolle in ein miniaturisiertes Setting.

Diese Arbeit wird durch den wachsenden Bedarf an Miniaturisierung, Parallelisierung und Nachhaltigkeit in der wissenschaftlichen Forschung angetrieben, insbesondere in Bereichen wie der Wirkstoffentdeckung, zellbasierten Hochdurchsatz-Screenings und Omics. Durch die Entwicklung und Verfeinerung von Strategien für DMAs zielt diese Arbeit darauf ab, deren Anwendung in diesen Bereichen zu erweitern und einen praktischen Ansatz für die Integration traditioneller Laborprotokolle in ein miniaturisiertes Format zu bieten.

Die Arbeit beginnt mit der Einführung grundlegender Konzepte zum Verständnis und zur Kontrolle der Verdunstung von Tropfen auf planaren, gemusterten Arrays, die in der Zellkultur verwendet werden. Ein mathematisches Modell, basierend auf dem Cahn-Hilliard-Phasenfeld-Ansatz, sagt die Verdunstungsdynamik auf Droplet-Arrays voraus. Die Simulationen zeigen kritische Wechselwirkungen zwischen Luftfeuchtigkeit, Temperatur und benachbarten Tropfen aufgrund des Abschirmeffekts. Diese Erkenntnisse, die durch experimentelle Daten validiert wurden, ermöglichten die Erstellung eines digitalen Zwillings des DMAs, der eine frühe Vorhersage von Verdunstungsereignissen mit hohem Risiko während biologischer Assays ermöglicht, insbesondere bei Experimenten, die Probeninkubation oder Wärmebehandlung erfordern. Diese Arbeit hebt die Bedeutung der Optimierung der Benetzbarkeit und Strukturierung, der Dynamik der Tropfenpositionierung und -abstände im Array sowie der präzisen Kontrolle von Umweltparametern hervor, um die Reproduzierbarkeit

miniaturisierter Experimente sicherzustellen, insbesondere in Anwendungen wie dem High-Throughput Screening.

Der zweite Teil dieser Arbeit stellt die Entwicklung einer Strategie namens „Sandwiching-Methode“ zur Manipulation von Nanoliter-Tropfen vor. Diese Technik erleichtert die parallele Erneuerung des Mediums und die Zellmanipulation und ermöglicht die Langzeitkultur von Zell-Sphäroiden auf dem Chip. Sie erlaubt auch den nicht-destruktiven und nicht-invasiven Transfer und die Verschmelzung dieser biologischen Zellstrukturen zwischen DMAs, wobei Hunderte davon in einem einzigen Schritt gleichzeitig bewegt werden. Diese Methode eröffnet neue experimentelle Möglichkeiten, einschließlich nahtloser Sammlung, Übertragung, Ernte und Probenahme, alles ohne Unterbrechung laufender Experimente. Der letzte Abschnitt beschreibt die Konstruktion und Entwicklung des Automatisierten Nanoliter-Tropfenauswahl- und Sammelgeräts (ANDeS), das DMAs mit nicht-optischen Analysegeräten integriert. ANDeS wurde entwickelt, um die Herausforderungen beim Handling und Transfer von Nanoliter-Tropfen zu bewältigen, Probenverluste zu minimieren und gleichzeitig einen effizienten Probentransport zu ermöglichen. Dieses Gerät zeigt großes Potenzial in miniaturisierten Anwendungen, da es die Sammlung und den Transfer biologischer Proben, die in Nanoliter-Tropfen enthalten sind, in Fused-Silica-Kapillaren zur anschließenden Analyse ermöglicht. Experimentelle Ergebnisse zeigen, dass ANDeS die Vielseitigkeit der DMA-Plattform erheblich verbessert, indem es eine automatisierte Entnahme von Nanoliter-Proben ermöglicht, eine Aufgabe, die manuell auf der Ebene einzelner Tropfen nicht durchführbar ist. Dieser Fortschritt stellt einen wichtigen Schritt zur Integration von DMAs in bestehende Analyse-Pipelines dar und erleichtert so ein breiteres Spektrum experimenteller Auswertungen.

Im Laufe der Arbeit zieht sich das übergeordnete Thema der Transformation von Laborpraktiken hin zu Miniaturisierung und Parallelisierung. Fortschritte in der DMA-Technologie versprechen, den Ressourcenverbrauch erheblich zu reduzieren, den experimentellen Durchsatz zu erhöhen und die Entwicklung biologischer und chemischer Assays zu beschleunigen. Indem sie zentrale Herausforderungen adressiert und innovative Lösungen vorschlägt, bietet diese Arbeit neue On-Chip-Experimentierstrategien und -methoden, die letztendlich die Lücke zwischen miniaturisierten Assays und breiteren experimentellen Anwendungen schließen.

Abstract

This doctoral thesis investigates the development and application of strategies for liquid manipulation on Droplet Microarrays (DMAs), a platform that offers a distinctive approach for confining stationary liquids in a planar, parallel, and miniaturized format. Unlike other microfluidic systems, which typically involve continuous flow, closed compartmentalization, or the use of sophisticated components like pumps, valves and actuators, DMAs provide a simpler, open-format system. This system positions samples as nanoliter droplets in a static, easily indexable 2D array format, resembling the familiar format of well plates but with the capacity to conduct from 0.4 to 31.8 experiments per square centimeter. This similarity facilitates the integration and adaptation of both standard and new laboratory protocols into a miniaturized setting.

This work is driven by the growing demand for miniaturization, parallelization, and sustainability in scientific research, particularly in fields such as drug discovery, cell-based high-throughput screening, and omics. By developing and refining strategies for DMAs, this thesis aims to expand their use in these areas, providing a practical approach to integrating traditional laboratory protocols into a miniaturized format.

The thesis begins by introducing foundational concepts for understanding and controlling droplet evaporation on planar patterned arrays used in cell culture. A mathematical model, based on the Cahn-Hilliard phase-field approach, predicts evaporation dynamics on droplet arrays. The simulations reveal critical interactions between humidity, temperature, and neighboring droplets due to the shielding effect. These findings, validated by experimental data, enabled the creation of a digital twin of the DMA, allowing for the early prediction of high-risk evaporation events during biological assays, particularly those involving sample incubation or heat treatment. This work highlights the importance of optimizing wettability and patterning, the dynamics of droplet positioning and spacing within the array, and precise control of environmental parameters to ensure the reproducibility of miniaturized experiments, particularly in applications such as high-throughput screening.

The second part of this work presents the further development of a strategy called the “sandwiching method” for manipulating nanoliter-scale droplets. This technique facilitates parallel medium replenishment and cell manipulation, enabling long-term culture of cell

spheroids on-chip. It also allows for the non-destructive and non-invasive transfer and merging of these cellular structures between DMAs, moving hundreds of them simultaneously in a single step. This method opens new experimental possibilities, including seamless collection, transfer, harvesting and sampling, all without interrupting ongoing experiments.

The final section describes the design and development of the Automated Nanoliter Droplet Selection and Collection Device (ANDeS), which integrates DMAs with non-optical analytical instruments. ANDeS is designed to address the challenges of handling and transferring nanoliter-sized droplets, minimizing sample loss while allowing for efficient sample transport. This device shows great potential in miniaturized applications, enabling the collection and transfer of biological samples contained in nanoliter droplets into fused silica capillaries for subsequent analysis. Experimental results demonstrate that ANDeS significantly enhances the versatility of the DMA platform by enabling automated retrieval of nanoliter samples, a task not feasible manually at the individual droplet level. This advancement marks a major step towards integrating DMAs with existing analytical pipelines, thereby facilitating a broader range of experimental readouts.

Throughout the thesis, the underlying theme is the transformation of laboratory practices towards miniaturization and parallelization. Advancements in DMA technologies promise to significantly reduce resource consumption, increase experimental throughput, and accelerate the development of biological and chemical assays. By addressing key challenges and proposing innovative solutions, this work offers new on-chip experimental strategies and methodologies, ultimately bridging the gap between miniaturized assays and broader experimental applications.

Table of Contents

List of Figures

List of Tables

List of Abbreviations

ANDeS	An automated nanoliter droplet selection and collection device
^{0}C	Degree Celsius
HTS	High-Throughput
HEMA-co-EDMA	Hydroxyethyl Methacrylate-co-Ethylene Dimethacrylate
DMA	DropletMicroarray
DMEM	Dulbecco's Modified Eagle Medium
DMSO	Dimethyl sulfoxide
FBS	Fetal Bovine Serum
P/S	Penicillin/Streptomycin
RPMI	Roswell Park Memorial Institute (medium)
HeLa CCL2	Human cervical cancer cell
HEK 293T	Human Embryonic Kidney 293 cells with SV40 T-antigen
SU-DHL4	A cell line derived from human diffuse large B-cell lymphoma
h	hour
min	minute
s	second
m	meter
cm	centimeter
mm	millimeter
μm	micrometer
L	liter
mL	milliliter

μL	microliter
T	Temperature
PBS	Phosphate buffered saline
UV	Ultraviolet
Vis	Visible

Acknowledgement

Supervision

Prof. Pavel A. Levkin is thanked for his supervision. The mentoring and belief in my abilities were invaluable to my development as a scientist and researcher.

Dr. Anna A. Popova is thanked for her supervision, understanding, advice and for giving me the scientific freedom to pursue innovative and creative ideas.

Prof. Dr. Marus Reischl is thanked for trusting in my capabilities and letting me join his group to learn more about the fields of robotics, laboratory automation and machine learning.

Funding bodies

The Deutscher Akademischer Austauschdienst (DAAD) is thanked for awarding me with a stipend. The financial independence, support, events, German courses and feedback greatly improved my PhD experience. The Bio Interfaces International Graduate School (BIF IGS) is thanked for providing a platform for interdisciplinary collaboration.

Collaborators

Prof. Dr. Jeroen Krijgsveld is thanked for opening the doors to his research group at the Deutsches Krebsforschungzentrum (DKFZ) to learn more about proteomics and to give me the possibility to get in touch with high-end technologies and solutions. Prof. Nestler is thanked for opening her group to collaboration for the project "DMA's digital twin". Dr. Yanchen Wu and Dr. Fei Wang are thanked for his help with mathematical models and calculations. Dr. Marcel Schilling is thanked for showing me how to use the tools developed by Prof. Dr. Markus Reischl's group for automated image analysis, which also opened my way and interest to the field of machine learning. Dr. Mei Zhou is thanked for the excellent collaborative project we conducted. Dr. Moritz Braun is thanked for his help in programming and electronics. Dr. Adela Vrsanova is thanked for show me the world of proteomics and share her brilliant ideas on sample preparation and manipulation. Razan El Khaled El Faraj is thanked for the qPCR analysis and advice.

Students and Trainees

I thank all my fellow PhD students, trainees and also my fellow graduates of the Levkin group for the tremendous support they have always given me, both in the work and scientific fields, as well as on a personal level.

Miscellaneous

Thanks to the best lab buddy ever Dr. Maximilian Seifermann – enjoy the little time you have left as the most jacked postdoc, because here I come!

Preface

This thesis is based on the results gathered during my doctoral studies in the group of Prof. Dr. Pavel A. Levkin and was conducted between February 2021 and December 2024 at the Institute of Biological and Chemical Systems – Functional Material Interfaces (IBCS-FMS). The contributions of collaborators are specified at the beginning of each chapter.

During these four years working with the Droplet Microarray, an invention created by the group of Prof. Dr. Pavel Levkin, I realized that modern science operates in a **world made for giants, while its key players are microscopic**. Before starting my PhD, I worked in science using standardized methods, tools, and platforms used in laboratories worldwide. Working with these standards is straightforward since every instrument is perfectly configured for them. However, as Plato's Allegory of the Cave suggests, you cannot think critically and innovatively unless you step out of the norm and question the status quo. Joining Prof. Dr. Levkin's group was like stepping out of Plato's cave. Once you start thinking critically about miniaturization, you realize that using 96-well plates for drug screening is akin to eating alphabet soup with a gardening shovel. Despite technological advancements, the legacy of years of scientific development is still deeply rooted in conventional methods.

Realizing that using setups with liquid volumes up to a thousand times what a single cell needs, or more than a million times what an enzyme needs to float and find a cozy receptor, is like letting a cow graze alone all over America and then trying to locate it to obtain its milk. Achievable? Certainly. Practical? I'll leave that to the reader's judgment.

Assay miniaturization should be an inherent perspective when approaching experimental design. Today's technology allows us to seamlessly miniaturize all kinds of methodologies, techniques, and tools. The scientific community has gone so far as to create lab-on-a-chip devices that can be sent into space to conduct experiments in the microgravity environment of spacecraft, [1] where building a full-scale laboratory is impractical, if not impossible.

It is evident that we are getting closer to making the Lab on a Chip concept a reality, not only for specialized applications but also for everyday use in common laboratory settings. However, the current focus of most solution-providing industries is on producing standardized equipment, with only few daring to take the first steps towards developing tools that enable researchers to push the boundaries of miniaturized research. While the idea of advancing to the

next sub-level entails multiple challenges, as you will read in this thesis, it is important to understand that the benefits are immense in comparison. These advantages are not only crucial for scientific development but also have a significant positive impact on the environment.

The traditional methods and tools used in laboratories consume vast amounts of consumables, generate significant waste, and contribute to pollution and CO_2 emissions. By adopting miniaturized techniques, we can drastically reduce the volume of materials required for experiments, minimize waste production, and lower the overall carbon footprint of scientific research. This shift towards more efficient and eco-friendly practices in the laboratory is vital for reducing the environmental impact of scientific progress.

With this thesis, the author aims to contribute to advancing towards the miniaturization of laboratory environments.

The work presented in this dissertation includes three published articles and additional unpublished results. The articles are listed as follows:

Article 1: Digital twin of a droplet microarray platform: Evaporation behavior for multiple droplets on patterned chips for cell culture. Y Wu, **JE Urrutia Gomez**, H Zhang, F. Wang, PA Levkin, AA Popova, B Nestler. Droplet 3 (1), e94.

Article 2: Highly Parallel and High-Throughput Nanoliter-Scale Liquid, Cell, and Spheroid Manipulation on Droplet Microarray. **JE Urrutia Gomez**, M Zhou, NK Mandsberg, JA Serna, J Von Padberg, S Liu, M. Reischl, PA Levkin, AA Popova. Adv. Funct. Mater. 2024, 35, 2410355. https://doi.org/10.1002/adfm.202410355.

Article 3: ANDeS: An automated nanoliter droplet selection and collection device. **JE Urrutia Gomez**, R El Khaled El Faraj, M Braun, PA Levkin, AA Popova. SLAS Technology 29 (1), 100118.

The following works that published during the PhD study, are not included in the present dissertation.

- Grid screener: A tool for automated high-throughput screening on biochemical and biological analysis platforms. MP Schilling, S Schmelzer, **JE Urrutia Gomez**, AA Popova, PA Levkin, M Reischl. IEEE access 9, 166027-166038

- Automated high-throughput image processing as part of the screening platform for personalized oncology. MP Schilling, R El Khaled El Faraj, JE **Urrutia Gomez**, SJ Sonnentag, F Wang, B Nestler, V Orian-Rousseau, AA Popova, PA Levkin, M Reischl. Scientific Reports 13 (1), 5107
- Enhancing Temperature responsiveness of PNIPAM through 3D-Printed Hierarchical Porosity. W Liu, Z Wang, J Serna, R Debastiani, **JE Urrutia Gomez,** L Lu, W Yang, Z Dong, PA Levkin. Advanced Functional Materials, 2403794.
- Electrode Droplet Microarray (eDMA): an impedance platform for label-free parallel monitoring of cellular drug response in nanoliter droplets. M Zhou, **JE Urrutia Gomez**, NK Mandsberg, S Liu, S Schmidt, M Meier, PA Levkin, HG Jahnke, AA Popova. Adv. Healthcare Materials, 2402046.
- Front Cover, Volume 3, Number 1, January 2024. Y Wu, **JE Urrutia Gomez**, H Zhang, F. Wang, PA Levkin, AA Popova, B Nestler. Droplet 3 (1), e115.

Affidavit

Hiermit versichere ich, diese Arbeit selbstständig verfasst zu haben, dass ich keine anderen als die angegebenen Quellen und Hilfsmittel benutzt habe, dass ich die wörtlich oder inhaltlich übernommenen Stellen als solche kenntlich gemacht habe und die Satzung des KIT zur Sicherung guter wissenschaftlicher Praxis in der jeweils gültigen Fassung beachtet habe.

Karlsruhe, den 06.10.2024

1. General Introduction

In recent years, scientific research has increasingly focused on developing technologies that enhance efficiency and reduce resource consumption. One significant area of innovation is the miniaturization of experimental methodologies. [2] These advancements are particularly important in fields such as drug discovery, diagnostics, and materials science, where the ability to perform a large number of experiments quickly and accurately can accelerate the pace of innovation. However, the challenge lies in effectively manipulating and analyzing these small volumes of liquids. [3] Rapid evaporation, precise droplet manipulation, and the integration with analytical devices are among the key obstacles that researchers must overcome.

1.1. The Role of Miniaturization in Modern Research

1.1.1. Miniaturizing Biological Assays for Enhanced Efficiency

The miniaturization of biological assays has revolutionized scientific research, offering significant advantages over traditional methods. Conventional biological assays typically require large sample volumes and extensive resources, making them costly, bulky, and contributing to higher CO_2 emissions. [4] [5] [6] [7] As the scientific community shifts towards more efficient and sustainable practices, miniaturized biological assays have become a focal point due to their potential to mitigate these issues. Furthermore, they offer benefits such as increased throughput and improved sensitivity. [8]

One of the primary benefits of miniaturized assays is the reduction in sample and reagent volumes. By scaling down the size of the assays, researchers can perform a larger number of experiments with the same amount of material. This is particularly advantageous when working with expensive or limited samples, such as rare biological specimens or high-cost reagents. [9] [10] Additionally, the smaller volumes used in miniaturized assays often result in faster reaction times and increased sensitivity, as the surface-to-volume ratio is significantly higher, enhancing molecular interactions and detection capabilities. [11]

Moreover, miniaturized assays facilitate increased parallelization, allowing researchers to test thousands of conditions simultaneously. This feature is essential for applications where it is necessary to evaluate a large number of variables within the same assay. [12] For example, in drug development, miniaturized high-throughput screening platforms are used to identify potential therapeutic compounds from large chemical libraries. [13] In genomics and

proteomics, microfluidic devices enable the efficient analysis of DNA, RNA, and proteins, providing valuable insights into the genetic and molecular mechanisms underlying diseases. [14] [15] Additionally, in the field of personalized medicine, miniaturized assays facilitate the analysis of patient-specific samples, enabling tailored treatment strategies based on individual biological profiles. [16]

1.1.2. Advancements in the Implementation of Miniaturized Assays

Technological advancements have been essential in the development and implementation of miniaturized biological assays. Microfluidics, a technology focused on accurately maneuvering small volumes of liquids (typically ranging from picoliters to microliters), [17] has enabled the integration of multiple laboratory functions onto a single chip. These devices allow for tasks such as cell culture, biochemical reactions, and analytical measurements to be performed with high precision and reproducibility, while also minimizing contamination and evaporation. [18]

Over the past twenty years, the field has seen significant advancements in both technological capabilities and application areas. Numerous systems and functional components have been created to execute a wide range of user-specified operations. The advent of computer-aided design software and automation tools has further expanded the potential of microfluidic applications. Currently, the focus has shifted from developing fundamental methods and techniques to applying them in key, timely, and crucial areas within the chemical and biological sciences. [19]

One prominent example of this evolution is the diversity of microfluidic chip designs. There are many different types, such as hydrogel microfluidic chips, microfluidic chips integrated with 3D culture technology, microfluidic chips fused with detection instruments, microfluidic chips for single cell analysis, microfluidic model organism chips, and droplet-based microfluidic chips. [20] [21] Among these formats, droplet-based microfluidics platforms represent a significant advancement in the fields of parallelization and miniaturization. These platforms combine the benefits of conventional microfluidics with a sophisticated and versatile method for compartmentalizing experiments. [22] [23] [24]

Droplet-based microfluidic systems excel in manipulating uniformly arranged microdroplets at high velocities, allowing the formation of thousands of droplets every second. [25] By integrating complex micropump and microvalve systems, droplet-based microfluidics can

precisely control droplets within the microfluidic channels, typically producing them in immiscible fluids, thereby preventing gas-liquid interaction and ensuring the integrity of the experiments. [26] In biological assays, this technology is commonly used to trap cells, spheroids, [27] or tumoroids [28] within nano- to picolitre droplets. This enables the sorting and parallelization of these samples within tiny droplets that act as mini reactors. [29]

One remarkable application of droplet-based microfluidics is the generation of uniformly sized tumor spheroids for photothermal therapy. In this process, cells are encapsulated within nano- to picolitre-sized droplets, forming spheroids of controlled size. These droplets are then grown independently of each other within the same chip, and treated with nanomaterials that, when exposed to near-infrared light, induce localized heating, effectively targeting and killing tumor cells. [30]

However, despite their multiple advantages, droplet-based microfluidic systems can face challenges such as the complexity of device fabrication, low compatibility with standard analytical devices, and issues like droplet coalescence, which require precise control mechanisms to avoid cross-contamination [31] [32] [33] Furthermore, the closed nature of these systems can make it difficult to access droplets for subsequent manipulation.

To address some of these limitations, the droplet microarray (DMA) platform was developed. DMAs enable drastic miniaturization of experimental vessels by confining stationary droplets in discrete, parallel compartments that are exposed to the environment, allowing easy indexing and manipulation. This distinct setup makes DMAs particularly suited for applications requiring high-throughput screening and precise control over static droplet arrays.

1.1.3. Droplet Arrays as High-Throughput Screening Platform

Droplet arrays offer an alternative approach to miniaturization and parallelization, leveraging the strengths of both droplet-based microfluidics and traditional multi-well plates. These arrays confine experiments in extremely small and discrete compartments while remaining open, and accessible, thus increasing their compatibility with a variety of analytical devices. [34] Similar to droplet-based microfluidics, droplet arrays have been designed in various formats to streamline specific applications. These include setups such as microchambers, [35], mini-pillar arrays, [36], liquid marbles, [37] and wettable patterns, [38] which offer diverse methods for experimental design, manipulation, and analysis.

Specifically, droplet arrays based on wettable patterns not only replicate all the functionalities of a multi-well plate but also enhance them. Their wall-less design allows for innovative procedures, such as parallel droplet sampling using the slide sandwich technique or merging neighboring droplets through dragging. Additionally, they offer numerous advantages, including rapid mixing and reaction times, due to the small volume and high surface area of the liquids. [39] [40] To date, droplet arrays have been implemented with several thousand individual experiments (or droplets), enabling ultra-fast throughput and massively parallel experimentation.

As reported by Feng et al., [41] the Droplet Microarray (DMA) is a droplet array capable of containing hundreds to thousands of droplets on a standard glass slide with dimensions of 75 x 25 mm. The DMA is patterned using light-triggered click chemistry, a method that makes it possible to create hydrophilic spots on a super-hydrophobic background. These spots allow liquids to be pinned to the surface in a desired manner. The flexibility of this production method permits the creation of customized designs, including various geometries, sizes, locations, distributions, and spot layouts, making it adaptable to the specific needs of individual experiments. [42] [43] [44]

1.2. The Droplet Microarray

1.2.1. The Droplet Microarray as High-Throughput Screening Platform

The Droplet Microarray (DMA) has been employed for a variety of biological techniques traditionally conducted using microtiter plates, which typically operate with microliter volumes. DMA's ability to handle volumes in the nanoliter range significantly reduces material consumption, thereby enabling a larger number of experiments to be performed with a limited amount of starting material. This is particularly advantageous for applications involving patient-derived cells, where only a small quantity of material can be obtained from the patient.

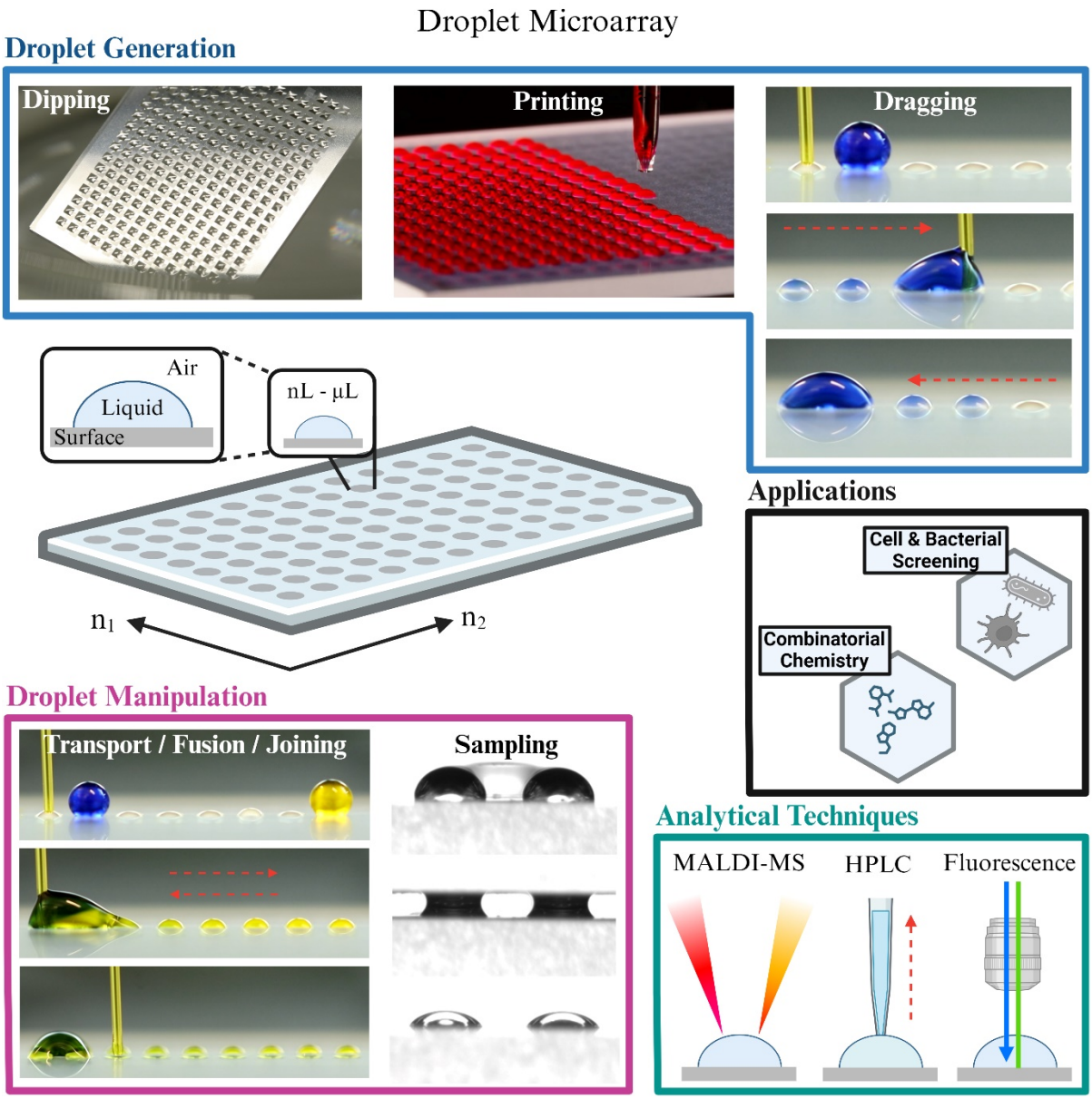

Figure 1. An overview of the Droplet Microarray (DMA). The DMA refers to an arrangement of droplets systematically positioned on a surface within an open and planar glass slide. The open format is characterized by at least one exposed surface, providing straightforward access to the samples. Unlike closed microfluidic systems, this openness expands the range of possible sample manipulations, experiments, analyses, and applications. The dimensions n_1 and n_2 indicate the number of droplets aligned in each direction on the microarray surface. The snapshot "Printing" was taken from a video by M2 Automation GmbH, published by Mario Nitzsche.

For instance, Cui et al. used a DMA with 588 spots, each containing 300 cells in a volume of 200 nL, to test 2.208 FDA-approved drugs on IDH1-mutated glioma cell lines derived from two patients. They identified 20 drugs that affected tumor sphere formation and viability. This study not only showcases the benefits of miniaturization and parallelization but also underscores a unique feature of DMA compared to standard well plates. [45]Thanks to its surface wettability properties, the DMA can be used upside down to implement the hanging drop method. The confinement of droplets relies solely on the positive interaction between the liquid and the hydrophilic spots, rather than on physical walls. This allows the liquid to adhere

to the surface without additional measures, eliminating the surface for cell adhesion and promoting 3D cell growth. [46] In this study, the hanging drop method replicated the 3D growth characteristics of patient-derived tumor spheres, achieving the parallel formation of 588 tumor spheres per DMA. [45] Furthermore, other reports demonstrated that the surface characteristics of the DMA allow for controlled mixing of neighboring droplets. This enables the combination of 3D cultures with 2D cultures or the merging of multiple spheroids into a single, larger droplet for functional analysis. [47] [48]

Another example illustrating the capabilities of DMA is the study by Popova et al. [49] In this study, a 108-spot DMA format, capable of containing up to 5 μL per spot, was used to culture and screen individual zebrafish embryos with fluorescently labeled cell-penetrating peptoids for subsequent analysis by fluorescence microscopy. Utilizing the inherent properties of DMA, peptoid libraries were presented to each embryo in a parallel, rapid, non-invasive, and non-destructive manner.

The study employed the sandwich method, where the original DMA with the embryos was sandwiched with an identical DMA containing the compounds. This created a sandwich structure, positioning the embryos between the two DMAs and allowing the compounds to mix with the droplets containing embryo. After culturing the embryos in this configuration, the DMA containing the compounds was removed. Since both slides have identical hydrophilicity, the mother droplet formed by the sandwiching in each spot was evenly distributed, leaving the embryos undisturbed in their original locations with the same amount of liquid as at the beginning. [49]

The vast variety of possible topographies that can be created for DMA, combined with its surface wettability properties, provides it with unique flexibility for applications in biological studies, enabling innovative approaches to cell culture and manipulation.

1.2.2. Surface Wettability of the Droplet Microarray

Wettability refers to how a liquid spread across a surface, including the strength of its attachment and the extent of the contact area it maintains. The most straightforward way to characterize wettability is through the contact angle (θ), which is the angle formed at the junction of the liquid-solid and air-liquid interfaces. When a droplet comes into contact with a solid surface, it forms a contact line where the liquid, gas, and solid substrate intersect. As

shown in Fig. 2, Young's equation connects the surface tensions of the solid-liquid (γ_{sl}), liquid-gas (γ_{lg}), and solid-gas (γ_{sg}) interfaces with the equilibrium contact angle through a force balance, expressed as

$$\cos\theta = \frac{\gamma_{sg}-\gamma_{sl}}{\gamma_{lg}} \tag{1.1}$$

For instance, when $\theta < 90\circ$, the solid surface is considered hydrophilic, while it is called hydrophobic surface, when $\theta > 90\circ$. Especially, when $\theta > 150\circ$, the surface becomes superhydrophobic, and the droplet on it approaches a spherical shape. [50]

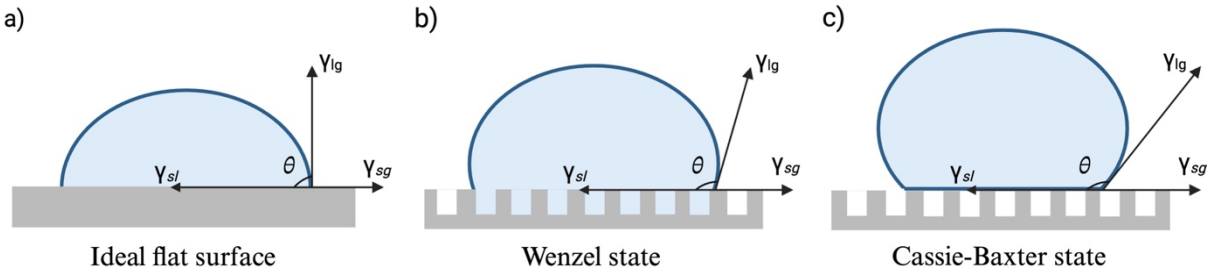

Figure 2. Diagram of a droplet on an ideal flat surface and on rough surfaces. (a) Schematic of Young's equation, illustrating the mechanical force balance at the three-phase contact line when the droplet is on an ideal surface. (b) Wenzel state. (c) Cassie-Baxter state.

In practice, real surfaces always exhibit roughness and defects. The wetting behavior of droplets is significantly influenced by the chemical and physical characteristics of these solid surfaces. When droplets are placed on rough surfaces, they can exist in one of two wetting states: the *Wenzel* state or the *Cassie-Baxter* state, as illustrated in Fig. 2 (b) and (c), respectively. [51] In the *Wenzel* state, the droplet completely wets the rough surface, and if the substrate has chemical hydrophilic properties, the roughness promotes this state. Conversely, in the *Cassie-Baxter* state, the droplet rests on top of the rough structure with air trapped underneath. In this scenario, the droplet exhibits a large apparent contact angle and a low sliding angle. The apparent contact angle for *Wenzel* state is described by the Wenzel equation.

$$\cos\theta_w = r\cos\theta \tag{1.2}$$

where θ_w represents the *Wenzel* angle, and θ signifies the contact angle on a smooth surface made of the same material. The variable r is defined as the ratio between the actual area and the projected area covered by the droplet. *Cassie and Baxter* further developed the concept of apparent contact angles for the wetting of porous surfaces. They proposed that the apparent contact angle is influenced by the energies of the contact area beneath the droplet, which

consists of two components: *component 1* and *component 2*. The apparent contact angle can be expressed as

$$\cos\theta_{app} = f_1 \cos\theta_1 + f_2 \cos\theta_2 \quad (1.3)$$

where f_1 and f_2 represent the area fractions of the two components, and θ_1 and θ_2 are their respective contact angles. For porous surfaces, one of the components (f_2) is air (θ_2 = 180°), and Eq. 1.3 then simplifies to

$$\cos\theta_{CB} = f_1 \cos\theta_1 + f_1 - 1 \quad (1.4)$$

this is known as the *Cassie-Baxter* equation, where θ_{CB} denotes *the Cassie-Baxter* angle. It is important to note that both the *Wenzel* and *Cassie-Baxter* models are applicable only when the droplet size is significantly larger than the surface structure. The apparent contact angle observed for the droplet reflects the average wetting characteristics of the substrate.

The wettability properties can be controlled by chemical functionalization and modifying the surface roughness. For instance, Geyer et al. demonstrated that by coating a glass substrate with a thin film of a porous copolymer consisting of 2-hydroxyethyl methacrylate (HEMA) and ethylene dimethacrylate (EDMA) to achieve a surface with a contact angle of less than 90°. Using photolithography in a grafting-from approach, they then polymerized a copolymer of 2,2,3,3,3-pentafluoropropyl methacrylate (PFPMA) on the HEMA-EDMA polymer, which exhibited a contact angle greater than 150°. This process resulted in a pattern where the hydrophilic background was divided in an array format by hydrophobic borders, effectively creating distinct areas for liquid confinement. [52]

1.2.3. Fabrication Methods and Surface Chemistry of the Droplet Microarray

Nowadays, the methods for fabricating the DMA have significantly advanced, particularly for applicability to biological screening. Based on the approach of using the porous HEMA-co-EDMA polymer, the first DMA was created, but this time by modifying the hydroxy groups on the polymer surface with pentanoic acid in an esterification reaction to convert the terminal groups into alkynes. These alkynes were then reacted with hydrophilic and hydrophobic thiols in a thiol-yne reaction to produce the patterned substrate. (Fig. 3) The resulting surface exhibited a contact angle of 169° for the superhydrophobic regions and 4.4° for the superhydrophilic regions. [41]

Although this technique enabled the confinement of both aqueous droplets and organic solvents, such as DMSO, the surface exhibited significant inhomogeneity, with increased molecular adsorption in the hydrophilic regions due to the highly polar nature of the polymer. This made the surface inefficient for biological applications, such as drug screening.

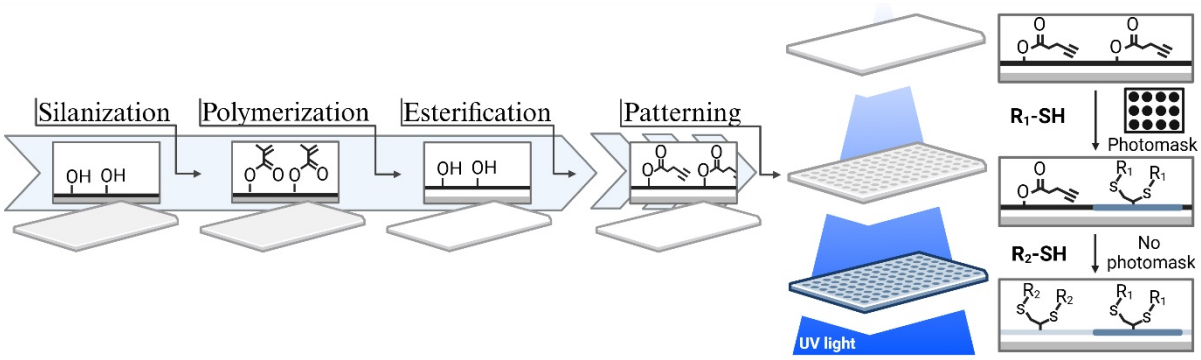

Figure 3. Schematic illustration of the surface modifications throughout the manufacturing stages of a HEMA-co-EDMA DMA. R_1 = Hydrophobic perfluoroalkyl group, R_2 = Hydrophilic amine group.

To address these issues, a new strategy called Z-slide was developed. In this approach, roughness was introduced to the glass slide by adding a coating of silica nanoparticles. These nanoparticles were pre-functionalized with trimethoxyvinylsilane in a polycondensation reaction and then spin-coated onto the glass surface. The vinyl groups were then used in the final step to create surfaces with different wettability using UV-induced radical addition of hydrophilic thiols such as 2-mercaptoethanol and cysteamine or hydrophobic thiols like 1H,1H,2H,2H-perfluorodecanethiol (PFDT) to the C-C double or triple bonds present on the surface. This step, thanks to photolithography and its accompanying high resolution and precision, allows for the creation of a large density of confined experimental vessels, reaching up to 2187 spots per slide. [53] This strategy produces a surface that provides high stability for aqueous droplets while significantly reducing non-specific adsorption of substances compared to previously mentioned techniques.[48]

The physical and chemical properties of a substrate are crucial in determining how droplets interact with its surface. These properties affect surface tension and wetting characteristics, directly influencing the droplet's behavior. When a droplet is placed on a hydrophilic spot surrounded by a superhydrophobic background, it adopts a specific shape dictated by the balance of adhesive and cohesive forces. Consequently, the contact angle and curvature of the droplet can be adjusted based on the geometry of the spot during the UV-induced radical addition guided by the photomask. The *Young-Laplace* equation explains how the geometry of

a droplet influences its physical properties. A curved droplet interface results in surface tension causing a pressure difference across the liquid-vapor interface. [54] [55] This relationship is expressed as:

$$\Delta p = \gamma \left(\frac{1}{R_1} + \frac{1}{R_2} \right) \quad (1.5)$$

where Δp is the pressure difference, known as *Laplace* pressure, γ is the surface tension, and R_1 and R_2 are the radii of curvature. For a theoretical case of a spherical droplet, the equation is represented as follows [56]:

$$\Delta p = \frac{2\gamma}{R} \quad (1.6)$$

Understanding the principles of Laplace pressure is crucial for effective droplet handling in droplet arrays. By exploiting pressure differences and surface tension characteristics, techniques such as droplet anchoring, merging, splitting, and directional movement can be successfully implemented. However, these manipulations present inherent challenges. Achieving accurate control and optimization requires understanding droplet geometry, volume, and substrate wettability, both for controlling and generating droplets. Consistent results depend on fine surface pattern design and careful calibration of wettability contrasts. [57]

1.3. Experimental Operation on Droplet Microarrays

1.3.1. Droplet Generation on Solid Substrates

In open microfluidic systems, droplets can be generated passively without the need for pumps by balancing hydrostatic and capillary pressures resulting from the channel geometry. In droplet arrays, an important factor influencing generation throughput is the method of droplet deposition or formation on the plate. On surfaces with significant wettability contrasts, discontinuous wetting can automatically partition a volume through a periodic wettability pattern. The DMA has led the way in using discontinuous wetting to create droplet microarrays by moving a volume across a surface with hydrophilic and hydrophobic patterns. [39]

As published by Popova et al., [58] the wettability contrast property was used to develop a method for reverse transfection and reverse screening of drugs on DMA. This method consisted of depositing transfection and drug mixtures directly onto the spots, followed by homogeneous seeding of cells by immersing the DMA in cell-containing culture medium and then removing

it. Due to the discontinuous wetting process, droplets containing cells were spontaneously created at each spot, allowing subsequent cell culture within the droplets.

However, droplets can also be automatically and accurately deposited on the DMA using technologies such as inkjet printing, acoustic droplet dispensing, pipetting robots, or liquid dispensers. These contact-free liquid printing techniques eject droplets at high speed onto the DMA. This process does not require contact with the substrate or pre-printed droplets. It enables the sequential addition of reagents or biological agents, such as cells or bacteria, to each droplet in a selective and controlled manner. This approach also avoids cross-contamination and allows for dynamic procedures within a single droplet, permitting complex experimental settings. [59]

An interesting application of this droplet addition strategy was demonstrated by Wiedmann et al. [60] Using a non-contact liquid dispenser, they developed a method for the automated and programmable merging of aqueous nanoliter droplets with organic droplets. In this method, the droplets were not only printed with the liquid dispenser but also merged by directing the dispenser between the droplets on the hydrophobic borders of the DMA. This caused the droplets of different compositions to combine into a single larger droplet, effectively mixing the contents from two neighboring spots into one.

Ultimately, both passive and active droplet generation techniques offer unique advantages for creating droplets. Passive methods, leveraging discontinuous wetting and wettability contrasts, provide a straightforward and efficient approach without additional costs. However, they risk cross-contamination between spots and do not allow for the sequential addition of liquids or the inclusion of different compounds in each droplet. On the other hand, active methods, such as liquid dispensers, enable precise and controlled droplet deposition. This allows for more dynamic assays with sophisticated protocols and the possibility of having varied experimental conditions on a single DMA. However, these methods are more complex to implement, as dispenser heads or setups are not typically designed for miniaturized platforms, requiring adaptations that increase the cost of the technique.

1.3.2. Droplet Sampling from Solid Substrates

Sampling droplets from patterned solid substrates presents unique challenges compared to conventional microplates. In the case of DMAs, the sampling method can vary depending on

the array format chosen. For example, large arrays with spots capable of handling volumes over 2 µL are manageable with conventional pipettes. As demonstrated by Höpfner et al., where the palladium-catalyzed Suzuki-Miyaura reaction was implemented on DMA to synthesize a library of 800 biphenyl compounds. Some of these compounds were released from 3 mm diameter spots by sequentially pipetting 5 µL of deionized water onto them, allowing them to be loaded onto a chromatography-mass spectrometry system for analysis. [61]

For arrays containing hundreds to thousands of nanoliter-sized droplets, the handling complexity increases. These smaller droplets are located on smaller spots and are often in closer proximity to neighboring droplets (e.g., 1 mm pitch). Manual collection of these droplets is nearly impossible due to the required precision and speed to prevent evaporation. Techniques like pooling droplets into a larger one, as reported by Chakraborty et al., are useful in such scenarios. In this study the authors used a DMA with 672 square spots, each 1 mm^2, to perform cDNA on-chip analysis from cells using real-time PCR. The spots containing cDNA from single cells were pooled by adding 7 µL of nuclease-free water, then collected with a pipette and deposited into PCR microtubes. [62] This approach works well when molecules can be easily identified between spots, such as with molecular labeling.

However, when samples are isolated and cannot be identified if mixed, individual droplet collection techniques become essential. Custom strategies, such as charged surface pipettes [63], tailor-made liquid handlers, [64] or “sandwiching” techniques, [65] are employed to address this challenge. These methods are necessary because commercial devices, like robotic pipettors, autosamplers, or liquid handlers, are generally not designed to handle the small topographical formats or volumes typical of droplet microarrays.

In addition, nanoliter-sized droplets are highly prone to evaporation in open systems, making their collection even more challenging. Evaporation can cause significant changes in droplet volume, affecting both the sampling process and the concentration of reagents, as well as the overall reaction dynamics, thereby compromising the reproducibility and accuracy of experiments. Uneven evaporation across an array can result in heterogeneous conditions, where some droplets might evaporate completely while others remain intact, leading to inconsistent results. The loss of solvent through evaporation can also alter the chemical environment within the droplets, potentially impacting the stability and activity of sensitive biological samples, such as cells or enzymes. Therefore, the sampling strategy must either be rapid enough to prevent evaporation, as seen with the sandwiching technique, or incorporate methods to slow

down evaporation. This can be achieved by adjusting the environment, such as lowering the temperature or increasing humidity, or by using substances that slow down the evaporation like DMSO [66] or glycerol.

1.3.3. Evaporation Behavior of Sessile Droplets

The evaporation of sessile droplets on DMAs is a critical process that can significantly affect experimental results. Given the small volume of droplets, evaporation occurs rapidly, leading to changes in concentration and potential loss of sample integrity.

Sessile droplets can evaporate in three primary modes: constant contact angle, constant contact radius, and a mixed mode where both angle and radius change. The mode of evaporation depends on the surface wettability and the surrounding environmental conditions. In the constant contact angle mode, the contact angle remains constant while the contact radius decreases, leading to a gradual reduction in droplet volume. In the constant contact radius mode, the contact radius remains fixed, and the contact angle decreases until the droplet evaporates completely. (Fig. 4) [67] [68]

In diffusion-controlled evaporation with a constant contact angle, the evaporation rate is directly proportional to the radius of the droplet base or its perimeter. [69] In contrast, for the constant contact radius mode with $\theta < 90°$, such as droplets pinned to the spots of the DMA, evaporation occurs more intensively near the three-phase contact line. Some explanations for this are: (i) the existence of disjoining pressure at the three-phase contact line; (ii) the non-uniform distribution of vapor flux over the droplet; and (iii) the non-uniform distribution of the temperature field. [70]

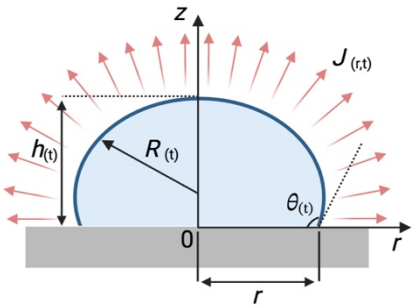

Figure 4. Schematic of the evaporation flux of a sessile droplet in constant contact radius mode. h(t) represents the height of the droplet at its highest point, measured from the substrate to the top of the droplet. It varies with time t. R(t) the radius of curvature of the droplet at its highest point. It describes the curvature of the droplet's surface and changes with time t. θ(t) The angle formed between the tangent to the droplet surface at the contact line and the horizontal substrate. This angle changes as a function of t. r the radius of the droplet base, measured

from the central point 0 to the edge of the droplet on the substrate. J(r,t) the evaporation flux at a point on the droplet surface, which varies depending on both radial position r and time t.

Evaporation is not only critical for sample integrity and droplet collection but also when using the DMA with analytical devices. For example, microscopy of the droplets containing cells requires placing the DMA under a microscope at ambient conditions, which can take hours and lead to evaporation. A similar issue arises with colorimetric assays, where the DMA provides an excellent format by displaying all points organized in an easily interpretable image. However, this process exposes the droplets to the environment, potentially biasing the results by increasing the concentration of analytes due to evaporation. This challenge also applies to cell incubation on the DMA, which typically requires days in environments where temperature and humidity are not conducive to droplet preservation.

To address these challenges, various strategies have been developed to mitigate evaporation. For example, in the work of Popova et al. [71], the DMA was used to assess the viability of cell cultures in 2D and 3D using simple digital imaging steps. The authors used microscopy to analyze the viability of cells in response to anticancer drugs by means of cell staining and colorimetric techniques. Both assays also required incubation steps in cell incubators for extended periods. Anti-evaporation strategies for these experiments were focused on increasing ambient humidity above 70% to prevent droplet evaporation. For instance, during sample printing on the DMA, a non-contact liquid dispenser adapted with an environmental humidifier maintained a 70% humidity level. For microscopy and incubation, they used a humidity chamber, consisting of a common petri dish with pads soaked in phosphate-buffer saline (PBS), which, when sealed, maintained nearly 99% internal humidity, effectively preventing evaporation.

However, some studies have reported using evaporation in droplet arrays to their advantage. For example, in case when controlled evaporation can be used to concentrate analytes present in the droplets. The droplet maintains a quasi-spherical geometry, and as it evaporates, the analytes are deposited within a detection area of a few square millimeters. [72] This concept is also used for separating bacteria, mammalian cells, and antibodies by leveraging the coffee-ring effect driven by evaporation. This effect creates a distribution of analytes from the perimeter of the droplet based on the size of the molecules. [73] These methods exemplify techniques that fall into the category of so-called on-chip analysis, as they allow the use of analytical techniques such as Raman spectroscopy, matrix-assisted laser desorption/ionization

mass spectrometry (MALDI-MS), or dielectrophoretic impedance within the same workflow to obtain the final outcome.

1.3.4. Integration of DMAs with Analytical Methods

Droplet microarrays provide an excellent platform for integration with analytical pipelines, especially those utilizing optical methods. Fluorescence sensing, one of the most mature technologies for biochemical molecule and cell sensing, has been successfully applied on DMAs for various applications. These include high-throughput synthesis of photodegradable hydrogels and analysis of 2D and 3D multicellular architectures. [74] [48] [47] [75] [16]. Integrating DMAs into these assays facilitates high-throughput analyses and enables high-density droplet fluorescence detection in biosensing.

Colorimetric sensing, which involves changes in solution color during chemical reactions and relates the color intensity to the analyte concentration, is another significant example. The miniaturization of colorimetric methods over the past two decades has enhanced their prominence for high-throughput and portable sensing. Droplet arrays, as a typical miniaturization unit, are accessible, low-cost, and do not require sophisticated instruments, allowing for multiple qualitative, semi-quantitative, and fully quantitative colorimetric sensing experiments. Colorimetric sensing has been successfully implemented on DMAs in studies such as the investigation of new antibiotics against multidrug-resistant bacteria [76] and viability assessment in 2D and 3D cell cultures. [71]

The open format of DMAs makes samples physically accessible, allowing the implementation of analytical methods beyond microscopy. For instance, IR/Raman spectroscopy, which can recognize chemical fingerprints of trace analytes for drug monitoring, biomarker detection, and cell imaging, has been successfully applied on DMAs. [53] Similarly, on-chip MALDI-MS, which involves mixing the sample with a matrix compound that absorbs laser light to facilitate desorption and ionization of analytes, has been implemented. Integrating DMAs with MALDI-MS is straightforward and has been demonstrated in various applications, including cell, protein, and chemical analyses. [77] [78] Additionally, UV-VIS spectroscopy on-chip has also been demonstrated. The excellent optical properties of DMAs allow adaptation for UV-VIS plate readers using the sandwiching technique, which traps droplets between two slides, enabling individual droplet analysis via plate readers. [53]

Techniques that facilitate real-time monitoring of samples are also favored by this format. For instance, DMAs have been applied to electrochemical sensing chips, where droplets form directly on the electrodes, allowing for non-invasive direct readout. [79]

Despite the versatility of DMAs for various analytical methods, there are still significant challenges in integrating them with non-optical analytical instruments. Instruments such as liquid chromatography-mass spectrometry (LC-MS), nuclear magnetic resonance spectroscopy (NMR), capillary electrophoresis (CE), flow cytometry, polymerase chain reaction (PCR), real-time PCR (qPCR), and techniques like western blotting or gel electrophoresis require physical removal of the droplet content from the DMA. Therefore, these techniques need samples to be transferred individually to the analytical equipment, making the perform of the entire workflow on-chip impossible.

1.3.5. Challenges in Integrating DMAs with Non-Optical Analytical Instruments

The challenge of integrating DMA with non-optical analytical instruments centers on developing an effective method for collecting and transferring nanoliter-size droplets. This task involves addressing three key criteria [80]:

(i) Handling Small Volumes: The minute size of the droplets, often as small as 200 nL, renders manual handling impractical. Precision is vital, as these droplets are typically 350 μm in height on a 1 mm^2 hydrophilic base. Additionally, the close spacing of droplets, sometimes only 500 μm apart, necessitates the use of automation to manage them effectively.

(ii) Minimizing Dead Volume: In larger assays, nanoliter-scale losses due to sample handling might be negligible. However, at the nanoliter scale, such losses become significant. Therefore, it is crucial to minimize dead volume to ensure accurate and reliable sample analysis.

(iii) Evaporation Control: Rapid evaporation is a major issue when working with nanodroplets exposed to the environment. To counteract this, sample collection methods must either be extremely fast or designed to prevent evaporation effectively.

Overcoming these obstacles is crucial for expanding the potential of droplet arrays, as it would open doors to a wider range of analytical read-out methods and equipment. Various groups have demonstrated progress in addressing these criteria, with advancements in interfacing droplet arrays with devices like HPLC, [81] LC-MS/MS, [82] nanoLC, [83] and NMR, [84] serving as notable examples. However, these solutions are often built in house, therefore not

commercially available, and tailored to specific applications and lack universal applicability, limiting their reproducibility and broader adoption.

A case in point is the work presented by Li et al., [85] where the authors created a setup involving a nanoliter-scale oil-air-droplet (OAD) chip with a four-layer cube structure designed to minimize sample loss due to evaporation, specifically for single-cell proteomic assays. The chip uses an oil layer to prevent droplet evaporation, an isolation layer to segment the droplet with oil, and a droplet layer for sample loading. A self-aligning monolithic device ensures precise manipulation of the droplet and high-efficiency injection of the nanoliter droplets into a capillary LC column for LC/MS-MS analysis. The design allows for both the printing of reagents in the droplet, thus incorporating processes such as cell lysis, protein reduction, alkylation, and digestion within the droplet, followed by direct collection and injection into the LC system, enabling high-efficiency proteomic analysis with minimal sample loss. Although this work showed excellent results, the setup designed is extremely specific and does not accommodate compatibility with different droplet arrays formats or platforms. This makes the experimental strategy very targeted rather than a broadly applicable solution, which goes against the main characteristic of droplet arrays: their high flexibility in experiment design.

This type of development shows a growing trend towards creating customized platforms to interface specific droplet arrays with non-optical analytical equipment. While these approaches increase adaptability for specific platforms and generate new ideas, they also highlight the significant shortcomings in terms of deployment and compatibility. This underscores the pressing need for accessible and standardized commercial technologies to address the so called “chip-to-world” [86] interaction.

Advancements in this area would significantly expand the field of miniaturization and parallelization in biological and chemical assays, paving the way for more efficient, versatile and sustainable research methodologies.

1.4. Research Purpose and Motivation

The objective of this thesis is to enhance the versatility and integration of the DMA platform for high-throughput biological assays. The initial focus is on establishing a digital twin for the DMA platform, aimed at predicting, controlling, and optimizing system behavior under various experimental conditions, thereby improving the reliability, applicability, and versatility of the DMA. Additionally, this thesis explores innovative methodologies such as the sandwiching

technique for droplet manipulation, which enables the development of new assays on the DMA. This technique allows for the handling of cellular structures between droplets and the integration of workflows with non-invasive and non-destructive sampling readouts. Furthermore, this work presents the development of an open-source device for the selective collection of droplets and their subsequent transport, storage and interface with non-optical analytical instruments. By addressing these aspects, this thesis aims to advance the field of miniaturization and parallelization in biological assays on the DMA, paving the way for new experimental methods and on-chip methodologies.

2. Results and Discussion

2.1. Digital Twin of a Droplet Microarray Platform: Evaporation Behavior for Multiple Droplets on Patterned Chips for Cell Culture

Disclaimer: This chapter, associated sections and images are published in [§1] and have been adopted for this thesis.

[§1] Wu Y, **Urrutia Gomez JE**, Zhang H, Wang F, Levkin PA, Popova AA, and Nestler B. Digital twin of a droplet microarray platform: evaporation behavior for multiple droplets on patterned chips for cell culture. Droplet. 2024; 3: e94. doi:10.1002/dro2.94

The author contributions were as follows: Urrutia Gomez JE performed the experiments, curated, analyzed the data, and wrote the paper. Wu Y, Zhang H and Wang F proposed the analytical model, performed the simulations, analyzed data, and wrote the paper. Popova AA, Levkin PA and Nestler B. proposed the original idea, acquired funding and corrected the manuscript.

Some of the content has been rewritten for a better understanding of this thesis work.

2.1.1. Introduction

2.1.1.1. Evaporation Dynamics of Droplet Microarrays: Effects of Wettability and Environmental Factors

Despite the benefits of miniaturization and parallelization, using the DMA platform presents several challenges. Common laboratory procedures, such as temperature cycles, sample incubation, and microscopy steps, become more complex due to the increased evaporation rate inherent in the miniaturized platform. The presence of multiple droplets in an array format can lead to non-uniform evaporation, causing variations in key parameters such as reagent concentration, pH, and cell culture volume. This variation introduces biases that are difficult to track and correct, affecting the reliability of experimental results.

To address these issues and improve control over the DMA platform, it is crucial to understand how wettability and environmental factors like humidity and temperature impact the evaporation of **multiple droplets** on patterned substrates. Recent research has focused extensively on these interactions, offering valuable insights.

One significant finding is that the distribution of droplets on a substrate can control evaporation kinetics. By varying the distance between them, it is possible to influence the rate at which the droplets evaporate. [87] For example, if the droplets are placed too close together, they may shield each other from evaporation. This effect is amplified when the droplets are surrounded by hundreds of other droplets that also interact with their neighbors. This interaction generates different evaporation rates depending on the position of each drop within the array, which may affect the uniformity of the experimental volume and, consequently, the final results.

Theoretical models indicate that the shielding effect [88] remains significant even when the distance between the centers of neighboring droplets is ten times the radius of the droplet base. [89] This means that a droplet located two or more positions away can still influence the evaporation rate of a distant droplet.

Additionally, as mentioned in *section 1.3.3*, the evaporation behavior on substrates is driven by two modes: constant contact radius and constant contact angle, which are determined by the surface's wetting properties. Therefore, the evaporation process is also influenced by the dynamics of the contact line where the droplet meets the surface. In practice, this is more complex, as droplets often evaporate in a combined mode known as the stick-slip mode, where the droplet alternates between sticking to the surface and slipping as it evaporates. [90]

Moreover, solving the problem of multiple droplet evaporation on DMA is very challenging due to their varying geometries. Most previous research has focused on droplets with circular contact lines, and there are limited analytical studies on the evaporation of droplets with other

shapes affected by the pinning effect. For example, Sáenz et al. explored the evaporation of nonspherical droplets both experimentally and numerically, but their work only considered the evaporation of a single droplet. [91]

2.1.1.2. Motivation and Aim

The aim of this work was to develop a comprehensive understanding and control of the DMA platform through both theoretical and experimental approaches, specifically for the control of biological experiments such as cell culture.

First, we proposed a theoretical model based on the phase-field model to describe the behavior of a single droplet situated in a square spot with sharp corners. Building on this, we developed a model for the behavior of multiple droplets on the same geometry. Using the insights from these models, we designed a digital twin for the DMA platform (Fig. 5). This digital twin allows the input of experimental data from the physical twin, such as humidity, ambient temperature, and initial droplet volume.

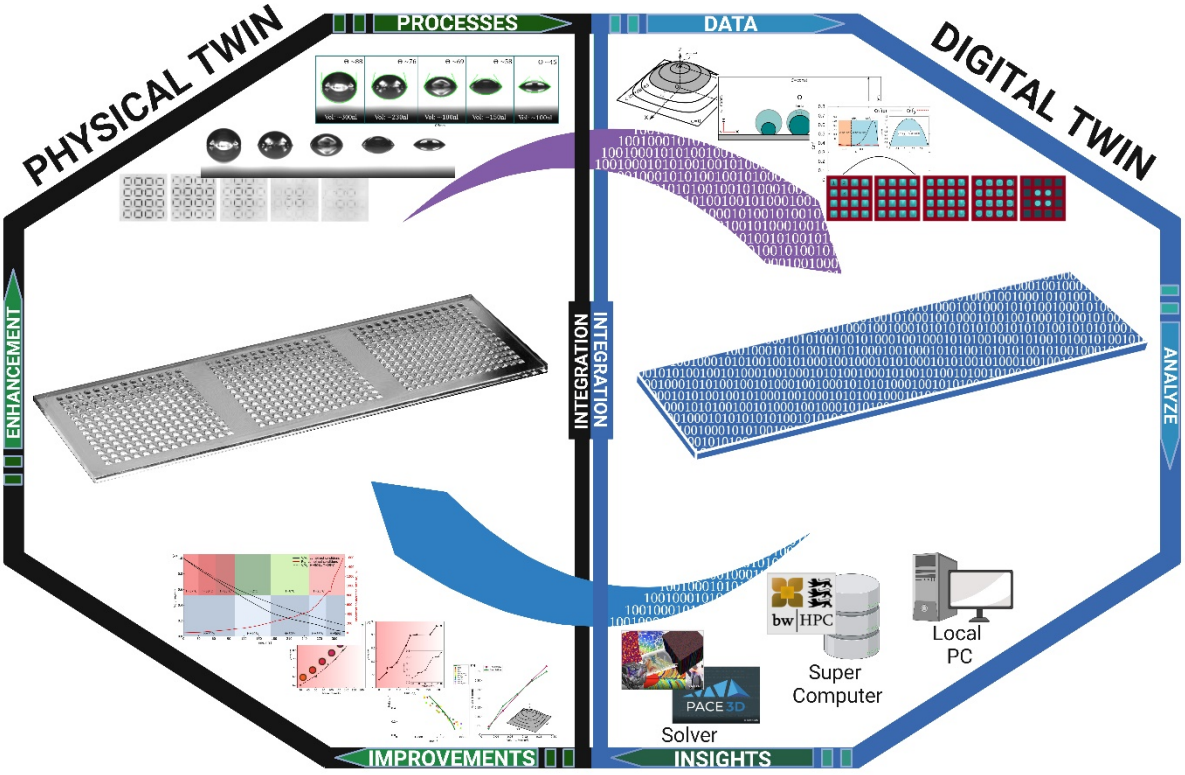

Figure 5. Interaction between digital twin and physical twin for the DMA platform. Experimental data from the physical twin is collected and used as input for modeling the digital twin. In the digital twin, this input data is evaluated, analyzed, and adapted through computer simulations. Once the digital twin is established, key parameters are varied to predict the evolution of droplet shapes and volumes under different conditions. These predictions guide the physical twin and provide insights for optimizing experimental conditions on the DMA platform.

In the digital twin, this data is evaluated and adapted through theoretical models and simulations conducted on either a local personal computer or a supercomputer. Once established, the digital twin allows us to vary key parameters to predict the evolution of droplet shapes and volumes under different conditions. This serves as a guide for the physical twin, providing valuable insights for optimizing experimental conditions on the DMA platform.

The primary aim of establishing this digital twin is to enable early prediction of the DMA's behavior under various experimental conditions. This allows users to anticipate and mitigate high evaporation risk events, thereby maintaining better control over their experiments throughout the procedures.

2.1.2. Phase-Field Model

The phase-field model is a powerful mathematical tool used to describe and simulate the evolution of interfaces and phase transitions in material systems. This model allows for a continuous representation of the interfaces between different phases, thus avoiding the need to explicitly track moving boundaries, which significantly simplifies numerical calculations. [92]

In the context of droplet evaporation on functionalized surfaces, the phase-field model is employed to capture the dynamics of the liquid-gas interface of the droplets. This approach is particularly useful for describing the behavior of droplets in contact with heterogeneous substrates and complex patterns. [93] In our study, contour curves were used to represent the equilibrium shape of the droplet, as shown in figure 6.

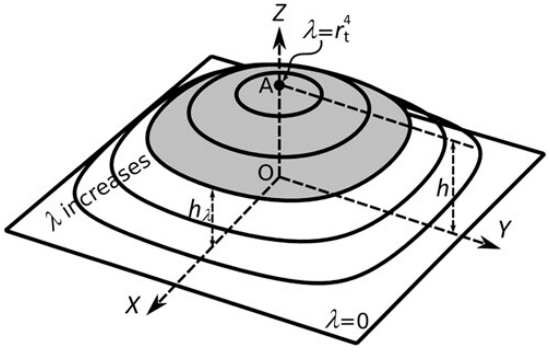

Figure 6. Diagram of the equilibrium droplet shape on a square-patterned substrate within a three-dimensional coordinate system (OXYZ). Contour lines represent the liquid–gas interface. Point A marks the apex of the droplet, and h indicates the droplet height. When $h_\lambda = 0$, the contour curve approaches a square, while as h_λ increases, the curves become smoother and rounder, becoming circular near the apex or the droplet.

$$(y - r_t)(x + r_t)(x - r_t)(x + r_t) - \lambda = 0 \qquad (2.1)$$

The parameter r_t represents the radius of the inner tangent circle of the square pattern. The parameter $\lambda \in [0, \lambda_{max}]$ governs the roundness of the curve, which is linked to the height h_λ ($h_\lambda \in [0, h]$), as proposed in the equation

$h_\lambda(\lambda) = h_\lambda / \lambda_{max}$. Here, h denotes the droplet height and $\lambda_{max} = r_t^4$ is the maximum value of λ. The volume of the droplet, V, is calculated using the integral $V = \int_0^h A(h_\lambda) dh_\lambda$, where $A(h_\lambda)$ represents the surface area for the droplet cross-section at height h_λ. Given a certain volume V and a base pattern, the height h can be determined. Adapted from Wu et al. [§1]

The model is based on the definition of an order parameter, which in this case is the relative concentration of the liquid and gas phases. This order parameter evolves according to a partial differential equation that minimizes the free energy of the system. The free energy consists of terms describing both the volumetric energy of the phases and the interfacial energy. Mathematically, this is expressed through a free energy functional that includes a double-well function to represent the phases in equilibrium (liquid and gas).

The liquid-gas interface is described by a series of contour curves obtained by slicing the droplet cap with flat surfaces parallel to its base. These curves vary from a square shape at the base to a circular shape at the apex of the droplet, controlled by a parameter λ (Fig. 6).

2.1.2.1. Phase-Field Model of *Cahn-Hilliard* Type

The *Cahn-Hilliard* type phase-field model is a specific extension of the phase-field model, designed to capture phase separation phenomena and interfacial dynamics in binary systems. This model is particularly suitable for describing droplet evaporation, where the transition between liquid and gas phases plays a crucial role. [94]

The free energy functional of the system is expressed as:

$$F = \int_\Omega [f(c) + 2\sigma\epsilon(\nabla c)^2] d\Omega \tag{2.1}$$

where Ω is the spatial domain, ϵ is the interface width, and $f(c)$ is the free energy density, represented by a double-well function with minima at concentrations c_{e1} and c_{e2}.

The *Cahn-Hilliard* equation governing the evolution of the order parameter c is:

$$\frac{\partial c}{\partial t} = \nabla \cdot (M \nabla \mu) \tag{2.2}$$

where μ is the chemical potential given by:

$$\mu = \frac{\delta f}{\delta c} = f'(c) - \epsilon^2 \nabla^2 c \tag{2.3}$$

At the fluid-substrate interface, a boundary condition is set to capture the surface tension and interactions with the substrate:

$$4Cn\nabla \cdot n - \left(\gamma_{sg} - \gamma_{sl}\right)\frac{l'(c)}{\gamma_{lg}} = 0 \qquad (2.4)$$

Here, as mention in *seccion 1.2.2*, γ_{sg} and γ_{sl} are the solid-gas and solid-liquid interfacial tensions, respectively, and γ_{lg} is the liquid-gas interfacial tension.

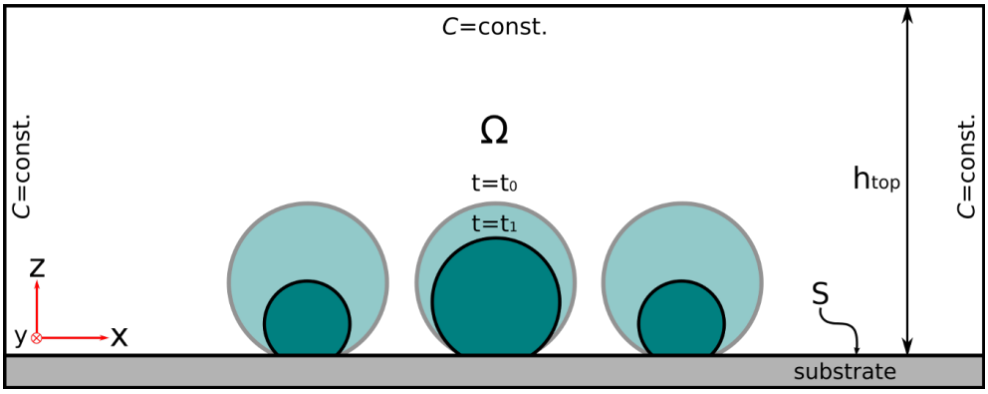

Figure 7. Cross-sectional view of the 3D computational domain showing the setup for simulating droplet evaporation on a patterned substrate. The diagram illustrates the initial release and subsequent non-uniform evaporation of droplets. The figure depicts three droplets at different stages of evaporation on the substrate. At the initial time t = t_0, droplets of uniform size are placed on the substrate. As time progresses to t = t_1, the droplets begin to evaporate non-uniformly due to the shielding effect caused by the proximity of adjacent droplets. The boundary S represents the interface between the computational domain Ω and the substrate. The top and side boundaries of the domain are maintained at a constant concentration (c = const.). The height h_{top} denotes the distance from the top of the domain to the substrate. The non-uniform evaporation behavior observed in the droplets is influenced by the patterned nature of the substrate and the initial conditions. Adapted from Wu et al. [§1]

2.1.2.2. Simulation

Simulations using this model demonstrate how droplets evaporate non-uniformly on substrates with different patterns. Figure 7 illustrates the cross-sectional view of the 3D computational domain, where the described boundary conditions are applied.

Initially, droplets of uniform size are pinned on the substrate, and subsequently, they evaporate non-uniformly due to the shielding effect from the proximity of other droplets and substrate characteristics. This behavior can be quantitatively analyzed using the free energy function represented in Figure 8, which shows the energy minimum states corresponding to the liquid and gas phases.

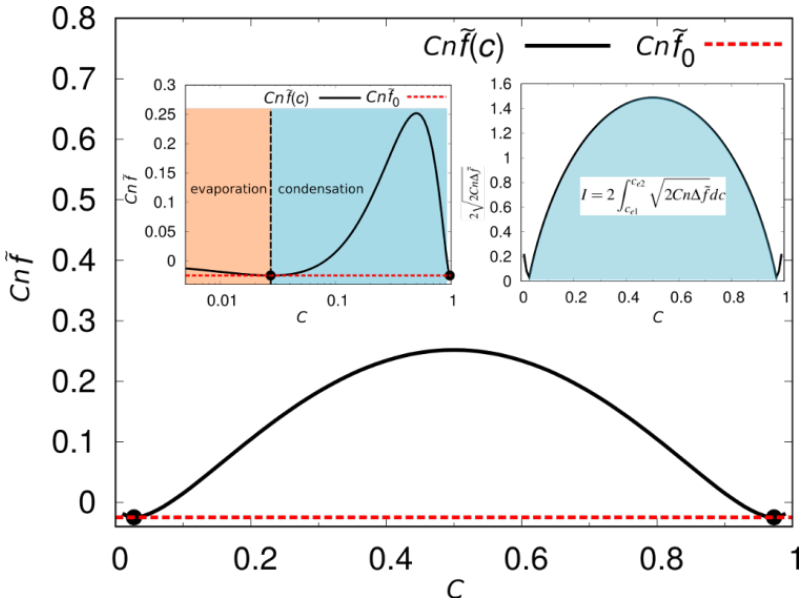

Figure 8. Free energy landscape and phase transition zones for droplet evaporation and condensation. The figure depicts the free energy $\tilde{f}$ as a function of the order parameter c, described by the equation (2.5). The points P_1 and P_2, marked by black circles, indicate the free energy minima corresponding to the bulk gas and liquid phases. The left inset provides a logarithmic scale view of the double-well function for the order parameter c. This visualization differentiates the evaporation (orange) and condensation (blue) zones, demonstrating the energy landscape in these two regions. The right inset illustrates the integration of the excess free energy, using the equation (2.8), to calculate the surface tension γ_{lg}. Adapted from Wu et al. [§1]

The free energy as a function of the order parameter c is given by:

$$Cn\tilde{f}(c) = c\ln c + (1-c)\ln(1-c) + 3.78c\,(1-c) \tag{2.5}$$

The two points $P_1(c_{e1}, Cn\tilde{f}(c_{e1}))$ and $P_1(c_{e2}, Cn\tilde{f}(c_{e2}))$ highlighted by black circles are the free energy minimum states, corresponding to the gas and liquid bulk phases, respectively. The left inset replots the double-well function with the c-axis in log-scale (Fig. 8), indicating the evaporation and condensation zones. The right inset illustrates the integration of the excess energy:

$$\gamma_{lg} = \int_{-\infty}^{+\infty} (\Delta f + 2\sigma\epsilon(\frac{\partial c}{\partial x})^2)\,dx \tag{2.6}$$

Where $\Delta f = f(c) - f_0$ and $f_0 = f(c_{e1}) = f(c_{e2})$. At equilibrium, we obtain:

$$\gamma_{lg} = \int_{c_{e1}}^{c_{e2}} \sqrt{2Cn\Delta\tilde{f}}\,dc = \sigma \cdot I \tag{2.7}$$

where

$$I = 2\int_{c_{e1}}^{c_{e2}} \sqrt{2Cn\Delta\tilde{f}}\,dc \tag{2.8}$$

By setting the integration $I = 1$, we have $\gamma_{lg} = \sigma$. An alternative double-well function $f(c)$ is given by:

$$\tilde{f}(c) = \frac{1}{Cn}\,(c\ln c + (1-c)\ln(1-c) + Xc(1-c)) \qquad (2.9)$$

With $X = 3.78$, $c_{e1} = 0.0273$, and $c_{e2} = 0.9727$.

To drive the evaporation and condensation, we assume a linear relationship between the ambient humidity H and the order parameter c_0, so that $H = \frac{c_0}{c_{e1}}$. When $c_0 < c_{e1}$ (evaporation) or $c_0 > c_{e1}$ (condensation), the corresponding process will occur, driven by constant chemical potential flux.

2.1.3. Evaporation Dynamics of Droplets on a Square Hydrophilic Spot

2.1.3.1. Single Droplet Evaporation

The current model is validated by simulating the evaporation of a single droplet within a 1 mm^2 square hydrophilic spot. The simulation results are compared to experimental data. The droplet used in this study is a water-based solution containing 5% glycerol by volume. Glycerol is added to the water to slow down the evaporation rate, facilitating better control of the initial droplet height during experimental measurements. Figures 9a and 9b show the simulation and experimental snapshots, respectively, of a droplet evaporating at a humidity level of 36%, which represents the typical laboratory conditions. Throughout the evaporation process, the droplet completely occupies the hydrophilic spot, indicating a constant contact radius mode of evaporation. Additionally, the normalized height (h/h_0) and the contact angle versus evaporation time (t, in seconds) for this droplet are plotted in Figure 9c. In this figure, circles represent experimental data, while solid lines represent simulation results. The findings indicate that the simulation closely matches the experimental data.

At the final stages of e, the droplets become very small, leading to a larger ratio of interface width to droplet size, potentially decreasing modeling accuracy. Furthermore, in the experiments' final stages, the solution thickens, and dehydration of salts occurs, making the evaporation process more complex than at the initial stage. But this complex process goes beyond the scope of this work, therefore it was neglected. The noticeable deviation between simulation and experimental contact angles in the final stage can be attributed to the phase-field model used, as explained in the previous sections can only considers diffusion and not fluid dynamics. During the simulation, the time scale for surface tension and fluid flow effects is assumed to be much larger than the diffusion process, causing slight deviations in droplet shape from equilibrium. Additionally, contact angle hysteresis caused by surface defects or

irregularities leads to deviations in contact angle and droplet shape. Despite these deviations, the overall good agreement between simulation and experimental results demonstrates the robustness and validity of the phase-field model developed in this study for describing the evaporation of a single droplet on a chemically patterned DMA surface.

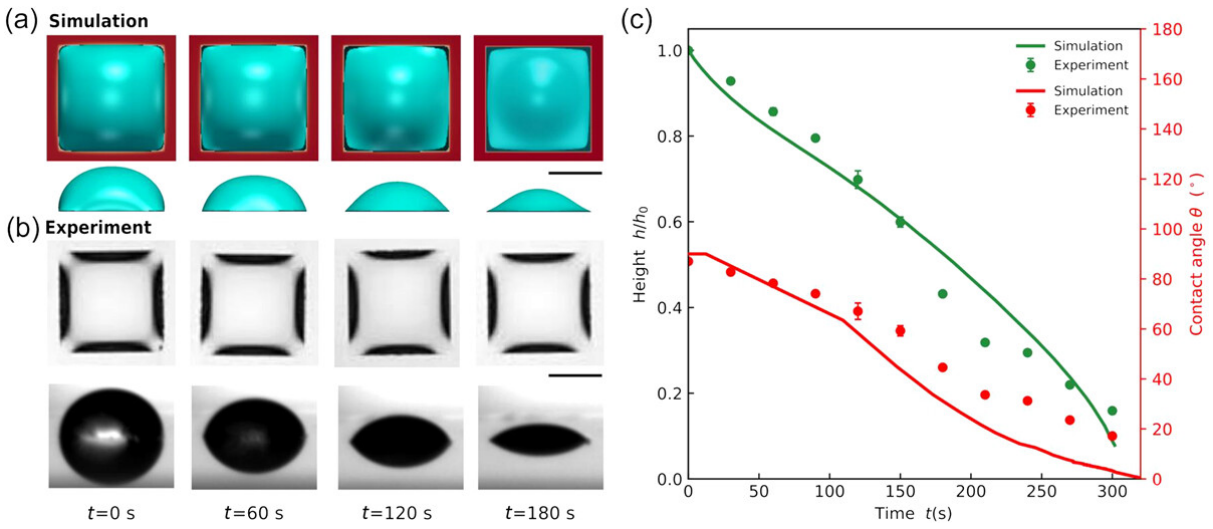

Figure 9. Comparison of simulation and experimental outcomes for the evaporation of a single glycerol droplet on a square-patterned substrate. (a) The first and second rows depict the top and side views of the simulated evaporating droplet at various times, respectively. (b) Corresponding experimental observations. The square spot measures 1 mm². Throughout the evaporation process, the droplet completely occupies the hydrophilic spot, indicating a constant contact radius mode of evaporation. (c) Time progression of the normalized droplet height (h/h_0) and contact angle (θ). Here, h_0 (h_0 = 0.47 mm) and h (mm) represent the initial and transient droplet heights, respectively. Simulation results are shown with solid lines, while experimental results are marked by dots with error bars. The coefficients of determination (R^2) for droplet height and contact angle are 0.9582 and 0.7861, respectively. Scale bars: 0.5 mm. Adapted from Wu et al. [§1]

Similarly, as depicted in Figure 10a, we performed a series of evaporation experiments on single droplets using various solutions frequently employed in laboratory settings, such as saline buffers and cell culture media, both with and without cells. After collecting the height evolution data, we plotted the normalized droplet height (h/h_0) against the nondimensionalized time ($\tilde{t}$), represented by different-colored circles. Here, the scaled time ($\tilde{t}$) is defined as $\tilde{t} = tD_e/x^{*2}$, where D_e (m^2/s) and x*(m) represent the effective diffusion coefficient and the characteristic length, respectively.

The colored circles on the graph in Figure 10a align with a master curve that matches the simulation result (solid curve). In our simulations, we solve the diffusion equations, demonstrating the diffusion-dominated nature of the evaporation processes for the liquids considered in this study. By comparing the simulations with the experimental results for various liquid solutions, we identified the effective diffusion coefficient (D_e), as listed in Table 1. It is important to note that the D_e used here is a modeling parameter in the simulation and

differs from the actual diffusion coefficient for the system under investigation. The physical value describing the diffusion of one substance into another is typically determined experimentally. [95]

Liquids	*Water*	*Glycerol*	*DMEM*	*DMEM$_{100}$*	*NaCl$_{0.1}$*	*NaCl$_2$*	*NaCl$_5$*
$D_e/(10^{-8}\ m^2/s)$	1.88	1.32	1.58	1.27	1.73	1.56	1.29
$D_e/D_{e,water}$	1.00	0.70	0.84	0.68	0.92	0.83	0.69

Table 1. Effective diffusion coefficients (D_e) for various liquids were determined by comparing experimental results with phase-field (PF) simulations. The accompanying number for Dulbecco's Modified Eagle Medium (DMEM) indicates the number of HeLa-CCL-2 cells present in the droplet. The numbers accompanying NaCl represent the molar concentration per liter of pure water. These concentrations were selected to cover a range from low to saturated salt concentrations.

In our study, we assumed the solution is dilute, and the late stage of the evaporation is not the focus. Therefore, to simplify the model, the effective diffusion coefficient is considered constant. Among the liquid solutions listed in Table 1, water exhibited the fastest evaporation with the highest D_e, while the aqueous solution of 5% glycerol evaporated more slowly, showing a lower D_e. For the DMEM cell culture media, increasing the cell concentration reduced diffusivity, similar to increasing the NaCl concentration in water.

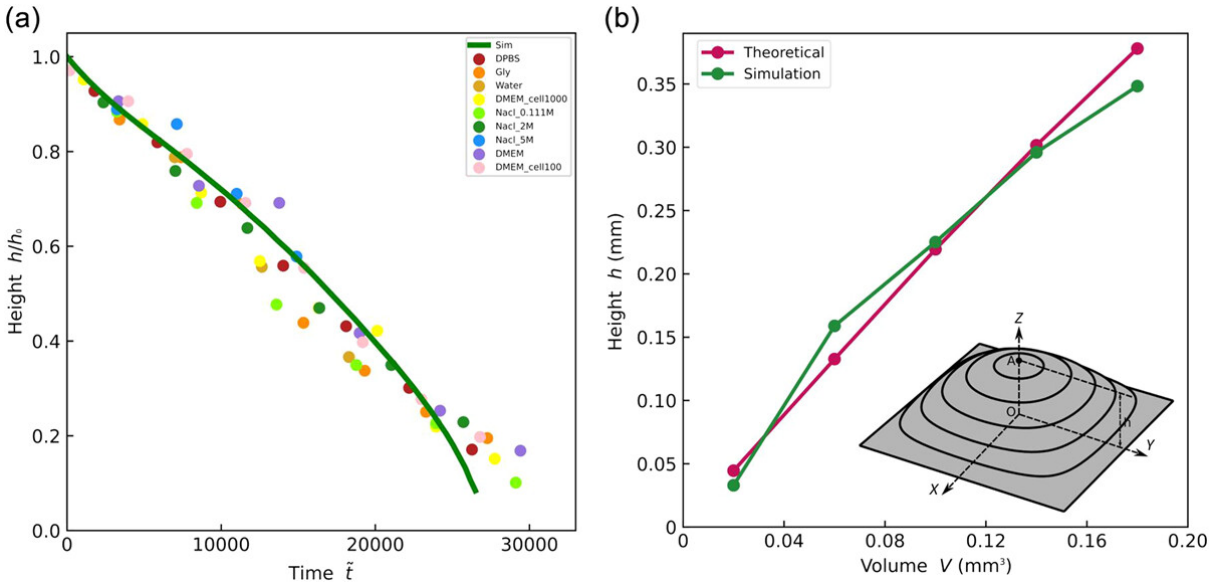

Figure 10. Analysis of the morphology of a single droplet on a square-patterned substrate. (a) Normalized droplet height h/h_0 (h_0 = 0.47 mm) as a function of non-dimensionalized time. The solid line represents the simulation result, while the colored circles indicate the experimental results obtained from different droplet compositions. The coefficients of determination R^2 range from 0.9194 to 0.9910. (b) Droplet height as a function of volume for an equilibrium droplet on a square-patterned substrate. The red and green points represent theoretical and simulation results, respectively. The coefficient of determination R^2 is 0.9696. The inset in (b) shows a schematic of an equilibrated droplet described by the theoretical model. The droplets in the simulations and the theoretical

model fully occupy the superhydrophilic square spot, which is valid for all studied liquids within the considered volume range. Cell (100–1000): Number of HeLa cells in the drop; DMEM: Dulbecco's Modified Eagle Medium; DPBS: Dulbecco's Phosphate-Buffered Saline; Gly: Aqueous solution of pure water with 5% glycerol vol/vol; NaCl (0.1, 2, 5 M): Sodium chloride at different molar concentrations in water; Sim: Simulation. Adapted from Wu et al. [§1]

Effective management of evaporation on the DMA platform is crucial, as solute concentration and pH levels in each droplet of cell culture media are significantly influenced by droplet volumes. Despite the challenge of measuring the volume of individual droplets on a square spot over time, we propose a theoretically quantifiable model that correlates droplet volume with droplet height. The model represents droplet shape through a series of contour lines as mentioned in *section 2.1.2*, and as depicted in the schematic inset of Figure 10b. The theoretical model's predicted relationship between droplet height and volume, indicated by the red line in Figure 10b, aligns with results from phase-field simulations shown by the green line.

2.1.3.2. Multiple Droplet Evaporation

We additionally verified our phase-field model for simulating the evaporation of multiple droplets by comparing it with experimental results. Figures 11a and 11b display snapshots of the multiple droplet evaporation processes from phase-field simulations and experiments, respectively. The droplets in the center exhibit a slower evaporation rate due to the presence of neighboring droplets, leading to nonuniform evaporation. This phenomenon of non-uniform evaporation is caused by the shielding effect as mentioned in *section 2.1.1.1*. Figure 11c quantitatively illustrates the evaporation processes (evolution of normalized height) for droplets at positions 1, 2, and 3, as highlighted in the first image of Figure 11a. The solid lines and circles represent the simulation and experimental results, respectively. The results for the droplets at different positions are depicted in different colors (1, red; 2, green; 3, blue). There was a strong agreement between the simulations and experimental data, and the shielding effect was accurately reproduced in the phase-field simulation. The deviations observed during the early stages of evaporation are attributed to the accumulation of the vapor phase around the droplet array in the experiments during the observational period, whereas in the simulations, there is no initial accumulation of the vapor phase, resulting in a relatively low vapor concentration that accelerates the evaporation in the simulations.

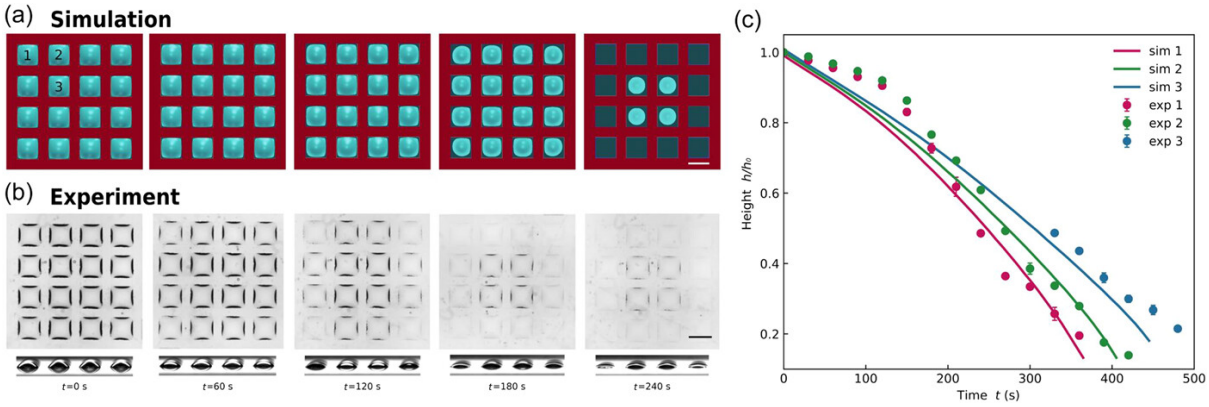

Figure 11. Comparison of the evaporation process for multiple droplets on a square-patterned substrate. The square spots are 1 mm² in size, arranged in a 4 × 4 pattern configuration with an edge-to-edge distance of D = 0.5 mm. (a, b) Simulation and experimental results, respectively. (c) Time evolution of the normalized droplet height h/h_0 (h_0 = 0,47 mm) for the droplets at positions 1, 2, and 3, as highlighted in the first image of (a). The solid lines and circles represent the simulation and experimental results, respectively. The results for the droplets at different positions are indicated by different colors: 1 (red), 2 (green), 3 (blue). The coefficients of determination R^2 for the results of droplets at positions 1, 2, and 3 are 0.9812, 0.9254, and 0.9533, respectively. Scale bars: 1 mm. Adapted from Wu et al. [§1]

Thereafter, we systematically examined the effects of humidity, temperature, and the distance between droplets on the evaporation process to enhance control over droplet formation and evaporation behavior. Figures 12a and 12b illustrate the evaporation processes (h/h_0 vs. t) at a humidity level of 36% for droplets arranged in 2 × 2 and 4 × 4 patterns, respectively. In Figure 12a, the curves in different colors represent various distances between the droplets D (mm). Due to the symmetric positioning in the 2 × 2 pattern, the four droplets evaporate uniformly. It is further noted that as D decreases (from 0.5 to 0.2 mm), the normalized height h/h_0 of the droplets decreases more slowly, indicating a reduction in the evaporation kinetics. A smaller distance between droplets enhances the shielding effect, leading to a higher local vapor concentration, which slows the diffusion process of water from the droplets to the surroundings.

A similar trend is observed in Figure 12b for the 4 × 4 pattern, although the evaporation kinetics for droplets at positions 1, 2, and 3 differ. These are depicted by the various line types in Figure 12b. The droplets at position 3 (solid lines) evaporate more slowly than those at positions 1 and 2 (dashed lines) for both studied distances D. Note that the curves for droplets at position 3 with different D (solid lines) diverge more than those for droplets at positions 1 and 2 (dashed lines). This indicates that droplets at position 3 are more sensitive to variations in D than those at positions 1 and 2. Additionally, as D increases from 0.2 to 0.5 mm, the divergence among the evaporation curves for droplets at different positions decreases. It is expected that uniform evaporation would occur at a very large value of $D = \infty$, displaying the same evaporation

kinetics as a single droplet with the fastest evaporation behavior, whereas nonuniform evaporation is observed at smaller D values, such as D = 0.2 and 0.5 mm.

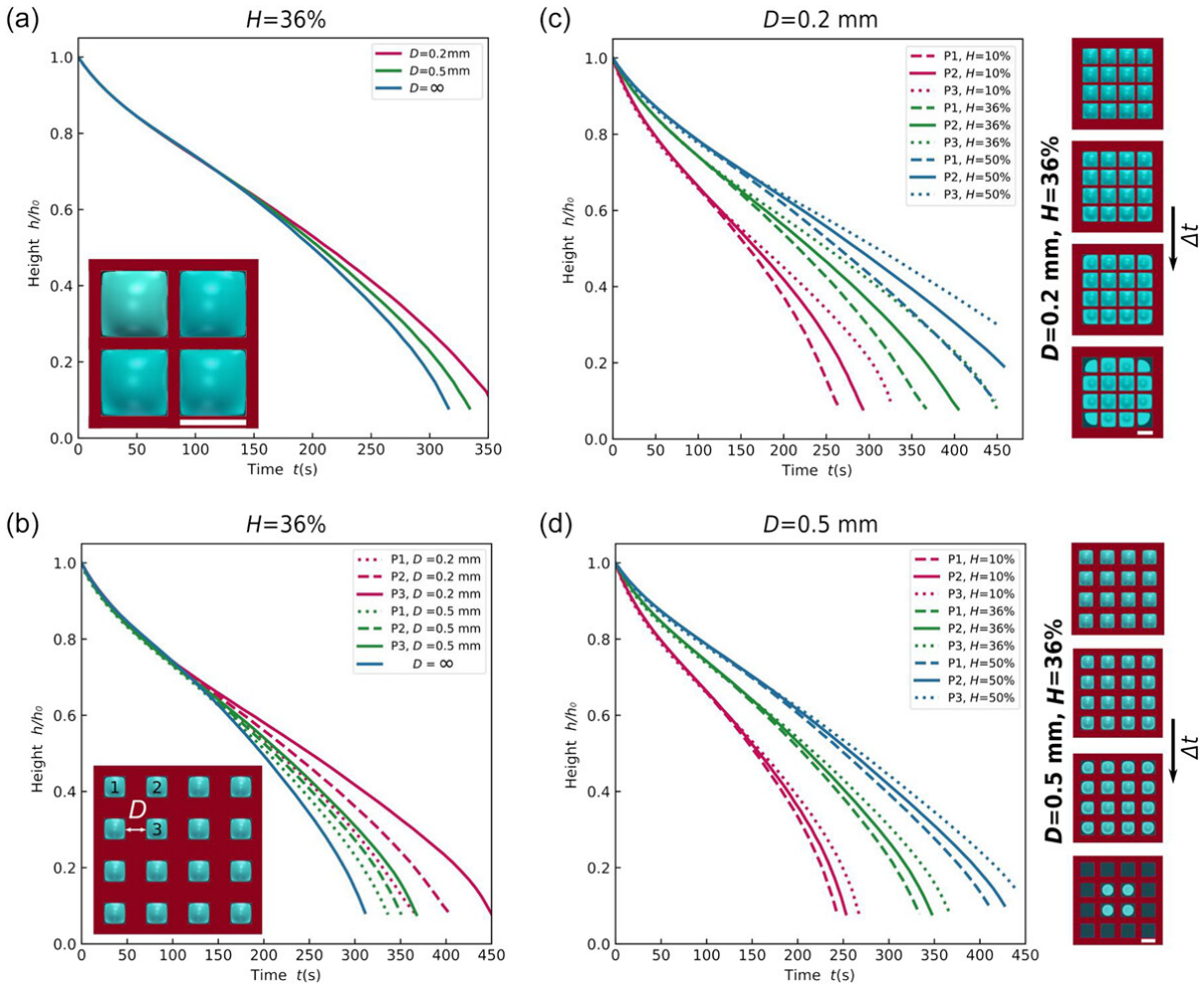

Figure 12. Simulation of the impact of droplet distance D and humidity H on the evaporation process. (a, b) Time evolution of the normalized droplet height for evaporating droplets under a consistent humidity of H = 36 % but with varying droplet distances. Initially, we examine 4 droplets arranged in a 2 × 2 pattern and 16 droplets in a 4 × 4 pattern, all with the same initial height of h_0 = 0.47 mm in (a) and (b), respectively. D = ∞ represents the results for single-droplet evaporation. (c, d) Evaporation behaviors for the 16 droplets under different humidity levels but with fixed droplet distances ([c] D = 0.2 mm; [d] D = 0.5 mm.) The snapshots adjacent to the plot diagrams show top views of the 16 evaporating droplets under H = 36% with the respective droplet distances. Scale bars: 1 mm. Adapted from Wu et al. [§1]

In addition to the position of the droplet within the array and the distance between the droplets, the environmental humidity H significantly influences evaporation behaviors. Figures 12c and 11d illustrate the effect of environmental humidity on the evaporation process of multiple droplets arranged in a 4 × 4 pattern with D = 0.2 and D = 0.5 mm, respectively. Each diagram uses different line types to distinguish the results for droplets at various positions, and different colors to represent the results under different humidity levels (red: H = 10%, green: H = 36%, blue: H = 50%) It is observed that lower environmental humidity markedly accelerates the evaporation process. However, the divergence among the three groups of evaporation curves

for droplets at different positions but under the same humidity level (either red, blue, or green) remains nearly the same. This indicates that environmental humidity has a minor impact on the shielding effect.

The extent of divergence of the evaporation curves with the same color (i.e., under the same humidity) depends solely on the distance between droplets *D*. In summary, while the evaporation rate is closely linked to environmental humidity, the variation in evaporation rates for droplets at different positions is influenced by droplet distance, as the shielding effect is more related to local humidity than to the overall environmental humidity. This shielding effect can be reduced by increasing the droplet distance. For very large distances between droplets, the shielding effect can be neglected, ensuring ideal parallelization on the DMA. However, due to computational limitations for very large domains, this cut-off distance was not studied in this work. Nevertheless, the shielding effect slows down evaporation, which is beneficial for maintaining a stable culture environment.

To study evaporation under varying temperatures, our model was expanded by linking the effective diffusion coefficient D_e to temperature T (K) as described by Smith et al. [96]:

$$D_e = \frac{0.01498T^{1.81}\,(1/M_A + 1/M_B)^{0.5}}{P(T_{cA}T_{cB})^{0.1405}\,(V_{cA}^{0.4}+V_{cB}^{0.4})^{0.5}} \tag{2.10}$$

where P (N/m²) is the pressure. The parameters M_i (g/mol), T_{ci} (K), and V_{ci} (m³/mol) are the molecular weight, critical temperature, and critical molar volume of component i ($i = A, B$), respectively. In this study, we assume that the temperature and pressure vary within a small range. Therefore, the parameters P, M_i, T_{ci}, and V_{ci} are constant values, leading to $De \propto T^{1.81}$. Based on the value of D_e at room temperature (T = 298 K), we can calculate D_e for other temperatures. Here, we demonstrate the concept of extending the phase-field model by incorporating an empirical equation supported by experiments. This empirical equation, implemented within the phase-field model, is a key parameter that narrows the gap between the real DMA platform (physical twin) and the digital twin.

2.1.4. Digital Twin of the Droplet Microarray

As a primary goal of developing a DMA digital twin, we applied our model to describe a real-life wet lab scenario. Figure 13a presents the simulation of the evaporation kinetics of a single DMEM cell culture droplet on a square pattern. This simulation demonstrates how the droplet is subjected to various typical experimental conditions such as temperature and humidity,

simulating refrigeration, incubation, and room temperature manipulations. The solid black line represents the evolution of the normalized volume V/V_0 under the specified conditions, with different time intervals highlighted in different colors in Figure 13a. The dot-dashed red line shows the variation in solute concentration (e.g., cell culture media components or drugs in screening applications) as the volume changes, calculated using the dilution equation $cd_1 V_1 = cd_2 V_2$ and the equation $Rc_d = (C_{d2} - C_{d1}) / C_{d1}$ at each point. Here, C_{di} (mol/m³) and V_i (m³) are the concentrations and volumes at time t_i (i=1 or 2). Rc_d indicates the concentration increase rate.

The dashed green line is a theoretical prediction for V/V_0 evolution under combined conditions of temperature and humidity, while the dashed black line represents V/V_0 evolution under constant conditions of H = 50% and T = 25°C. The theoretical prediction is based on a diffusion-based evaporation model, which assumes the rate of droplet volume change $\dot{V_{Sim}}$ (m³/s) is proportional to the effective diffusion coefficient D_e, droplet base radius R_b (mm), vapor concentration difference Δ_c, and geometric factor $f(\theta)$, related to the contact angle. Thus, $\dot{V_{Sim}} \propto D_e R_b f(\theta) \Delta_c$. Throughout the evaporation process, R_b is constant, Δ_c is proportional to relative humidity H, and D_e for different temperatures is calculated as $D_e \propto T^{1.81}$. To simplify the contact angle influence, we use $f1(\theta)$ and $f2(\theta)$, for large ($V/V_0 \geq 0.3$, t = 0 –184 s) and small contact angles ($V/V_0 \leq 0.3$, t = 184 – 326 s). By fitting the evaporation rates at typical intervals t = 76 – 110 s (for large angles) and t = 184 – 256 s (for small angles) with simulation results, we can calculate evaporation rates for other intervals, as listed in Table 2. The simulated volume change rates agree well with theoretical predictions. The green dashed line in Figure 13a is derived by assuming the same initial volume and using theoretically predicted evaporation rates from Table 2.

From 0 to 110 s, the humidity is the same for the solid and dashed black lines, but the temperature is higher for the solid black line, causing a slightly faster decline due to heating. The similar volume changes for heated cases (37°C and 50°C) compared to 25°C (dashed black line) are due to the delayed evaporation response when switching temperatures, as the vapor phase transport needs time to establish a new quasi-static state. From 110 to 184 s, despite a cooling effect at 2°C, the solid black line declines faster due to very low humidity (H = 10%), driving the diffusion process. From 184 to 256 s, with the same humidity but lower temperature, the solid black line declines slightly slower, showing a cooling effect. From 256 to 293 s, the solid black line declines quicker due to lower humidity. In the final stage, both

curves decline nearly in parallel as they have the same temperature and humidity. The green dashed line aligns well with the solid black line, with slight deviations due to delayed evaporation response from switching conditions. Throughout the evaporation process, the solute concentration change rate is inversely proportional to volume variation. As shown in Figure 13c, this solute variation in DMEM increases the solution's pH.

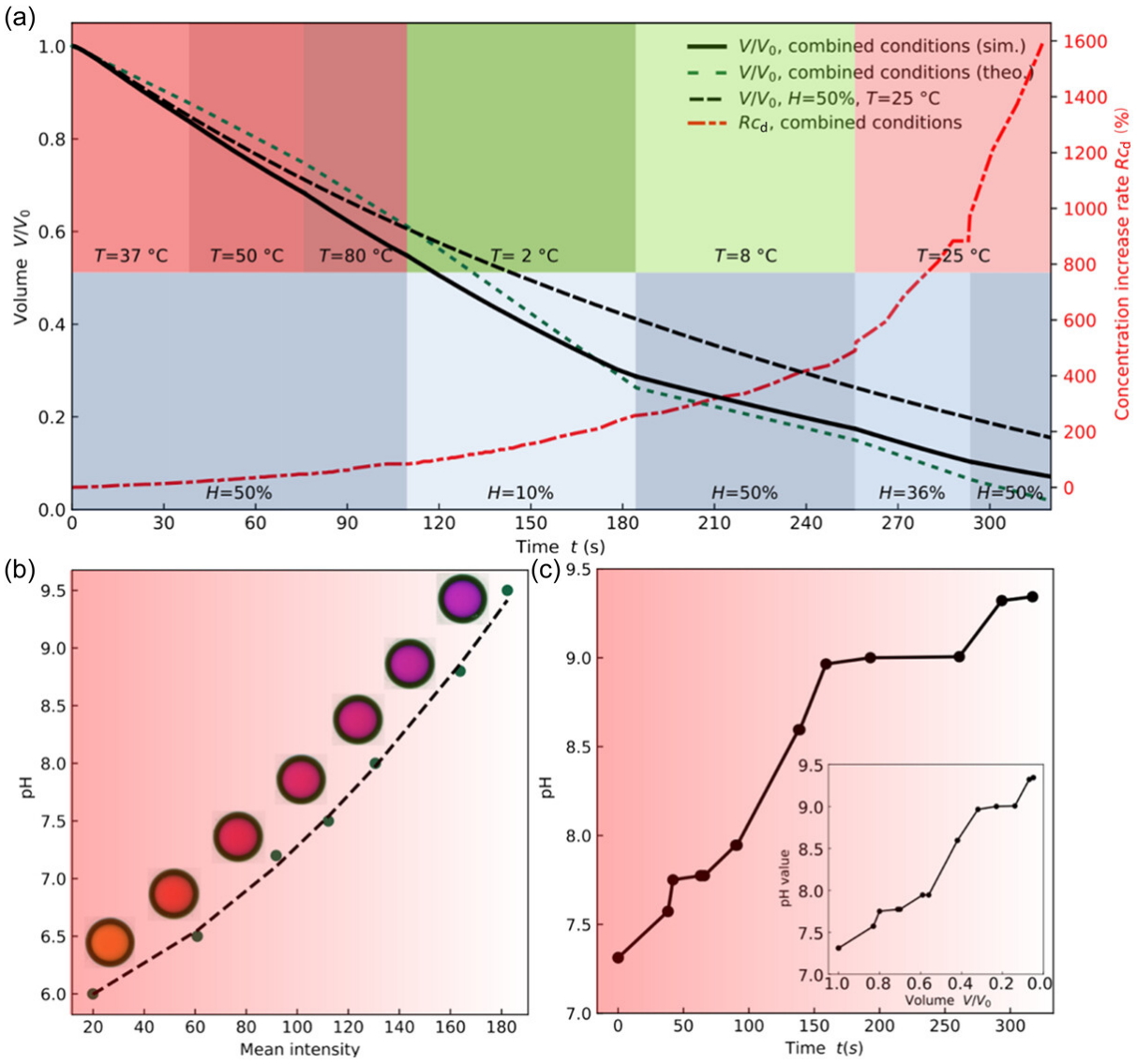

Figure 13. Combined influence of temperature (T) and humidity (H) and monitoring of droplet pH. (a) Simulation of evaporation dynamics for a single droplet on a square-patterned substrate under various T and H conditions. Droplets of Dulbecco's Modified Eagle Medium (DMEM) cell culture media are used. The solid black line represents the simulation result under standard laboratory conditions, with given temperature and humidity at different stages highlighted in different colors. The dashed green line shows the theoretical prediction under the same conditions. The dot-dashed red line indicates the concentration change rate of a solute (e.g., cell culture components, drugs) under the same conditions. Specific conditions include T = 37°C; H = 50% for cell culture incubator conditions, T = 50°C/T = 80°C; H = 50% for the heating process during cell lysis by thermal shock, T = 2°C; H = 10% and T = 8°C; H = 50% for the cooling process to complete cell lysis mediated by thermal shock, T = 25°C; H = 36% for sample manipulation post-thermal shock under a microscope, and T = 25°C; H = 50% for the liquid printer microenvironment to print new reagents in each droplet. The black dashed line indicates a reference simulation result under H = 50% and T = 25°C. (b) Functional relationship between the mean intensity of droplet color and pH value. pH values for droplets of different volumes are individually measured in

experiments, with the fitting function indicated by the dashed line and a coefficient of determination $R^2 = 0.9973$. (c) Evolution of pH value during the droplet evaporation process. The initial state of the evaporating droplet corresponds to the third case in (b), with pH = 7.3. Measured pH values are based on intensity measurement, and the inset shows the functional relationship between pH value and droplet volume. Adapted from Wu et al. [§1]

Time intervals	***0-38s***	***38-76s***	***76-110s***	***110-184s***	***184-256s***	***256-293s***	***293-326s***
Conditions (T; H)	37°C; 50%	50°C; 50%	80°C; 50%	2°C; 10%	8°C; 50%	25°C; 36%	25°C; 50%
$\dot{V}_{sim}$ $/(10^{-3}mm^3/s)$	4.95	4.95	4.81	4.19	1.87	2.23	1.43
$\dot{V}_{theo}$ $/(10^{-3}mm^3/s)$	3.80	4.10	4.81	5.51	1.87	2.66	2.07

Table 2. Evaporation rates obtained from simulation results $\dot{V_{sim}}$ and theoretical predictions $\dot{V_{theo}}$ under standard laboratory conditions with specified temperature (T) and humidity (H) at various time intervals.

The pH level of the culture medium is a critical factor influencing various cellular processes necessary for cell growth and survival. Fluctuations in pH levels can impact nutrient solubility and availability, metabolic pathways, and protein folding, all of which are vital to cellular functions. In cellular assays conducted in small droplets, even slight volume changes can cause significant fluctuations in metabolite and salt concentrations, leading to pH changes. Thus, accurately monitoring pH variations during the evaporation process is essential to optimize cell culture conditions and improve cell assay performance within droplets.

In this study, we measured the pH of DMEM droplets containing a pH indicator, without cells, to track pH evolution throughout the evaporation process. Figure 13b illustrates the changes in mean color intensity of DMEM droplets with a pH indicator during evaporation. pH measurements and color intensity analyses were conducted on a single droplet, reflecting the behavior of individual droplets within an array where droplet distances exceed the cutoff distance.

We related pH value to mean intensity using a fitting function: $\mathrm{pH} = aM^2 + bM + m$ with a, b and c are fitting parameters, and M represents the mean color intensity. Using this correlation, we traced pH changes in droplets throughout the evaporation process. Figure 13c plots the pH evolution, with the inset showing the relationship between droplet volume and pH value.

Experimental droplet volumes for pH calculation were determined by measuring droplet height, correlating real-time height data with mean intensity during evaporation. It is important to highlight that our goal was to introduce a real-time method for monitoring pH and solute concentration changes in a droplet, closely associated with volume variations. This method is applicable whether the droplet under study is a single droplet or part of a droplet array, as long as the droplet volume can be detected.

2.1.5. Summary and Conclusion

In this chapter, we demonstrate that accurate droplet volume control can be achieved through careful management of the evaporation process. We investigated the evaporation behavior of droplets on a DMA both experimentally and numerically, under various conditions by adjusting environmental humidity, temperature, and wetting properties. Notably, the phase-field simulations showed excellent agreement with experimental results for the evaporation of single and multiple droplets on a patterned substrate. Specifically, multiple droplets on patterned surfaces (e.g., 4 × 4 arrays) exhibit nonuniform evaporation rates due to the locally nonuniform water vapor concentration formed during evaporation, known as the shielding effect. We further demonstrated that this shielding effect can be mitigated by increasing droplet spacing and that evaporation rates are highly dependent on environmental humidity. As the shielding effect slows evaporation and promotes a stable culture environment, a detailed understanding of volume evolution over time for individual droplets within an array under the shielding effect is necessary.

To extend the phase-field approach for modeling real evaporation processes under combined humidity and temperature influences, we adopted an empirically determined equation. Besides the numerical model, we proposed a theoretical model to describe the shape of a droplet on a noncircular pattern, establishing a functional relationship between droplet volume and height, thereby simplifying volume determination in experiments. This theoretical model can be easily adapted to other topography-based wetting morphologies.

To evaluate the impact of evaporation on droplet composition during common laboratory procedures, we developed a real-time method to monitor changes in pH and solute concentration. Using DMEM culture medium as a proof of concept, we observed that volume reduction during assays significantly alters pH and solute concentration. These changes can affect cell culture growth, stability, differentiation, and drug delivery, which are critical in drug

screening assays. Although our method was tested specifically on DMEM culture medium, it has potential applications for other compounds and chemical reactions, offering broad utility for high-throughput miniaturized assays on DMA. Further research is needed to address challenges such as the effects of pH levels on droplet physical properties and the impact of solute concentration on product formation in miniaturized synthesis reactions. Our study underscores the potential of creating a digital twin system for miniaturized and parallelized applications requiring real-time control of droplet behavior.

2.2. Highly Parallel Nanoliter-Scale Liquid, and Spheroid Manipulation on Droplet Microarray via Sandwiching Method

Disclaimer: This chapter, associated sections and images are published in [§2] and have been adopted for this thesis.

[§2] **Urrutia Gomez JE**, Zhou M, Mandsberg NK, Serna JA, Von Padberg J, Liu S, Reischl M, Levkin PA, and Popova AA. Highly parallel and High-Throughput Nanoliter-Scale Liquid, Cell, and Spheroid Manipulation on Droplet Microarray. Adv. Funct. Mater. 2024, 35, 2410355. https://doi.org/10.1002/adfm.202410355.

The author contributions were as follows: Urrutia Gomez JE and Zhou M proposed the original idea, performed the experiments, curated, analyzed the data, and wrote the paper. Mandsberg NK curated, analyzed data and corrected the manuscript. Serna J. corrected the manuscript. Liu S and Von Padberg J printed the sandwiching adaptors. Reischl M. acquired funding and corrected the manuscript. Levkin PA and Popova AA proposed the original idea, acquired funding and corrected the manuscript.

Some of the content has been rewritten for a better understanding of this thesis work.

2.2.1. Introduction

2.2.1.1. Challenges and Opportunities in the DMA Implementation for a Large Spectrum of Biological Analyses

As mentioned in *section 1.3*, the DMA has been implemented for various types of biological and chemical analyses, demonstrating a high capability in interacting with different types of

analytical devices. Additionally, the DMA format is ideal for innovating new protocols and strategies for integration into established assays as well as developing new methodologies.

However, despite this versatility, numerous tasks that could potentially be implemented on the DMA remain unachievable due to challenges such as droplet evaporation, incompatible format, or the difficulty of handling hundreds of droplets simultaneously. As described in *section 1.3.5*, the methods that have not yet been adapted to the DMA typically involve non-optical analysis of samples. They also include procedures that rely on the conservation and manipulation of specific liquid volumes from a primary liquid source, such as media exchange, manipulation of cells, or non-destructive sampling. When scaled down to nanoliter droplets, these tasks become nearly impossible to perform. Nevertheless, if successfully implemented, they offer significant opportunities for parallelized and miniaturized research.

2.2.1.2. Motivation and Aim

In this chapter, we develop and validate a strategy for highly parallel nanoliter-scale manipulation of droplets on the DMA. Our goal is to create a user-friendly tool adaptable to a wide range of biological and chemical assays. We employ a technique called sandwiching, which leverages the open format of the DMA to create a sandwich structure by placing a glass counterpart of the DMA on top of the droplets. This configuration ensures uniform interaction of all droplets with the opposing surface simultaneously (Fig. 14b). The surfaces can range from a bare glass slide to another DMA slide, allowing for precise, rapid, and simultaneous manipulation of thousands of nanoliter droplets. These advancements are intended to broaden the scope of high-throughput, miniaturized studies in DMA, facilitating applications in drug screening, developmental biology, and advanced microtissue engineering.

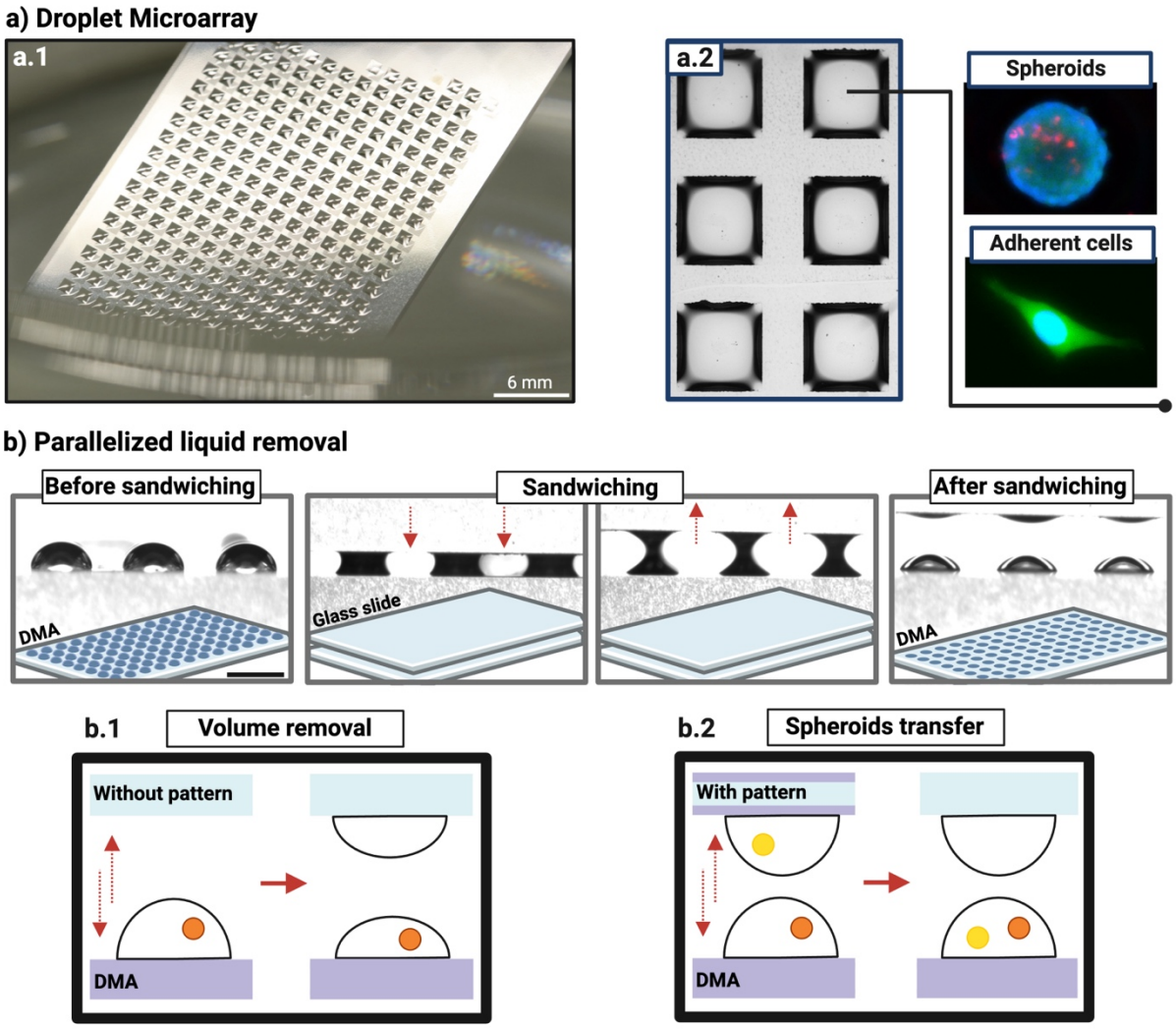

Figure 14. Droplet Microarray and sandwiching strategy. (a.1) Image of the Droplet Microarray submerged in water showing the simultaneous formation of nanoliter droplets due to its hydrophilic spots on a superhydrophobic background. (a.2) Microscopy image featuring 6 spots: showcasing superhydrophobic borders and hydrophilic spots within the DMA. Next to it a microscopy images capturing diverse cell culture models on DMA substrate. (b) Schematic depicting the assembly of the sandwich-like structure using a DMA. The procedure is illustrated from left to right. (Before sandwiching) The initial inset shows a side view of the DMA containing 300 nL droplets, alongside an illustration showing how the 672 droplets are positioned. This slide is hereafter referred to as the donor slide. (Sandwiching) The insets show the DMA sandwiched by a counter slide, which is referred to as the acceptor slide. Positioned 0.4 mm above the base of the droplets using an adapter the acceptor slide comes in contact with droplets formed on a donor slide at the highest point of the air-liquid interface, forming a new liquid-solid interface at the droplet's apex. Upon the removal of the acceptor slide, which breaks the capillary adhesion, the droplets undergo elongation. This is followed by the overcoming of pull-off forces, [97] resulting in a rearrangement of volumes. (After sandwiching) Side view image of the DMA post-sandwiching, showing a reduction in droplet's volume. (b. 1 and 2) Schematic representation of the different applications that can be carried out using the sandwiching technique. Volume removal allows to remove a portion of the droplet volume using homogeneous surface as an acceptor slide. Spheroids transfer permits the use of a hydrophilic-superhydrophobic patterned DMA slide as a donor and acceptor slide to transfer spheroids from one DMA to another by gravity. Adapted from Gomez et al. [§2]

2.2.2. The Sandwiching Method

The sandwiching method involves aligning two slides and placing them as close as possible, allowing the droplets pinned to one slide to interact with the surface of the other slide, causing

them to come in contact to the upper slide's surface. This method can also be used to merge or interact two distinct droplets, one on the bottom slide and the other on the top slide, creating a mother droplet from the two droplets by controlled merging. Additionally, when the top slide is removed from the sandwich format, it takes part of the droplet with it, leaving the other part on the bottom slide. This allows for a controlled removal of volumes from the droplets in a highly parallel manner.

Earlier research has utilized various methods to hold two glass slides together, ranging from manually operated custom-built metal frames [98] to automated systems that offer increased precision and stability. [65] Despite their accuracy, both the automated system and the metal frame published previously were cumbersome and not well-suited for routine operations. Additionally, in both instances, the approach was limited to transferring anticancer compounds by rehydrating dried substances from one slide to the other. In this study, we enhance the method by focusing on the simultaneous uptake of droplets and the transfer of their contents, broadening its use to regular on-chip lab procedures, particularly in cell culture manipulation. To simplify the process and improve alignment precision and consistency, we created a 3D-printed adaptor with a spacer that ensures the required distance between the DMAs, based on the spacer's height (Fig. 15). This adaptor was produced using maskless projection stereolithography via a DLP 3D printer, and its open-window design enables easy observation during droplet handling. (Fig. 17a).

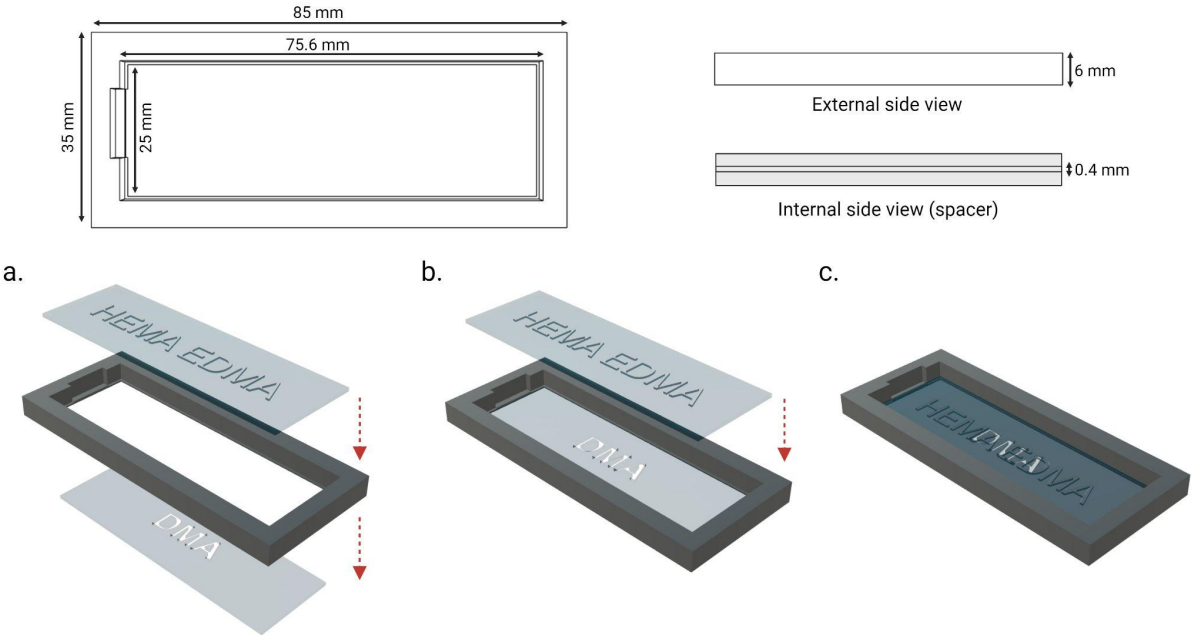

Figure 15. Rendering of DMA sandwiching adapter. The illustrations show the dimensions of the alignment frame as well as the dimensions of the internal spacer. (a.b.c) The process is illustrated from left to right, demonstrating

the assembly of slides in the adapter. The DMA is placed in the bottom part with the droplets facing inward into the adapter. The HEMA-EDMA slide is positioned in the upper part with its coated side facing towards the DMA. A 0.4 mm spacer is used to prevent both faces from touching, thereby avoiding the merging of droplets between neighboring ones. Adapted from Gomez et al. [§2]

Using the specially designed sandwiching adaptor, we first explored the process of droplet splitting on a DMA surface, with a poly (2-hydroxyethyl methacrylate-co-ethylene dimethacrylate) (HEMA-EDMA) coated slide serving as the acceptor. This polymer was selected for its high wettability (static water contact angle close to 0°), making it well-suited for droplet adhesion (Fig. 16a). When a droplet is sandwiched between two flat surfaces, a cylindrical liquid bridge forms. As the surfaces are separated, the capillary bridge undergoes Rayleigh instability, which leads to its division. Rayleigh instability describes the tendency of a cylindrical liquid column to break into smaller droplets due to surface tension aiming to minimize surface energy. This results in the formation of one droplet on each of the donor and acceptor slides (Fig. 16b).

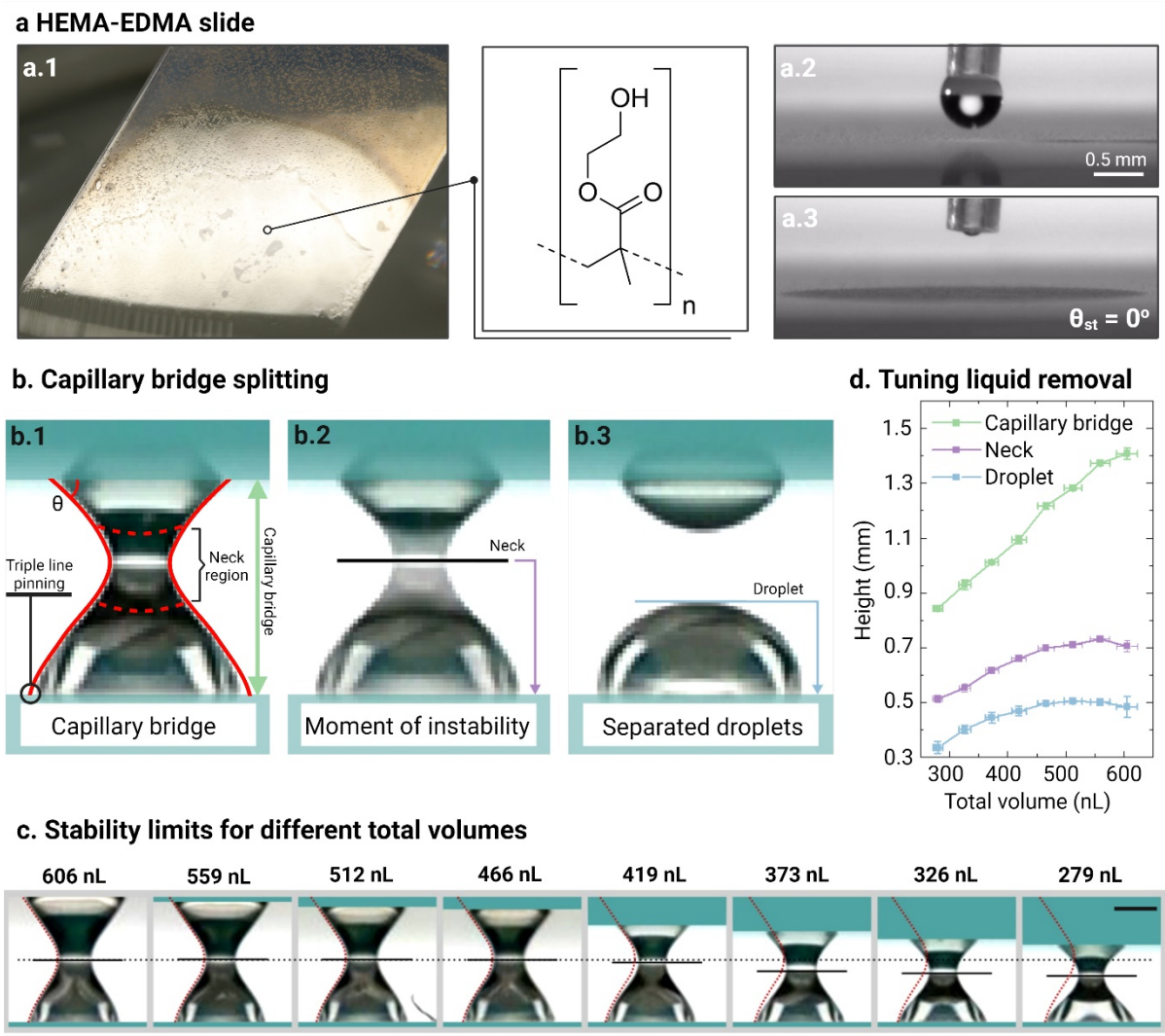

Figure 16. Analysis of volume extraction via capillary bridge instability between a DMA slide and a HEMA-EDMA polymer-coated surface. (**a.1**) Image of the slide coated with poly (2-hydroxyethyl methacrylate-co-ethylene dimethacrylate) (HEMA-EDMA) submerged in water showing its hydrophilicity. (**a.2-3**) Snapshot of the deposition of a droplet on the HEMA-EDMA slide showing a static water contact angle (θst) of 0°. (**b**) Sandwich wettability boundary conditions and capillary bridge (**b.1**) before, (**b.2**) during, and (**b.3**) after its division into two droplets. (**c**) Photos of capillary bridges of different volumes immediately before instability. Scale bar 0.5 mm. (**d**) Capillary bridge, neck, and resulting droplet height as a function of total capillary bridge volume (n = 4). Adapted from Gomez et al. [§2]

At the initial stage, when droplets on the donor DMA slide contact the acceptor slide, they create r–θ-type capillary bridges. [99] On the donor side, the bridge has a pinned triple line, while on the acceptor slide, a fixed apparent contact angle is maintained (Fig. 16b.1). [100] The pinning effect arises from the DMA's distinct wettability pattern, which anchors the triple line at the edge of the hydrophilic area, where the advancing contact angle reaches 168°, and the receding angle is less than 5°.

When a droplet successfully splits, the sizes of the resulting droplets are determined by the position of the neck, which is the inflection point of the capillary bridge. This position is

influenced by factors such as the total volume, the wettability of both substrates [101], the alignment of the substrates, and the speed at which they are separated. [102] The shape of these capillary bridges is primarily controlled by surface tension, rather than gravity. This is indicated by the Bond number, which in this case is about 0.03, showing that surface tension dominates. [103] Estimating the volumes after splitting is challenging due to the square footprint of the hydrophilic spots, which affects the shape of the cylindrical bridges. To address this, we experimentally established a relationship between the necking point and the initial droplet volume (ranging from 279 nL to 606 nL). Figure 16c depicts the capillary bridges right before the droplet splits, at the point of instability, while Figure 16d shows the length of the bridge, the necking point, and the final height of the bottom (donor) droplet after splitting, all as a function of the initial droplet volume.

Our data reveal two distinct behaviors in droplet splitting. For initial volumes between 279 nL and 419 nL, the height of the remaining droplet on the DMA increases with the initial volume. However, for larger initial volumes between 466 nL and 606 nL, the height of the remaining droplet becomes constant and no longer depends on the initial volume (Fig. 16d). The neck height exhibits a similar plateau, while the length of the capillary bridge continues to increase linearly across the entire range of volumes ($R^2 > 0.99$). These two behaviors arise from a decoupling between the neck region and the boundary conditions set by the acceptor slide. This is particularly evident when comparing the profiles of the capillary bridges (Fig. 16c, with the red dashed line representing the 606 nL profile overlayed on all images). Larger volumes result in nearly identical profiles, with the only difference being where the bridge is truncated by the acceptor slide. In contrast, for smaller volumes, the truncation occurs closer to the neck, causing the constraints from the acceptor slide to affect the capillary bridge shape and push the necking point closer to the donor slide, reducing the final droplet size. It's important to note that the independence seen at larger volumes may diminish as the volume increases further, allowing gravity to influence the bridge shape and potentially increase the height of the remaining droplet.

In summary, while it is possible to control the volume fraction by adjusting the initial droplet volume, the relationship is highly non-linear.

2.2.3. Application of the Sandwiching Method in Cellular Biology

2.2.3.1. Parallel Medium Replenishment Enables Long-Term Cell Culture On-Chip

Cell culture on the DMA platform has been limited to a maximum of three days without refreshing the cell medium on the spots. Beyond this limit, there is a significant decline in cell viability, with up to a 40% decrease by the fourth day. [58] The primary reason for this limited culture time is the challenge of rapidly and simultaneously removing cell medium from 672 individual nanoliter droplets while avoiding sample evaporation and cross-contamination. To address this problem, we used the sandwiching method to remove the cell medium from the droplets in parallel and then replaced it with new medium using liquid printers. Exchanging the medium of suspension cell cultures and 3D spheroids is challenging, even in plates, due to their non-adherent nature. These cells can be easily washed away and lost during the medium exchange procedure. Therefore, it was crucial to ensure that the sandwiching method did not displace or wash away the suspension cells from the droplets.

As shown in Figure 17, the sandwiching of two DMAs is clearly visible under the microscope, which is advantageous for imaging. This setup reveals a round spot shape (Fig. 17a.2) caused by the elongation of the droplets upon contact with the acceptor slide. Subsequently, we investigated whether this procedure had any physical impact on the cells, as shown in Figure 17b. When sandwiching was performed on the SU-DHL4 cell culture, it was observed that the cells remained unaffected both during and after the process. They were neither captured nor removed from the culture by the acceptor slide. A similar outcome was observed with HEK293 spheroids during sandwiching. Despite repeated contact between the donor and acceptor slides, the cells maintained their original morphology and remained unaffected, as confirmed by visual inspection under the microscope.

Following this evaluation, we proceeded with the medium replenishment strategy. This involved automated dispensing of 300 nL droplets containing cells in individual DMA spots, followed by cell incubation by the hanging drop method [46] for 24 to 48 hours. Once spheroids were formed, the sandwich method was used to remove 150 nL of spent medium, which was then replaced with fresh medium using a liquid printer. This procedure was applied every 4 days for a period of 14 days. As depicted in Figure 17c, there was a notable 17% increase in the diameter of spheroids subjected to medium refreshment, contrasting with the control group, which showed a 30% decrease in diameter. In addition, in Figure 17c.2, Hoechst and propidium

iodide (PI) staining revealed a significant difference in cell viability, with notably lower viability observed in the control group. This difference between the two groups confirms the effectiveness of the strategy in preserving both the integrity and morphology of the spheroids while allowing liquid manipulation.

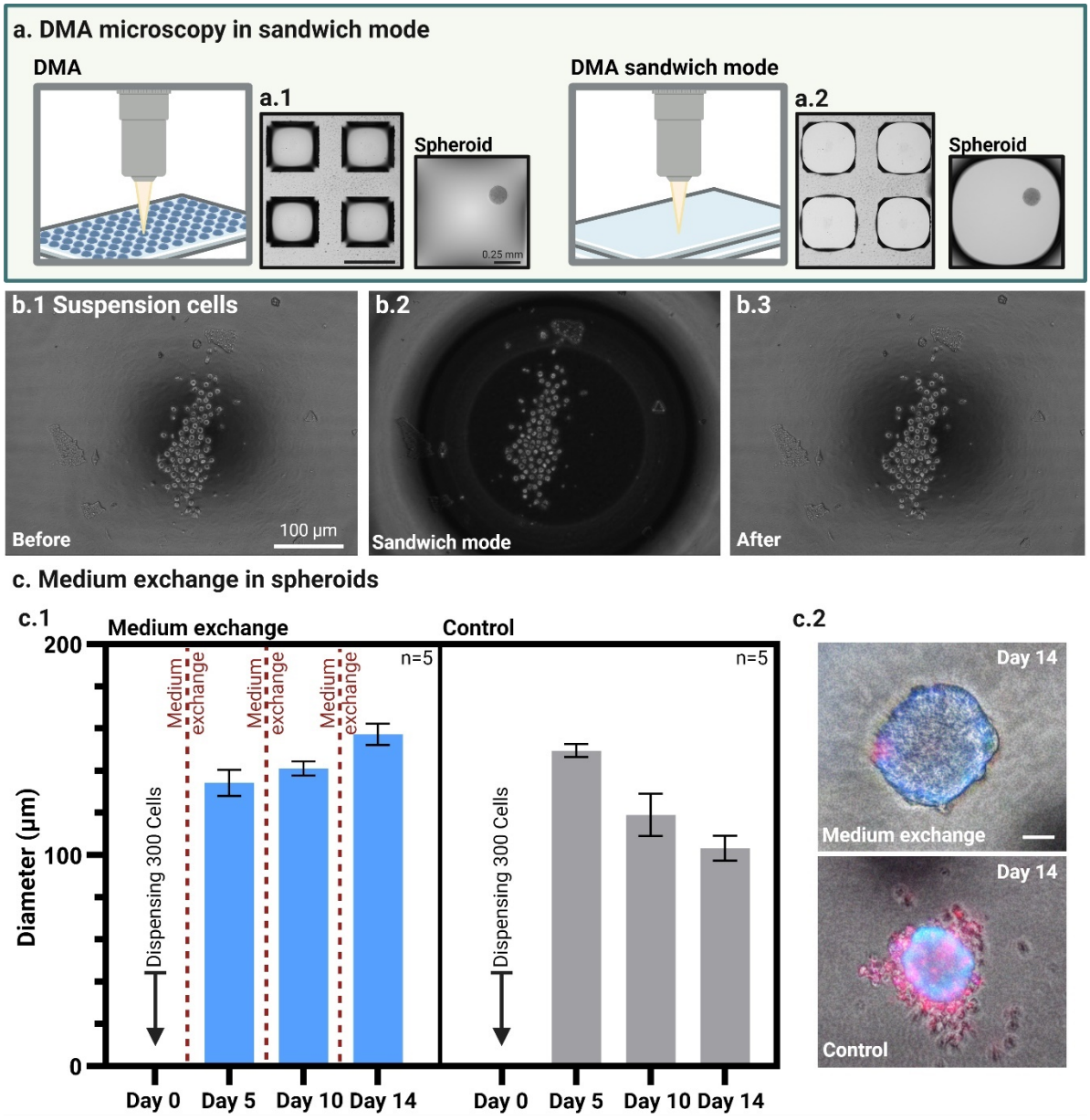

Figure 17. Extended cell culture of suspension cells (SU-DHL4) and HEK293 spheroids on DMA. (**a**) Diagram demonstrating the improved microscopy imaging when the DMA is in sandwiching mode. Scale bar 1 mm and 0.5 mm. (**a.1**) Optical microscopy image of a DMA slide featuring individual spots containing 300 nL of cell culture medium, alongside a spheroid from HEK293 cells. (**a.2**) Optical microscopy image of a DMA slide in sandwiching mode, displaying the previously mentioned spots, alongside the spheroid being sandwiched by the slides assessing any potential damage. (**b.1.2.3**) Sequential images depicting before, during, and after the application of the sandwiching technique on suspended cells, demonstrating that the cells are not perturbed by this procedure. (**c.1**) Plot of the spheroid diameter over time. Blue represents cultures receiving fresh medium every 4 days, while gray indicates cultures without fresh medium replenish for 14 days. (**c.2**) Images of stained spheroids on day 14. The upper image corresponds to a spheroid with addition of fresh medium every 4 days, while the bottom image corresponds to a spheroid without medium replenishment. Spheroids were stained with Calcein (Green), Hoechst (Blue) and PI (Red). Scale bar 40 µm. n=5. Adapted from Gomez et al. [§2]

2.2.3.2. Parallel Manipulation of Cells Spheroids

The manipulation of cell aggregates, such as spheroids, is of great interest in the fields of cell biology and tissue engineering. The ability to construct multicellular 3D structures enables studies of tissue morphogenesis [104] and the creation of advanced models of diseased tissues. [105] Current strategies to manipulate 3D cell aggregates mainly rely on aspiration systems that collect and transport the aggregates through gel-like or liquid media or on levitation and assembly using magnetic fields. [106] [107] However, these approaches are limited due to their reliance on complex instrumentation and low throughput. To overcome these limitations, we employed the sandwiching method to transfer spheroids from one DMA to another, by positioning one slide above the other, as shown in figure 18. This method relies on gravity to ensure the spheroids move from the top DMA to the bottom.

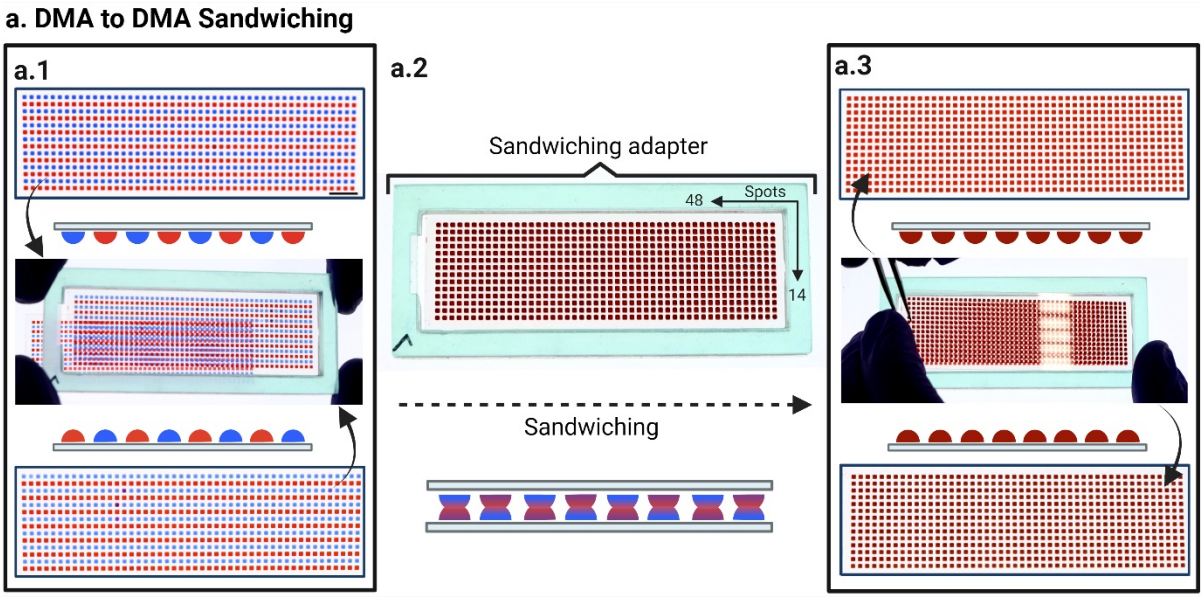

Figure 18. Parallel droplet merging process using the sandwiching technique between two DMAs. (**a**) The diagram illustrates the sandwiching method, using DMA slides with red and blue pencil ink droplets as a demonstration. (**a.1**) Snapshot shows two DMAs printed with blue and red ink droplets, illustrating how they are aligned and stacked using an adapter. Scale bar: 7 mm. (**a.2**) Another snapshot captures the moment the two DMAs are being sandwiched together. (**a.3**) A final snapshot displays the outcome of the sandwiching process, confirming that all droplets successfully merged with their respective counterparts without any cross-contamination between adjacent droplets. The image shows the top DMA being lifted off the other with tweezers. Adapted from Gomez et al. [§2]

To test the effectiveness of the sandwiching adaptor for mixing droplets between two DMAs, we printed each DMA with alternating parallel lines of 250 nL droplets of red and blue dye (Fig. 18a.1). The process began by placing one DMA on a flat surface. The sandwiching adaptor was then positioned on top, followed by the placement of a second DMA onto the adaptor to ensure precise alignment. Once the droplets merged, the top DMA was carefully

lifted off using tweezers, and the adaptor was then removed from the DMA on the surface. The results confirmed that all droplets from both DMAs merged and mixed successfully, with no fusion or cross-contamination between neighboring droplets on the DMA (Fig. 18a.3). The entire sandwiching and splitting process, involving two DMAs with 672 droplets each, took around one minute to complete.

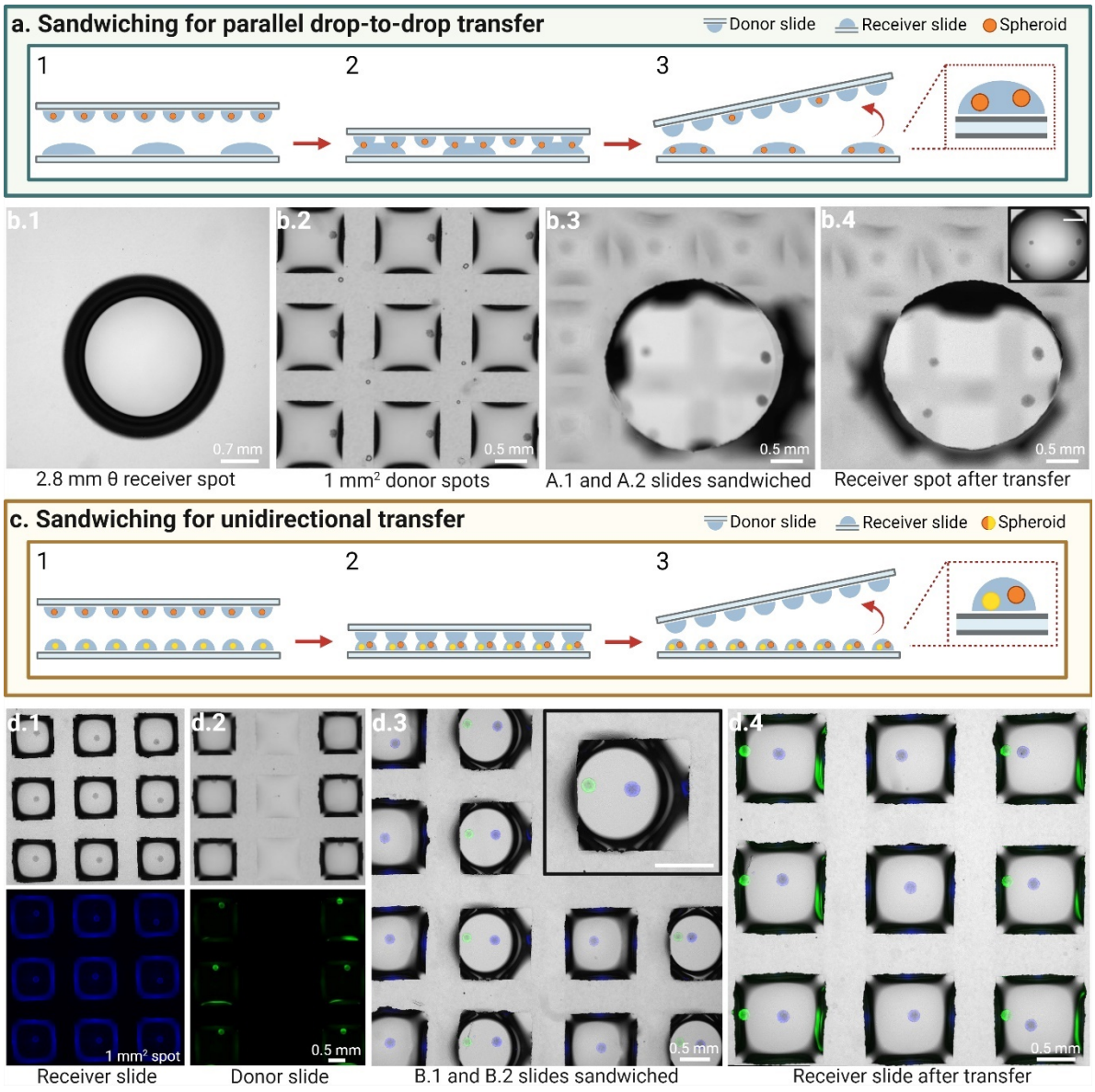

Figure 19. Sandwiching for parallel drop-to-drop transfer of cellular spheroids. (**a**) Step-by-step schematic representation of workflow of the transfer of an object from one DMA to another DMA through the utilization of the sandwiching method. (**b.1**) Spot with a diameter of 2.8 mm, containing 5 µL of culture medium. (**b.2**) 1 mm² spots containing 300 nL of culture medium and HEK293 spheroids. (**b.3**) Image of the target spot beneath the donor spots containing the spheroids. (**b.4**) Image depicting successful transfer of four spheroids from the donor slide to the receiver slide using the sandwiching method. The accompanying image in the upper right corner displays the target spot post-transfer. Scale bar 1.4 mm. (**c**) Schematic illustrating the step-by-step process of transferring multiple objects from one DMA to another DMA, which already contains an object, using the sandwiching method. (**d.1**) Image showing a 1 mm² DMA containing spheroids stained with Hoechst (blue) in 250 nL droplets. (**d.2**) Image showing a 1 mm² DMA containing spheroids stained with Calcein (green) placed alternately in 250 nL droplets. (**d.3**) Image of the receiver slide beneath the donor slide. The top right image shows

an enlarged image of a spot being sandwiched. Scale bar 0.5 mm (**d.4**) Final arrangement of spheroids achieved by the sandwiching method. Adapted from Gomez et al. [§2]

Using the sandwiching method, we smoothly transferred single spheroids from 1 mm² spots containing 300 nL of culture medium to a larger DMA format with 2.8 mm diameter spots and 5 µL of medium (Fig. 19b). Similarly, figure 19d illustrates the controlled pooling of spheroids between 1 mm² spot DMAs. The process begins with the receiver slide containing individual spheroids stained with Hoechst (blue) in 250 nL droplets (Fig. 19 b.1). Simultaneously, the donor slide also contains spheroids in 250 nL droplets, alternately located on the DMA and stained with Calcein for better tracking (green) (Fig. 19b.2). The transfer process proceeds by placing the donor slide on top of the receiver slide (Fig. 19b.3), allowing the controlled transfer of spheroids from one spot to another via gravity. The final result is a slide featuring spheroids with different stains sharing the same spot and arranged in alternating spots, demonstrating the process's controllability (Fig. 19b.4). This approach minimizes human error and significantly reduces transfer time. For instance, manually collecting a spheroid from droplets on a 1 mm² spot typically takes an experienced user about 45 seconds, with an additional 45 seconds needed for repositioning in another DMA. Scaling up, manually collecting 672 spheroids would require approximately 1 hour, whereas the sandwiching method accomplishes the task in only about 10 seconds. Unlike methods where spheroids from hanging droplets are transferred only once to cell culture dishes [108] or imaging plates, [108] our approach allows for multiple transfers.

2.2.3.3. Parallel Addition of Multiple Spheroids to Nanoliter Droplets

To replicate the complexity of natural tissues, artificial multicellular systems have been developed to imitate the spatial organization and geometry of various cell types within a 3D microenvironment. [109] These systems are often built using “building blocks” like cell sheets, [110] organoids, [111] and spheroids, [112] which are arranged into well-defined structures. However, many existing methods for creating these complex 3D cellular systems require advanced equipment and are not suitable for high-throughput production. Techniques such as directed and remote assembly, while effective, frequently involve manual steps or specialized tools, limiting scalability and potentially compromising cell viability. [113] [114] [115] [116] Additionally, methods using cell-laden hydrogels [117] or scaffold-based approaches [118] may suffer from low cell density or unintended interactions with the biomaterials used.

A recent strategy by Cui et al. utilized the open format of DMAs to control the merging of spheroids in neighboring droplets, creating multi-spheroid architectures with precise geometries. [119] Although this scaffold-free approach shows promise for automation, it is limited to spheroids from adjacent droplets on the same DMA, which reduces the total number of spheroids available for creating complex multi-spheroid structures. To enhance throughput in forming multi-spheroid architectures on DMAs, we adopted the sandwiching technique, which allows spheroids from additional, external DMAs to be incorporated into each droplet. This method enables the formation of thousands of droplets, each containing a customized number of spheroids that can subsequently fuse into intricate 3D cell assembloids.

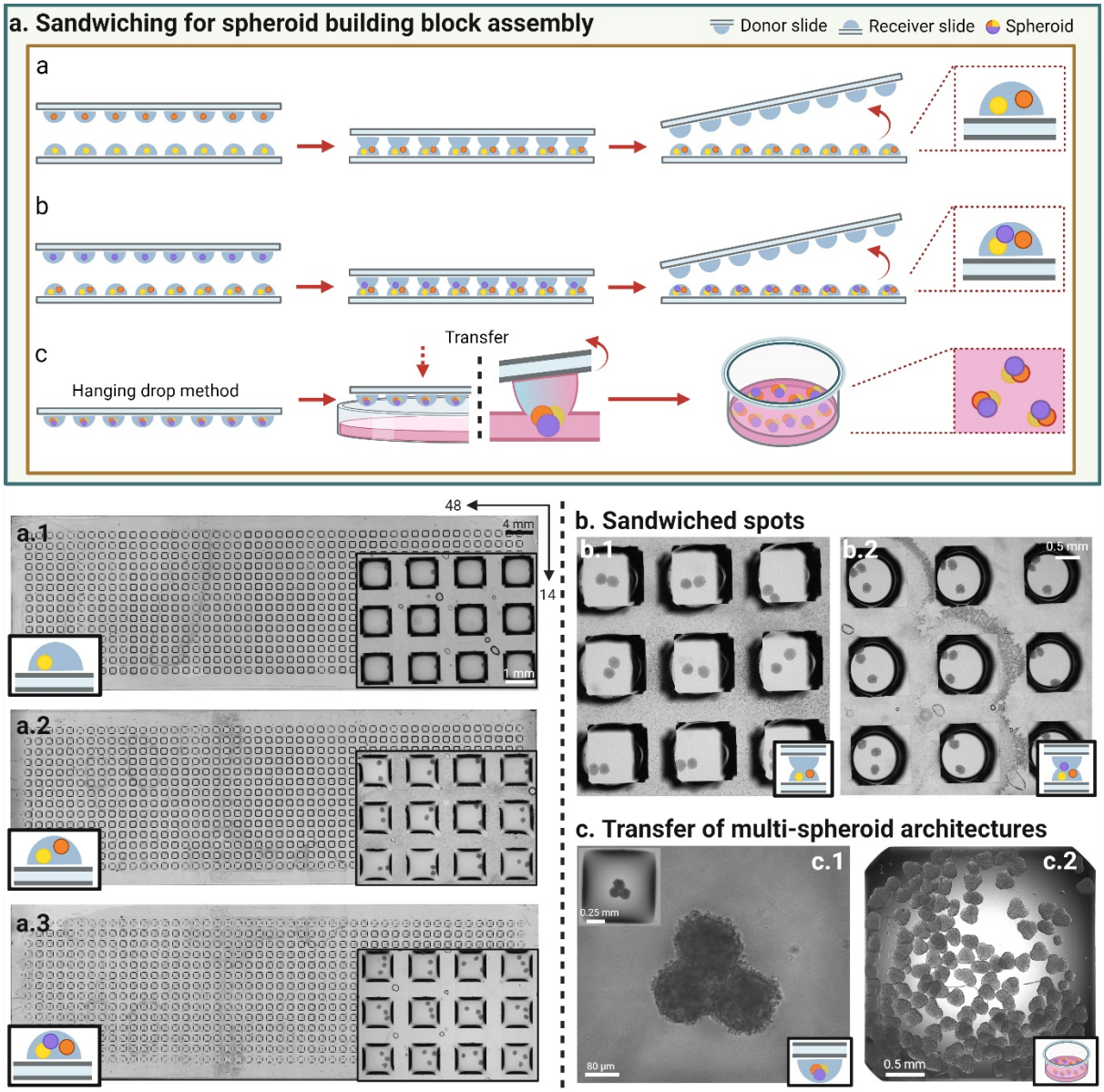

Figure 20. Sandwiching for formation and assembly of multi-spheroids cellular architectures. (**a-c**) Step-by-step schematic representation of the workflow of transferring spheroids from one DMA to another DMA using the sandwich method. (**a.1**) 672-spot DMA, each containing a single HEK293 spheroid; inset on the right shows a

magnified view of 12 spots. (**a.2**) DMA from image A1 after the transfer, now containing two HEK293 spheroids per spot; inset on the right shows a magnified view of 12 spots. (**a.3**) DMA from image A.1 after the second transfer of spheroids, showing three HEK293 spheroids per spot; inset on the right shows a magnified view of 12 spots. (**b.1 and 2)** Images obtained during the sandwiching of spots, showing how spheroids are transferred, resulting in spheroids pairs (**b1**) and triplets (**b2**). (**c.1**) Image showing a single spot containing three spheroids fused after 72 h. of incubation using the hanging drop method. (**c.2**) Image showing various multi-spheroid architectures collected from a DMA and transferred to a well of a 384-well plate. Adapted from Gomez et al. [§2]

To create these structures in each individual spot, we first generated HEK293 spheroids on three separate DMAs, each containing 672 droplets. As shown in Figure 20a we used a unidirectional transfer approach via the sandwiching technique to sequentially move spheroids onto a single DMA. This method initially produced spheroid pairs with a 95% success rate (Fig. 20a.2), followed by spheroid triplets with a 90% success rate (Fig. 20a.3). The DMA was then inverted, and the hanging drop method was applied for 72 hours to make the spheroids to merge into larger, more complex multicellular structures (Fig. 20c.1).

After the merging process was complete, the newly formed multi-spheroid architectures could either remain on the DMA for further studies, such as drug screening, or be transferred to other platforms for additional applications. To demonstrate the feasibility of harvesting these spheroid structures and to ensure they stayed intact, we transferred the triple spheroids from the DMA to a well plate. This was achieved by placing the DMA on the surface of a Petri dish containing cell medium, allowing gravity to assist in the seamless transfer of the multi-spheroids in a single step (Fig. 20c). Once settled, the supernatant was removed, and the spheroids were collected and relocated to a well plate using standard pipetting techniques (Fig. 20c.2).

The sandwiching technique for assembling spheroid structures also allows for the combination of different cell types, enabling the fusion of spheroids made from distinct cell types into unified, hetero-spheroidal structures. Furthermore, it supports the integration of both 2D and 3D cultures within a single spot, enhancing the flexibility of this method. This approach offers significant potential for modeling the complex cellular interactions and spatial organization found in native tissues, providing a versatile platform for developing multi-spheroid systems

2.2.4. Summary and Conclusion

In this chapter, we introduced a strategy for highly parallel manipulation of nanoliter-scale droplets using a sandwiching technique, which enhances biological assays by enabling on-chip parallel manipulation of spheroids. This technique involves placing a glass counterpart on top of the DMA to ensure uniform interaction of all droplets with the opposing surface.

The sandwiching method demonstrated significant success across various applications, such as medium replenishment for long-term cell culture on DMA. This approach effectively extended the culture duration of cell spheroids while maintaining high cell viability. Furthermore, it facilitated the smooth transfer of spheroids between different DMA configurations, enabling controlled transitions and pooling. The ability to precisely manipulate spheroids highlights the potential of DMA in constructing multi-spheroid architectures in a high-throughput manner. By combining and fusing spheroids into larger structures, these constructs can be utilized for both on-chip screening and subsequent collection for further analysis or tissue engineering. These innovations underscore DMA's adaptability to complex miniaturized assays, which were previously challenging or unfeasible.

Overall, the advancements discussed in this chapter present a novel approach to sample handling in DMA. The sandwiching method is straightforward, flexible, and easy to implement, offering new possibilities for experimental design.

2.3. ANDeS: An Automated Nanoliter Droplet Selection and Collection Device.

Disclaimer: This chapter associated sections and images are published in [§3] and have been adopted for this thesis.

[§3] **Urrutia Gómez JE**, El Khaled El Faraj R, Braun M, Levkin PA, and Popova AA. ANDeS: An automated nanoliter droplet selection and collection device. SLAS Technology. 2024, 100118. ISSN 2472-6303, https://doi.org/10.1016/j.slast.2023.11.002.

The author contributions were as follows: Urrutia Gomez JE proposed the original idea, wrote the code, built ANDeS, performed the experiments, curated, analyzed the data, and wrote the paper. El Khaled El Faraj R performed the qPCR experiments and corrected the manuscript. Braun M. contributed to writing the code and building ANDeS. Levkin PA and Popova AA proposed the original idea, acquired funding and corrected the manuscript.

Some of the content has been rewritten for a better understanding of this thesis work.

2.3.1. Introduction

2.3.1.1. Integrating DMA with Non-Optical Analytical Devices

As mentioned in *section 1.3.5*, integrating DMA with non-optical devices presents a significant challenge. This is due to its miniaturized format, which offers several advantages, such as reagent reduction, sample parallelization, and increased compartmentalization. However, these benefits can become disadvantages when it comes to individual or multiple sample collection and handling, as the format does not conform to common laboratory standards, making it incompatible with some preestablish workflows.

Additionally, issues such as volume loss and dead volumes when handling small quantities, or the evaporation and condensation of droplets, remain complex to control and address. As previously discussed in this work, there are significant advantages to applying the miniaturization and parallelization of DMA in areas that require non-optical equipment for final result reading. For instance, assays such as single-cell sequencing, single-cell proteomics or transcriptomics, and molecular profiling of low-input cells are of particular interest today, as they allow for a detailed assessment of cell heterogeneity within a population.

These assays require platforms like DMA, which can compartmentalize a discrete number of cells or even a single cell in an appropriate volume for precise sample preparation. This enables the cell to interact with reagents and allows the components to be studied at a dilution suitable for the small amount of molecules present. This type of assay is becoming increasingly popular in fields such as genomics, transcriptomics, and proteomics. However, most protocols rely on non-optical equipment, ranging from simpler devices like qPCR to more sophisticated ones such as LC-MS/MS. These devices require samples to be transferred into established workflows, typically using formats like tubes or well plates, or even loaded directly into the device, which limits compatibility with the DMA.

2.3.1.2. Motivation and Aim

In this chapter, we tackle the challenge of droplet retrieval on DMA by introducing the **A**utomated **N**anoliter **D**ropl**e**t **S**election and Collection device (ANDeS) (Fig. 22). This automated system is designed to aid in the collection and transfer of nanoliter droplets from the DMA to other platforms for subsequent analysis. The ANDeS integrates a 3-axis motion system with a syringe pump (Fig. 22a). By using the syringe pump, droplets are collected

through a fused silica capillary, which functions both as a nozzle and a sample container. This method allows for the sequential collection of multiple droplets within a single capillary, providing flexibility in adjusting the quantity and sorting of samples. Additionally, it facilitates the storage, transport, and transfer of samples to other platforms or measurement equipment (Fig. 21b and c). The ANDeS system ensures precise and reproducible collection of volumes ranging from 50 nL to 350 nL, with mechanical components that offer a positional accuracy of ±30 µm, enabling accurate positioning of the capillary tip to a DMA-spot area as small as 500 µm².

The results of this study aim to develop a method to improve the versatility of DMA, making it compatible with analytical devices that were previously incompatible with its format.

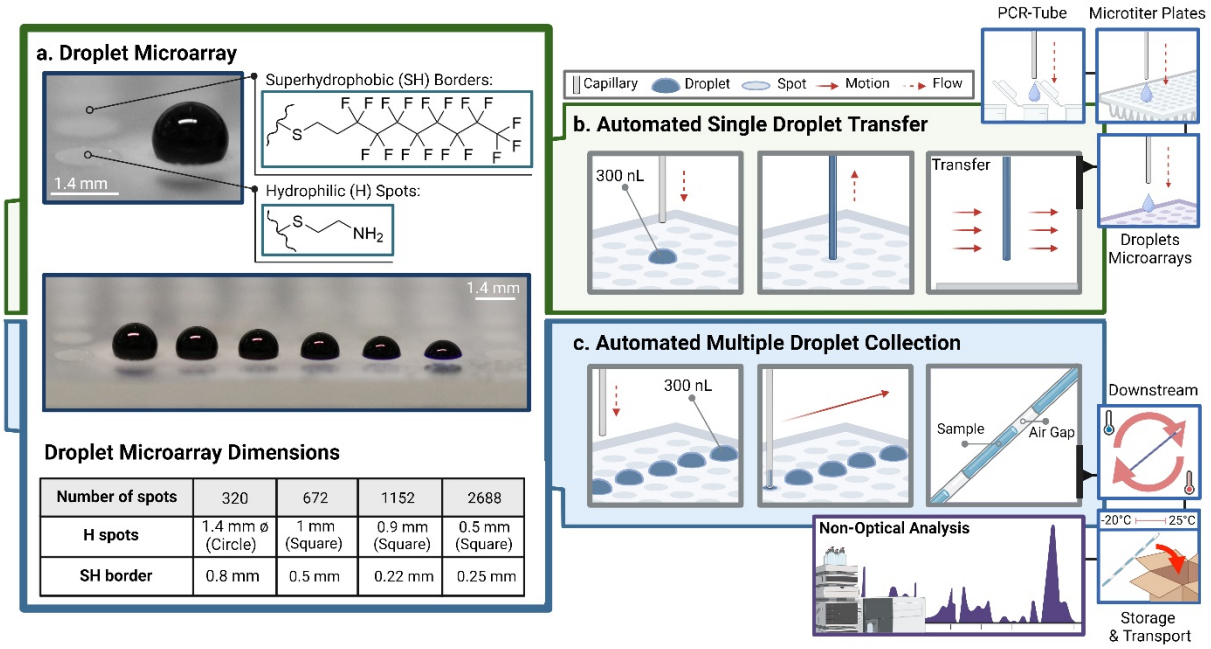

Figure 21. The concept of automated nanodroplet collection from Droplet Microarray. (a) A photo of a DMA slide showing droplets ranging from 2 µL to 500 nL. The accompanying table presents the dimensions of hydrophilic (H) spots, superhydrophobic (SH) borders, and the corresponding number of droplets per a 2.5 × 7.5 cm DMA slide. (b) Schematic workflow for single-drop transfer from a DMA to other platforms. (c) Schematic workflow for multiple droplet collection from a DMA, conducting in-capillary processing, storage of samples, and final analysis using non-optical analysis platforms. Adapted from Gomez et al. [§3]

2.3.2. Automated Nanoliter Droplet Selection and Collection Device (ANDeS)

2.3.2.1. Design and Construction

ANDeS is a 3-axis Cartesian motion system composed of linear rails, carriages, and transmissions. This system features an integrated syringe pump, a high-resolution camera for recording the process, and a touch-screen interface (Fig. 22a). The syringe pump is connected

to a fused silica capillary (75 µm inner diameter, 360 µm outer diameter) via fittings. The capillary serves as a replaceable nozzle and attaches to a Z-axis on a 3D printer hot-end extruder head to collect and relocate droplets (Fig. 22b). Nema 17 bipolar stepper motors drive the leadscrews on each axis and the syringe pump. These motors are synchronized by A4988 stepper controllers, which receive steps and direction signals from a Raspberry Pi 4 through the Reprap Arduino Mega Pololu Shield 1.4 (RAMPS 1.4). Additional components, such as the Raspberry Pi camera V2 and the touch screen display, are connected directly to the microcontroller for controlling and monitoring.

Positioning commands to place the capillary at the desired location within the workstation are determined using an open-access graphical user interface (GUI), designed for a 3-axis robotic positioning system. This GUI operates on an open-loop control algorithm, directing stepper motors according to a predefined sequence of movements and timing without real-time feedback from encoders or sensors. The code calculates the required step count based on the distance to the target and a predefined step-to-distance ratio. For example, with the 672 spots DMA array (48 by 14 spots with a 1.5 mm distance between spot centers), motor displacement is 37.5 steps between adjacent spots, with the upper-right spot serving as the home position. Users can input different array lengths and spot distances, which the GUI automatically translates into motion parameters.

Moreover, the system includes control over the motor driving the syringe pump, allowing users to set parameters for regulating the volume to be collected. The volume collected with ANDeS depends on the syringe volume, the flow rate controlled by the syringe pump, and the duration of liquid uptake. The flow rate can be adjusted by changing the revolutions per minute (RPM) and the number of motor steps via the GUI code. Users can specify different uptake durations for different spots, resulting in varied collected volumes within the same run. Additionally, the system allows for automatic loading of these instructions before each run to streamline the process.

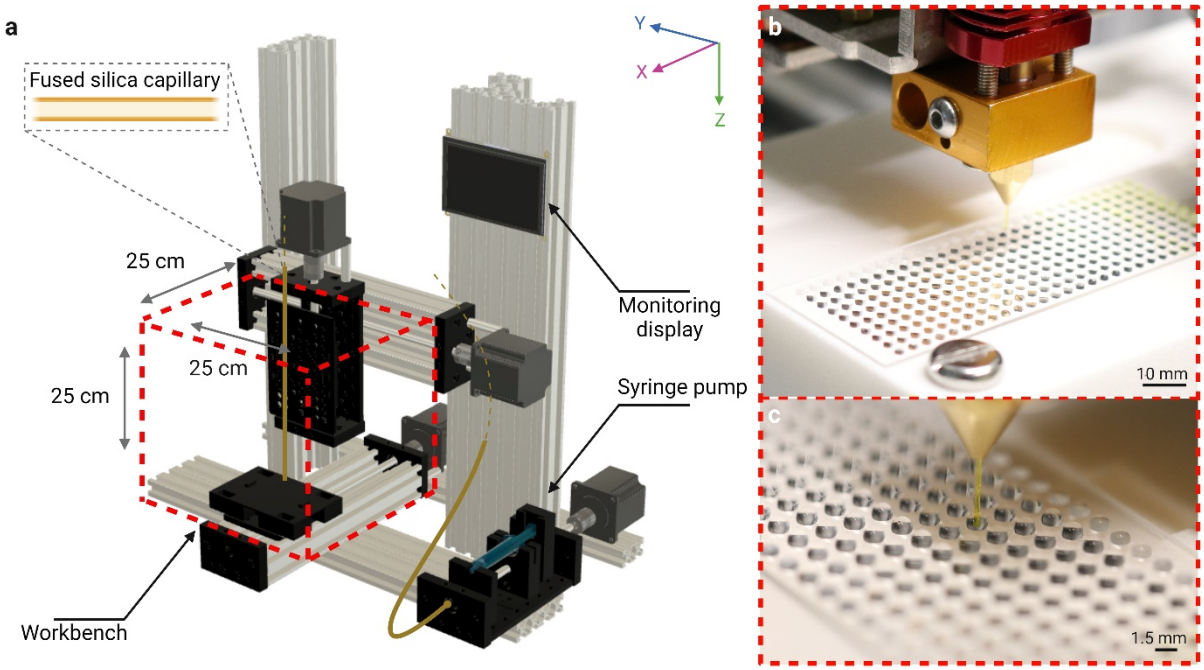

Figure 22. Depiction of the main characteristics of the ANDeS. (a) 3D renderings of the ANDeS based on a CAD model. The dashed box represents the workstation. (b, c) The workbench images display the capillary holder nozzle with a diameter of 360 µm Ø, as well as a DMA consisting of 320 spots with a round shape of 1.4 mm diameter. Each spot contains 1 µL of water droplets. Adapted from Gomez et al. [§3]

2.3.2.2. Characterization of Movement Accuracy

To validate the precision of capillary positioning within the hydrophilic spots, we utilized a DMA with square hydrophilic spots measuring 1000 µm on each side and a center-to-center distance of 1500 µm. We calculated the positional accuracy of ANDeS as illustrated in Figure 23.

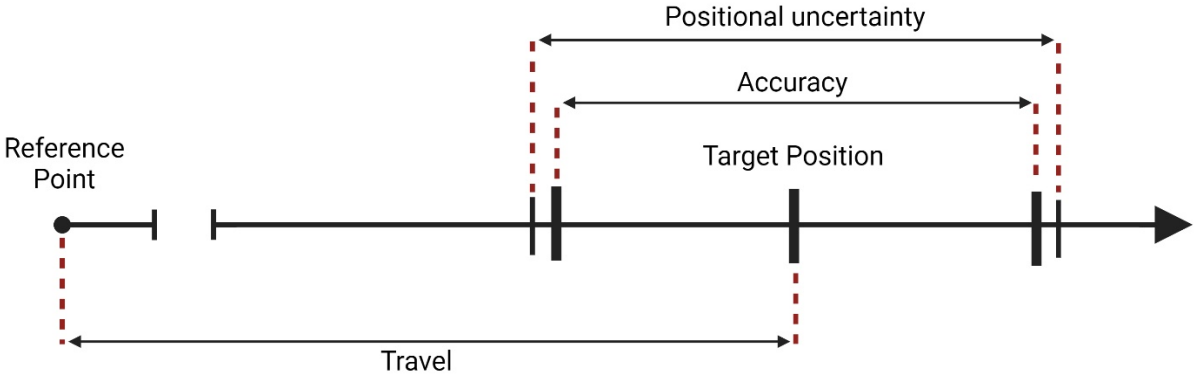

Figure 23. Characterization of positional accuracy of ANDeS. The schematic illustrates how the positional uncertainty and accuracy of ANDeS was estimated. To evaluate these parameters, each axis was moved in opposite directions over a given distance. Adapted from Gomez et al. [§3]

Accuracy refers to the ability of the axis to reach a given position precisely within the working area. For example, for the X-axis, this means it can be positioned with an error margin of up to ± 0.026 mm from the intended target. Conversely, positional uncertainty refers to the variability or imprecision in achieving those positions, meaning that when the X-axis is commanded to move to a specific location, it may deviate by up to ± 0.143 mm from the intended position (Table 3).

Axis	*X (mm)*	*Y (mm)*	*Z (mm)*
Travel	100	100	50
Accuracy	± 0.026	± 0.033	± 0.032
Positional uncertainty	± 0.143	± 0.156	± 0.127

Table 3. The table shows the values of travel, accuracy and positional uncertainty obtained for each axis. (n = 10)

To determine the values of accuracy and positional uncertainty for each axis, we measured their movement from the reference point to the target position in both directions at the system's maximum speed of 15 mm/second. This process was repeated 10 times. Once the data was collected, the standard deviations of the distances obtained were calculated to determine the positional uncertainty of each axis. The accuracy of each axis was then estimated by calculating the Mean Squared Error (MSE). Finally, the MSE values of all axes were averaged to determine the overall accuracy, resulting in a combined MSE of ± 30 µm. This level of precision allows for accurate control of the system, enabling precise positioning of the capillary nozzle on arrays of various sizes, including microtiter plates and the DMA with 2688 spots (H spots: 0.5 mm square; SH border: 0.25 mm) (Fig. 21a).

2.3.2.3. Characterization of Droplet Collection and Transfer

To control the collection flow to pick up droplets of different sizes within just one second, we first determined the dependencies of the collected volume on parameters such as flow rate and motor frequency. We mounted a 100 µL syringe on the syringe pump and maintained a constant motor frequency of 3000 RPM. By varying the number of steps executed by the motor, we observed the collection of different experimental volumes. Using a capillary with a length of 150 cm and a diameter of 75 µm, we conducted measurements with water droplets, repeating

the process three times for each of six different volumes ranging from 50 nL to 300 nL. The experimental data was then used to develop an empirical model describing the relationship between collected volume, flow rate, and motor steps (*num_steps*). This model followed a nonlinear regression equation, as shown in figure 24.

$$Flow = a \exp(b\ num\_steps) + c \qquad (2.11)$$

Compared to experimental data, the model demonstrated a coefficient of determination (R^2) of 0.9742 and a residual standard error ($Sy.x$) of 19.05, indicating it can estimate the flow rate for collecting a single droplet of the desired volume with an accuracy of ± 19 nL/s.

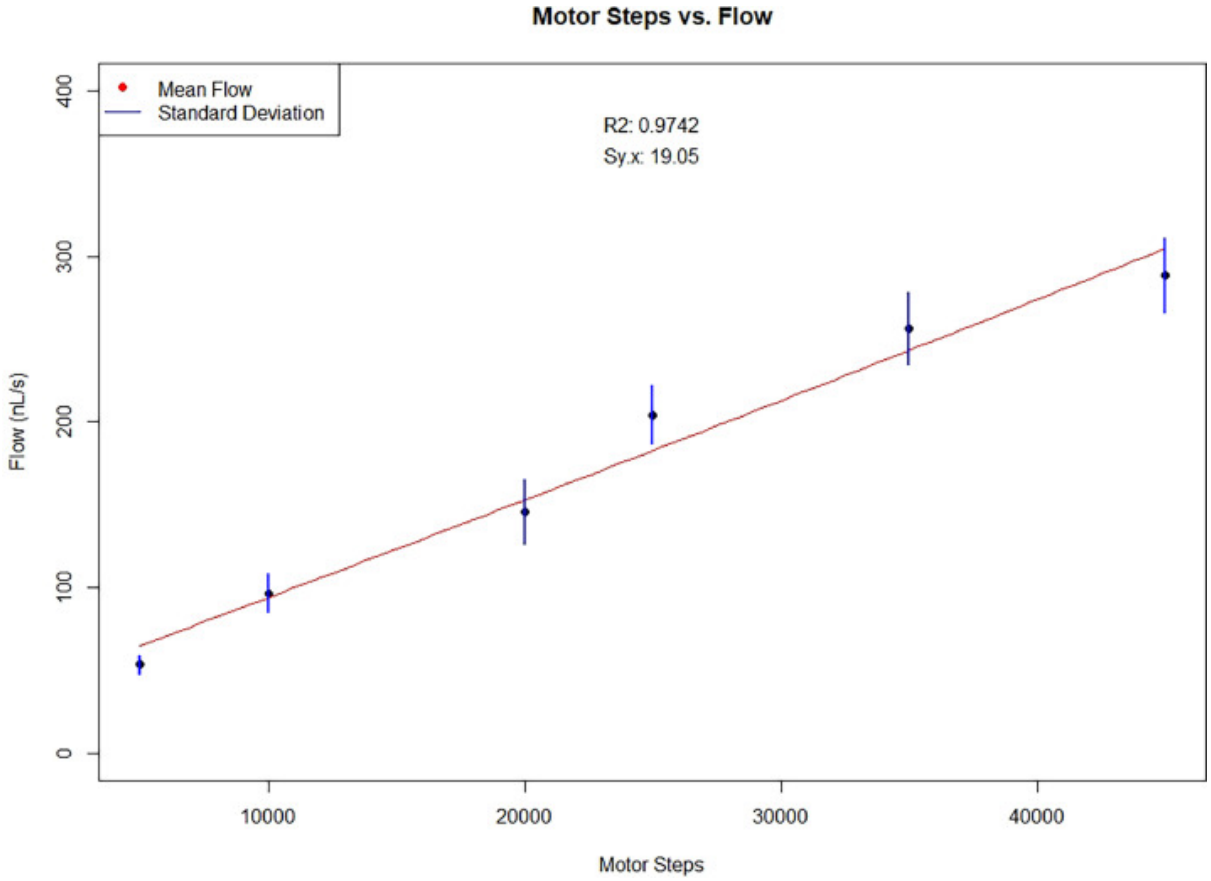

Figure 24. Empirical model describing the relationship between collected volume, flow rate and engine steps. Adapted from Gomez et al. [§3]

After establishing the droplet collection process, we validated the efficiency of ANDeS in transferring droplets from the DMA to other platforms, such as microtiter plates, vials, and other DMAs. This validation targeted applications related to the analysis of molecules collected or generated within the DMA. In such cases, transferring compounds from the DMA to other vessels is necessary for subsequent analysis by equipment such as PCR/qPCR machines, LC-MS, or NMR. To evaluate the transfer process, we manually pipetted 300 nL of water onto a

1.4 mm Ø DMA spot, which was then automatically collected by ANDeS via capillary and transferred to another spot (Fig. 25a).

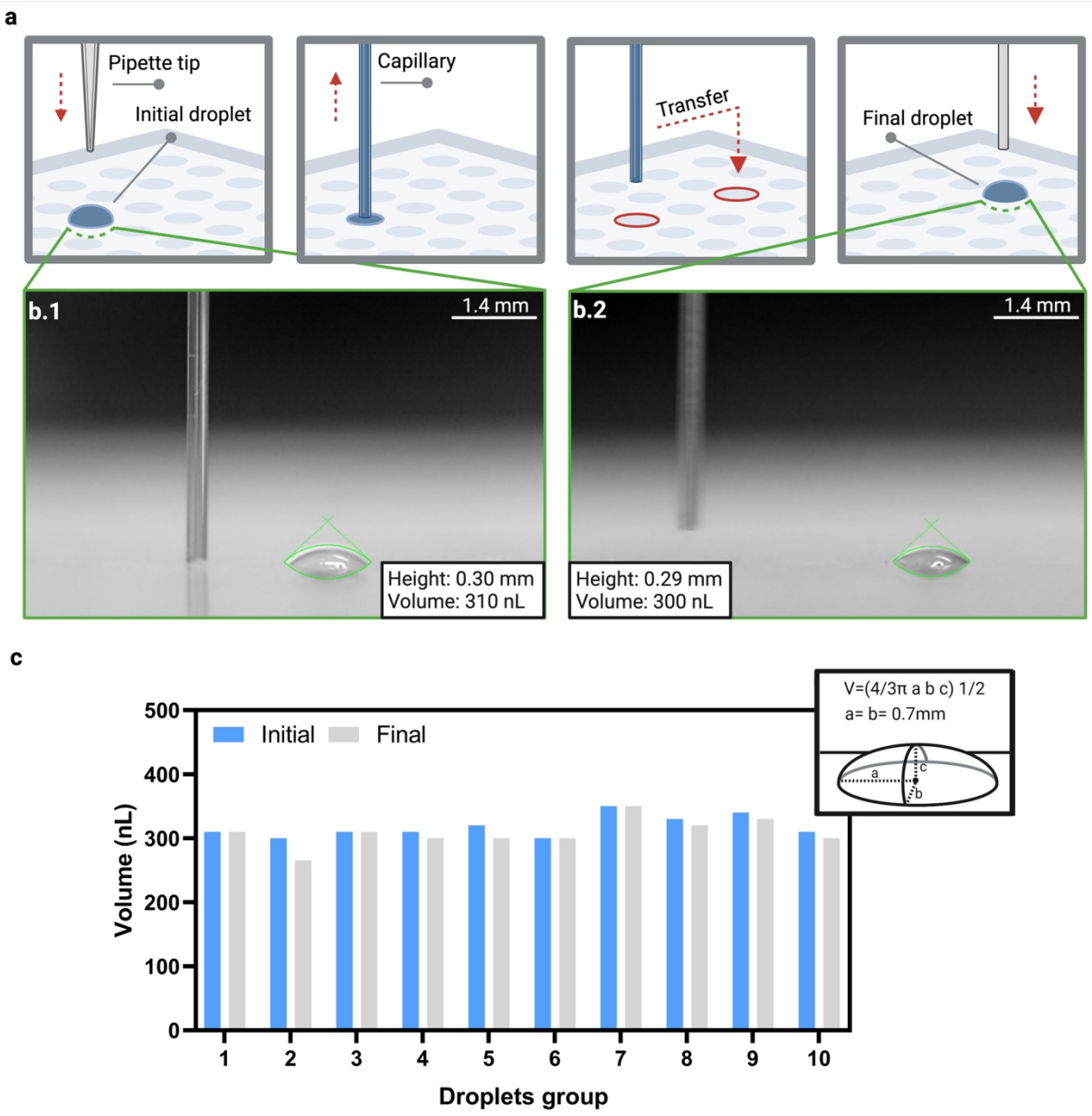

Figure 25. Assessment of accuracy of droplet transfer. (a) Schematic representation of step-by-step automatic collection and relocation of a 300 nL droplet. (b.1) Analysis of droplet height and volume prior (b.2) and after the transfer. (c) Comparison of the volumes of droplets prior and after the transfer (n = 10). Adapted from Gomez et al. [§3]

The height of the relocated droplet was measured and compared to its initial height before collection, as shown in Figure 25c. The volume of the droplets was calculated using the equation for the volume of a spherical cap, where a and b represent the radius of the hydrophilic spot (1.4 mm Ø) and c is the height of the droplet. The final calculated volumes of the transferred droplets averaged 308 nL with a 95% confidence interval (CI) of ±13 nL,

corresponding to a measurement error of 1.2% (n = 10). The results indicated that an average volume loss of 2.9% occurs when moving a droplet from one point to another.

After determining the volume loss associated with the droplet transfer process, further experiments showcased ANDeS's ability to transfer droplets between different platforms. For instance, the system successfully transferred 250 nL droplets from a 1 mm square hydrophilic spot to a 1.4 mm Ø spot, with each transfer taking approximately 30 seconds. Additionally, it was possible to transfer a 500 nL droplet from a 1.4 mm Ø hydrophilic spot to a 250 µL conical tube and back again. These demonstrations highlight how ANDeS can automate sample collection from the DMA and facilitate sample transfer, particularly for volumes that are challenging for manual collection. The capability to collect and transfer nanodroplets enables detailed sample analysis in the nanoliter range, eliminating the constraints imposed by manual collection methods.

2.3.2.4. Characterization of Multiple Droplet Collection

The utilization of fused silica capillaries for sample collection was chosen to fulfill specific requirements, such as accommodating multiple nanoliter samples, ease of handling, material durability, prevention of sample evaporation, and convenience in sample transport and storage. These capillaries offer versatility in length and diameter, allowing them to contain different volumes and amounts of samples according to user preference. Additionally, sample withdrawal from capillaries to other containers or platforms is straightforward and can be performed by ANDeS or manually using a syringe pump.

To validate the collection of multiple droplets, a DMA containing an array of 1 mm square hydrophilic spots was fully printed with 200 nL droplets using a non-contact liquid dispenser. Subsequently, six of these droplets were automatically collected by ANDeS using the same capillary. The lengths of the capillary the samples occupied (plugs) were then determined using a light microscope, as depicted in Figure 26a. To separate each sample from the previous one, an air plug of approximately 2.5 mm was created, determined by the time the capillary is suspended in the air without contact with the samples. The volume of the sample inside the capillary was calculated using the equation for the volume of a cylinder. Here, the internal radius was taken as the radius of the capillary (37.5 µm), and the length was measured as the length of the plug, which is the distance between the center points of the meniscus at both ends of the sample. (Fig. 26).

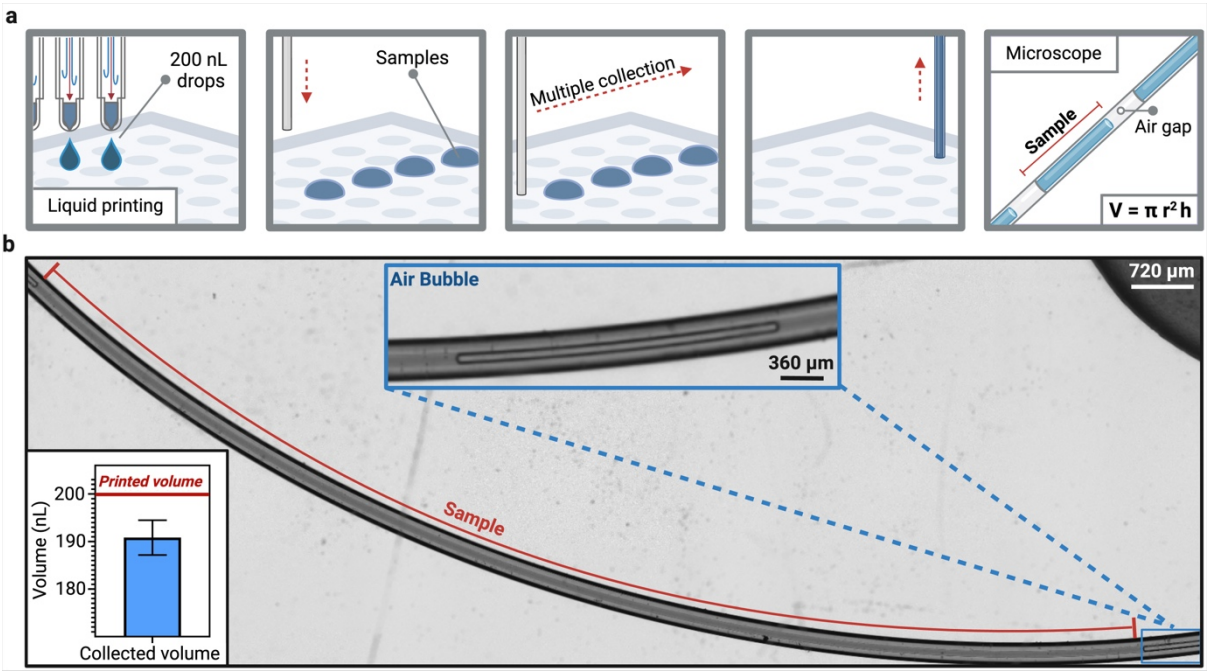

Figure 26. Characterization of the automatic multi droplet collection. (a) Schematic workflow of the automatic multi droplet collection. (b) Image of a sample and an air plug between the samples inside fused silica capillary. In the lower left corner, the graph showing the measured volumes of the droplets collected inside the capillary compared to the initially printed volume of 200 nL. The red line represents the volume printed by the non-contact liquid dispenser. Error bar shows the standard deviation between 6 replicates each. Adapted from Gomez et al. [§3]

As shown in Figure 26b, the volumes of collected droplets inside the capillary were calculated to average 190 nL, with a 95% confidence interval (CI) of ±2.6 nL, corresponding to a measurement error of 3% (n = 6). These results indicated that an average volume loss of 4.6% occurs when collecting multiple droplets from the DMA.

For a total collection of six droplets, the time required was approximately 1 second per drop and an additional 1 second waiting time between droplets to create the air plugs. Therefore, theoretically, by employing an adequate syringe volume and adjusting the number of motor steps to match the syringe gauge, it would be possible to collect all 300 nL droplets from a 672-spot DMA in about 22 minutes when operating at the maximum frequency.

The ability to collect several samples in a single capillary without mixing them offers the opportunity to perform in-capillary downstream processing. This can involve various techniques such as thermal shocks, sonication, or UV treatment. Additionally, this format allows for the consecutive injection of these samples directly into analytical workflows, such as a liquid chromatography system.

2.3.3. Demonstration of ANDeS for Real-Time Experimental Workflow

To demonstrate the use of ANDeS for real lab applications, we performed and validated the collection of cDNA samples from a DMA chip using the Cells-to-cDNA on Chip method. [62] In this method, the entire sample preparation process, including culturing and lysing cells, isolating mRNA, and converting it to cDNA, occurs in 200 nanoliter droplets. Although the protocol demonstrated high efficiency, the sample collection step had limitations. Manual collection of individual nanoliter droplets is not feasible, so droplets were pooled into a single conical PCR tube using a larger volume of liquid. This method requires skilled users, does not allow for addressing individual droplets, and is associated with a risk of sample loss and cross-contamination.

To address this problem, we sought to validate the automated collection of droplets containing cDNA and compare it to the manual procedure. For this, cDNA samples obtained in 350 nL droplets using the Cells-to-cDNA on Chip protocol were collected both manually and automatically (Fig. 27a and b). Each sample was then transferred to a single conical PCR tube for quantification of cDNA using qPCR analysis targeting the GAPDH (GlycerAldehyde 3-Phosphate DeHydrogenase) gene, as depicted in figure 27.

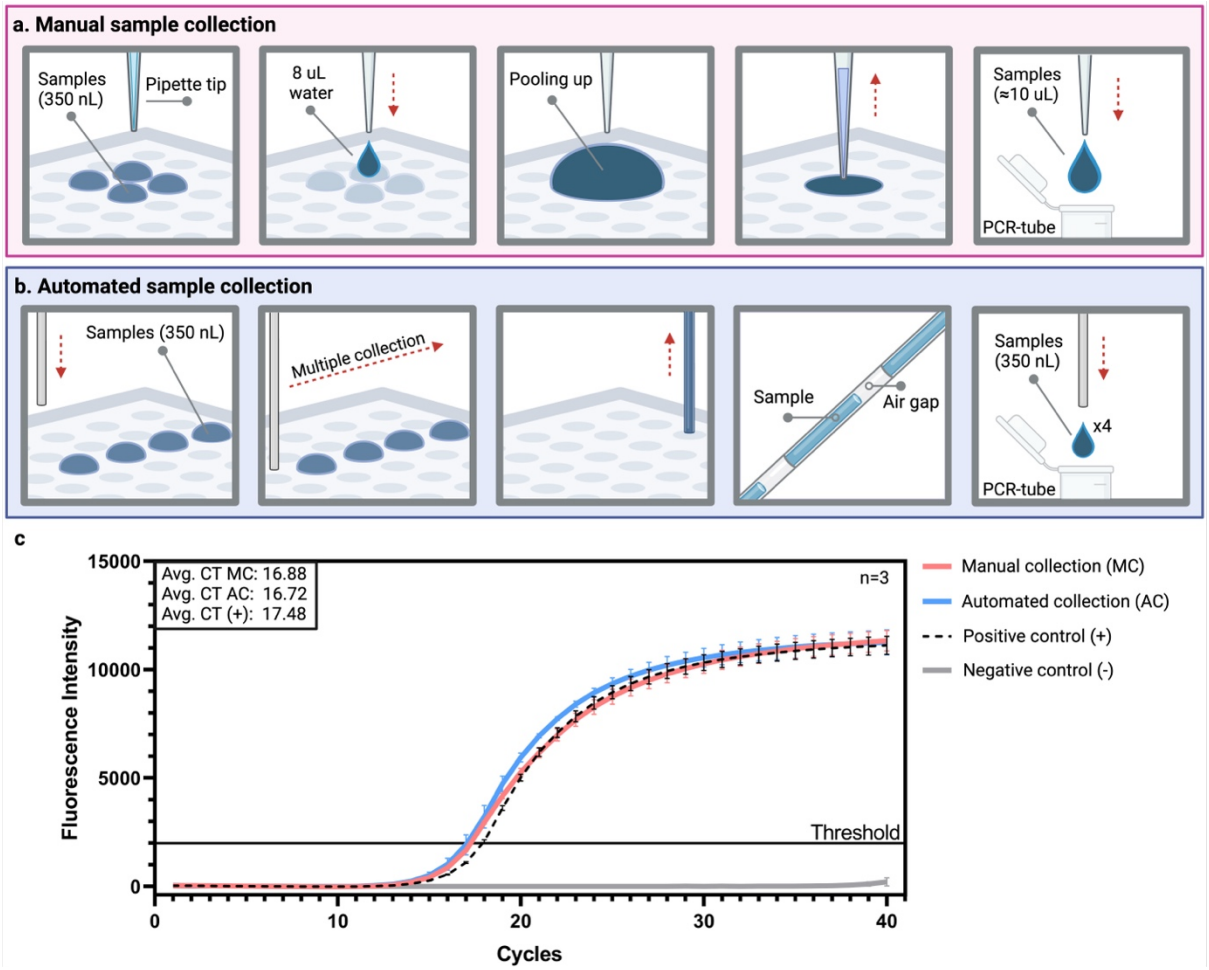

Figure 27. Quality comparison of samples collected automatically and manually. (a) Schematic of the protocol for manual collection of nanoliter samples from a DMA. (b) Schematic of the protocol for automated collection of nanoliter samples from a DMA. (c) qPCR amplification curves of manual and automated collection of 22.6 ng/µl of cDNA synthesized by the Cells-to-cDNA on Chip method from SU-DHL-4 cells. (Avg. CT MC = Average Cycle Threshold Manual Collection; Avg. CT AC = Average Cycle Threshold Automatic Collection). Error bars show the standard deviation between 3 replicates each. Adapted from Gomez et al. [§3]

The obtained results demonstrate that samples collected automatically using ANDeS exhibit average cycle threshold (*CT*) values for the GAPDH gene of 16.72, reflecting the concentration of cDNA in a sample (Fig. 27c). This is comparable to GAPDH *CT* values of 16.88 in samples obtained through manual collection. Both automatically and manually collected samples had GAPDH *CT* values close to those of the positive control (17.48), which was the original sample used for the test. These results indicate that the automated method for droplet collection is efficient and does not lead to DNA loss during the transfer steps.

Moreover, the automated method enables the collection of each of the 672 individual droplets, which is not possible with manual droplet pooling. Pooling multiple droplets for collection requires a labeling strategy to distinguish the content from the original droplets. ANDeS allows diverse samples to be collected and analyzed without the need for prior labeling. Additionally,

the automated collection process preserves sample integrity by avoiding sample dilution during pooling, reducing the risk of sample loss during collection. It also minimizes human error and reduces collection time. For instance, while an experienced laboratorian might take approximately 45 seconds to collect a group of 4 droplets manually, ANDeS can collect the same group in only 8 seconds. On a larger scale, manually collecting 200 droplets would take about 37 minutes, whereas the automated method would accomplish the task in just 6 minutes.

As a next step, we validated the multiple droplet collection (*MDC*) method using the same cDNA sample approach. Unlike the previous method, where droplets were collected individually and then pooled together in the same PCR tube, the *MDC* method collects all samples in the same capillary and analyzes each droplet independently. As shown in Figure 28, the *MDC* method was used to collect 350 nL droplets of both cDNA and water within the same capillary. The inclusion of water droplets in this experiment allowed us to assess the potential for cross-contamination between collected samples when using the *MDC*. After collection, samples were transferred to separate PCR tubes for subsequent qPCR analysis.

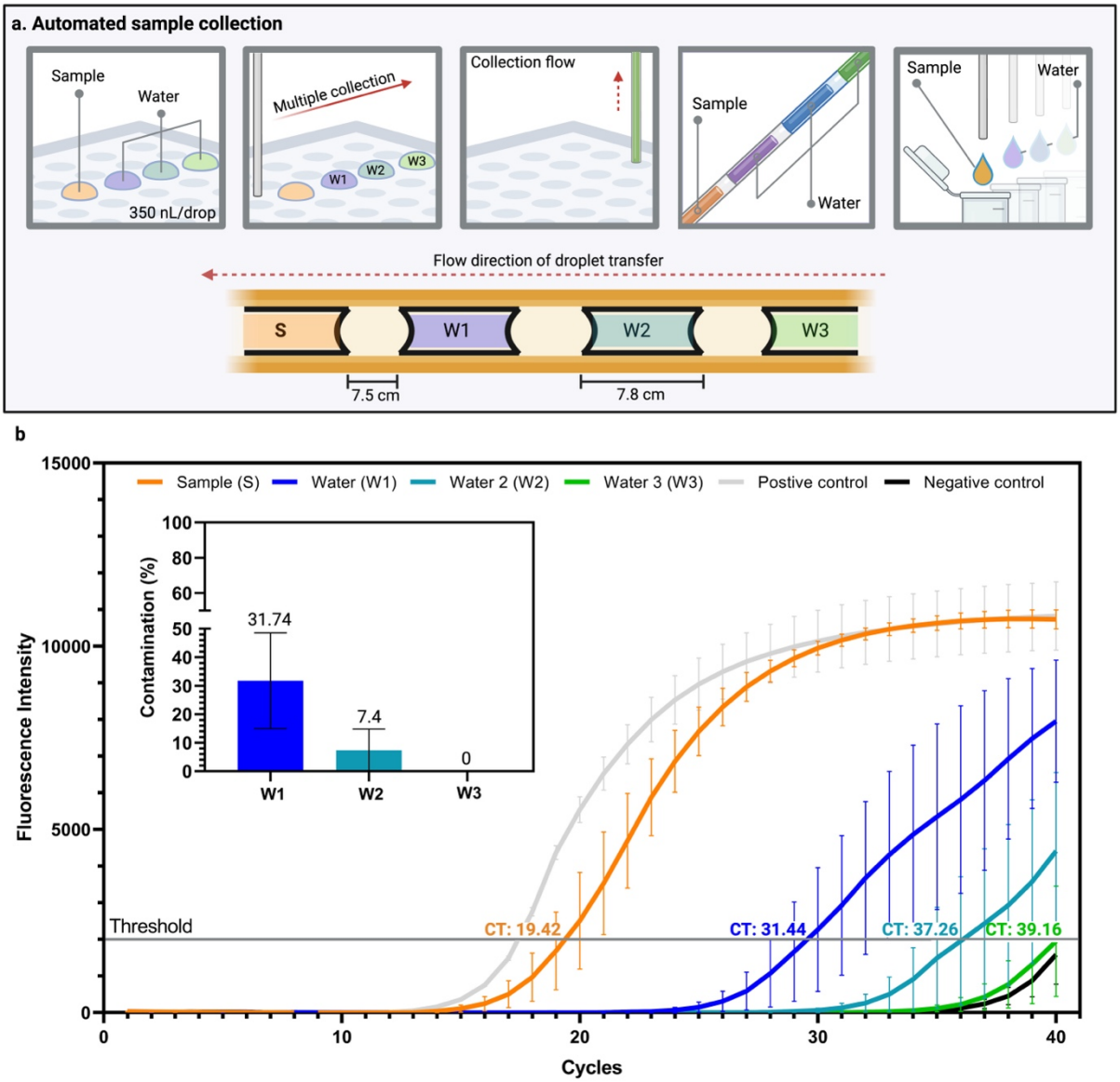

Figure 28. Assessment of qPCR amplification of 350 nL droplets. (a) Schematic of the protocol for automated collection of nanoliter samples of cDNA and water from a DMA and subsequent droplet assignment in PCR tubes. For droplet collection, a fused silica capillary of 75 µm inner diameter and 80 cm length was used. The collection rate was set at 1 second per droplet, with an additional 1 second standby to create air gaps between the droplets. The first drop collected was the drop containing a concentration of 22.6 ng/µl of cDNA, followed by the 3 drops of water. After the collection process, the capillaries were removed from the ANDeS and closed at the ends with a silicon septum. The capillaries were then reinserted into the ANDeS syringe pump so that the cDNA sample was located at the opposite end to the one inserted into the pump. Subsequently, the samples were deposited in different PCR tubes using the syringe pump in infusion mode. Throughout this process, the capillaries were monitored with a microscope to observe the advancement of the droplets and ensure their accurate deposition into the PCR tubes which contained the qPCR master mix. Finally, the samples were evaluated for GAPDH gene expression via qPCR analysis. (b) qPCR amplification curves of individual cDNA and water droplets collected within the same capillary. The accompanying graph shows the percentage of contamination in the water samples. Error bars show the standard deviation between 3 replicates each. Adapted from Gomez et al. [§3]

As shown in Figure 28b, samples obtained from single 350 nL cDNA droplets exhibited a mean *CT* value of 19.42, indicating successful amplification of the GAPDH target gene. The three water droplets introduced consecutively in the capillary showed mean *CT* values of 31.44, 37.26, and 39.16, respectively. According to qPCR diagnostic analysis standards, *CT* values

higher than 37 are considered a reasonable cut-off point to conclude the absence of the target gene in the sample. [120]

To assess cDNA contamination in the water droplets, we applied a conditional statement: if the mean *CT* value of a water droplet is less than or equal to the mean *CT* of the sample (19.42), the droplet is considered 100% contaminated. Conversely, if the mean *CT* value is greater than or equal to the cut-off value (37), the droplet is considered not contaminated. For droplets with *CT* values between these thresholds, the percentage of contamination is calculated proportionally.

Using this method, the following conclusions were made: the first water droplet, closest to the cDNA sample, exhibited a contamination percentage of 31.7%; the second droplet showed 7.4% contamination; and the third droplet demonstrated no apparent contamination (0%) (Fig. 28b). It is important to highlight that the qPCR technique has very high sensitivity, capable of detecting DNA in samples at very low concentrations, even down to 10 pg/µL [121] [122]. The results demonstrate a certain droplet-to-droplet contamination risk, which can be efficiently mitigated by adding two separate droplets of water between each sample droplet.

In this study, we utilized quantitative polymerase chain reaction (qPCR) to effectively characterize the transfer and cross-contamination of multiple droplets collected within a single capillary. The findings highlight the performance of ANDeS in accurately collecting multiple nanoliter droplets. Moreover, our results underscore the potential of conducting qPCR analysis on nanoliter samples obtained from DMA.

2.3.4. Summary and Conclusion

In this chapter, we developed and tested the Automated Nanoliter Droplet Sorting and Collection (ANDeS) device, designed to overcome the challenge of retrieving nanoliter droplets from Droplet Microarrays for subsequent transfer to analytical equipment or for relocating droplets within a DMA slide. ANDeS offers a positional accuracy of ±30 µm, enabling precise positioning of the capillary nozzle within a DMA slide down to 100 µm hydrophilic spots. This accuracy could be further improved by using leadscrews with a smaller pitch and incorporating microstepping technology.

ANDeS can also be adjusted to collect larger droplets by replacing the 100 µL syringe with one for larger volumes or by using a continuous flow pump.

During testing, ANDeS successfully automated the collection of samples for real-life experimental procedures, eliminating the need for manual pooling. This significantly reduced sample collection time by approximately 90% and minimized human error. Automated droplet collection also enables the use of all spots in the DMA without the risk of merging and eliminates the need for chemical labels for sample identification.

The ANDeS design supports a wide range of arrays, from flat surface arrays to 3D formatted arrays and submerged arrays. As an open-format device, it is highly adaptable and can be modified to address specific tasks. This flexibility makes ANDeS a reliable tool for assays requiring the precise and specific collection of samples from a large population of droplets.

ANDeS, with its in-capillary collection strategy, offers a versatile and affordable solution for creating new alternatives to interface non-optical analytical devices with Droplet Array Chips.

3. Conclusions and Outlook

High-throughput droplet array-based assays are becoming increasingly common and popular across a variety of disciplines. However, the development of tools and equipment capable of interfacing with this format has not kept pace with the rapid adoption of miniaturized assays. Although the feasibility of adopting standardized protocols from platforms such as the 384-well plate (which offers 3.5 experiments per square centimeter in µL volumes) to a miniaturized platform like the DMA (which offers from 0.4 to 31.8 experiments per square centimeter in nL-pL volumes) has been demonstrated, there is still a clear lack of tools available to adapt this miniaturization format to broader applications.

This work focuses on creating new methods for the manipulation, control, and integration of the DMA platform into conventional large-scale environments. The objective is for these strategies to extend and accelerate the adoption of this platform across more disciplines, allowing them to benefit from the advantages that the DMA provides in high-throughput experimentation based on nanoliter droplets. The need for reliable, accurate, fast, and parallel droplet handling is evident, and it is clear that manual droplet handling at this level of miniaturization is impractical, if not impossible. This shortcoming slows down the adoption of this format across various disciplines, which could greatly benefit from the opportunities offered by the DMA.

The first part of this work focused on studying the evaporation behavior on the DMA platform, as controlling evaporation is essential due to the use of nanoliter volumes. Rapid evaporation can lead to significant experimental inconsistencies, bias in results, and the risk of losing valuable materials and samples. Through sophisticated theoretical models and simulations, it was possible to predict the evaporation rates of commonly used laboratory compounds on the DMA.

In addition, the importance of the topographical design of the DMA was demonstrated, particularly how the distance between droplets can affect the shielding effect, directly influencing the evaporation rate. Thanks to the flexibility of the DMA production method, as shown in *section 1.2.3*, we can use the array design to our advantage to control this phenomenon and achieve uniform or desired evaporation. Based on these results, a digital twin was developed to predict and control droplet behavior under specific conditions, taking into account environmental factors such as humidity and temperature. This digital twin was used as a showcase to predict droplet behavior on the DMA during an entire theoretical sample preparation experiment, including steps such as cell incubation and temperature-mediated lysis.

These results exemplify the potential of having a tool capable of predicting the viability of an experimental design before actual testing. These insights not only ensure more reliable and stable experimental setups but also help strategize the transition or adaptation of commonly performed assays on conventional platforms to the field of miniaturized high-throughput assays using the DMA. Furthermore, implementing this predictive model can optimize established processes on the DMA and protect valuable or rare samples, such as patient samples, by first verifying the feasibility of the experimental design without risking these samples. This predictive capability ensures that researchers can anticipate and mitigate potential issues related to evaporation and condensation, leading to more controlled and accurate experiments.

Once the key parameters for droplet control and preservation in the DMA were established, the focus shifted to developing a strategy for parallel manipulation of those hundreds of droplets contained in a DMA. Therefore, the second part of this work employed a strategy called "Sandwiching". This method allows simultaneous interaction with all **672 droplets** present in a DMA. By applying this strategy, it was possible to achieve applications previously impossible in the DMA, such as performing medium changes for cells housed in nanoliter droplets or manipulating cellular groups contained within them.

The results of this section (*section 2.2*) showed that using this method, it is possible to culture cell groups, such as spheroids, for extended periods on nanoliter droplets. This is achieved by enabling the simultaneous addition of nutrients and removal of metabolic contaminants. Additionally, the technique allows for the non-destructive and non-invasive transfer of hundreds of spheroids between droplets, as well as between different DMA formats. Furthermore, this strategy facilitates more complex and extended biological studies on a single DMA, capable, for example, of generating hundreds to thousands of different spheroid architectures on a glass slide half the size of an ID card. As a result, it presents significant opportunities to accelerate the incorporation of miniaturization through droplet arrays into various research fields, ranging from high-throughput drug screening on multi-spheroid structures to studies in microtissue engineering.

The final chapter of this thesis presents the development of the Automated Nanoliter Droplet Selection and Collection Device (ANDeS), designed for the precise manipulation and transfer of individual droplets. The aim is to interface the DMA with non-optical equipment that requires direct interaction with each droplet to deliver results. ANDeS allows for the precise selection and collection of nanoliter droplets using capillaries, which act as containers for subsequent transport and injection of samples into different devices. This also has potential for sample preparation within the capillary, eliminating undesirable factors such as evaporation and condensation of nanoliter samples.

This innovation addressed a major shortcoming previously existing for DMA technology. While optical analysis works reliably on DMA, non-optical methods were excluded due to the impossibility of collecting those samples for further analysis. In that section (*section 2.3.3*), the method was validated through a showcase experiment using a highly sensitive methodology. qPCR was chosen to identify possible cross-contaminations due to the serial collection of samples within the same capillary. The technique demonstrated that ANDeS could reliably transfer multiple droplets into its capillary without cross-contamination, maintaining sample integrity for subsequent analyses.

The results showed that ANDeS can bridge the gap between DMA and sophisticated analytical equipment, such as LC-MS/MS. Additionally, being open-source, it is highly adaptable to different droplet array formats and various protocols for sample preparation, preservation, and transport. These results provide guidance for adopting DMA in high-interest areas of study,

such as genomics, transcriptomics, and proteomics at the single-cell level, which are of significant interest at the time this thesis is being written. Platforms like DMA play an ideal and fundamental role due to their ability to compartmentalize biological samples at very small scales and in large groups of datapoints, which is essential for the development of these fields.

In summary, this thesis provides tools and methodologies to overcome the limitations of high-throughput nanoliter droplet array-based assays. By addressing critical challenges such as evaporation control, parallel handling, and droplet collection and transfer, this work offers a comprehensive framework for expanding the experimental capabilities of DMA. The development of simple yet reliable techniques, such as the "sandwiching" method, along with the creation of an automated droplet collection and transport device, has shown great potential to tackle the chip-to-world problem.

Furthermore, it is hoped that this work will inspire other researchers to adopt creative approaches to overcome the emerging challenges in today's science, viewing them as opportunities for scientific innovation and discovery.

4. Materials and Methods

4.1. Droplet Microarrays

The droplet microarray DMA slides were purchased from Aquarray GmbH, Eggenstein-Leopoldshafen, Germany. All the steps of automatic droplet printing were carried out using a universal liquid dispenser (I-DOT, Dispendix GmbH, Germany). The droplets were automatically collected and relocated by ANDeS through a fused silica capillary (75µm i.d., 360µm o.d.; CS-Chromatographie Service GmbH, Langerwehe, Germany).

4.2. Preparation of HEMA-EDMA Slides

An uncoated Nexterion glass slide (Schott AG, Germany) underwent activation using a UVO cleaner (Jetlight Co. Inc., CA) for 10 minutes. Following activation, 150 µL of a modification mixture containing 20% 3-(trimethoxysilyl)propyl methacrylate in ethanol was applied onto the slide, which was then covered with another activated glass slide. The solution was evenly

distributed between the two slides, ensuring the removal of all bubbles, and allowed to react for 30 minutes. This functionalization process was repeated twice, followed by washing with acetone and drying with a nitrogen gun. The nanoporous poly(2-hydroxyethyl methacrylate-co-ethylene dimethacrylate) (HEMA-co-EDMA) polymerization mixture was prepared with the following components: 24 wt% 2-hydroxyethyl methacrylate (HEMA), 16 wt% ethylene dimethacrylate (EDMA), 12 wt% 1-decanol, 48 wt% cyclohexanol, and 0.4 wt% 2,2-dimethoxy-2-phenylacetophenone (DMPAP). Subsequently, 15-30 μL of the polymerization mixture was pipetted onto a fluorinated glass slide, and a modified glass slide was placed on top, allowing the mixture to spread evenly without forming air bubbles. These sandwich-like slides were then exposed to UV radiation (260 nm wavelength) for 20 minutes at an intensity of 10 mW/cm2. After irradiation, the slides were separated and washed with ethanol, followed by immersion in ethanol for several hours.

4.3. Liquids and Cell Dispensing

The pressure-based non-contact liquid dispenser, I-DOT One (Dispendix GmbH, Germany), was utilized for dispensing liquids and cell suspensions at specified cell densities. DMA slides (catalog numbers: G-np-102, G-np-201, and G-np-202) were procured from Aquarray GmbH (Eggenstein-Leopoldshafen, Germany). To prevent droplet evaporation during printing, a humidity level of 70% was maintained via an integrated humidifier.

4.4. Evaporation Experiments

Evaporation processes were observed using a KEYENCE Fluorescence Microscope BZ-X810 (Keyence Corporation) for top views and a Krüss DSA 25 contact angle goniometer for side views. ImageJ software (National Institutes of Health) was used to measure droplet heights and contact angles, with the scale based on the spot dimensions.

The temperature and humidity were measured using the DHT22 sensor (Adafruit Industries LLC) controlled by the Arduino UNO Rev3 microcontroller board (Arduino). The ambient relative humidity H and ambient temperature T are, respectively, $36 \pm 2\%$ and $25 \pm 1.2°C$, unless specified otherwise.

4.5. pH Indicators

A pH scale (6.0–9.5) and sample ($pH = 7.4$) were prepared with DMEM without phenol red using Cresol red (Supelco Inc) by a Mettler Toledo FE20/EL20 pH Meter (Mettler Toledo).

Afterward, the solutions were dispensed on 1.4 mm Ø spots DMA at a volume of 1.4 µL. Thereafter, the DMA was placed in a CanoScan8800F (Canon) to take an image of the pH scale and samples. The images have 3165 and 6178 pixels for width and height, respectively, and the horizontal and vertical resolutions are both 6400 dpi. The scanning speeds for 300 and 4800 dpi are 1.0 and 12.1 ms/line, respectively. Next, the DMA was left to evaporate inside the scanner and images of this process were taken every 5 min. Finally, the intensity of the color for the evaporating droplet was measured using Gridscreener software,50 which allows determination of the correlation of the initial color's mean intensity of the pH scale with the mean intensity variation of the samples upon evaporation. In parallel, a replicate of the same test was monitored using a goniometer to measure the evaporating droplet height at each point. The humidity and temperature inside the scanner and the goniometer were monitored using the DHT22 sensor.

4.6. Computational Simulation and Models

The simulations were performed using the PACE3D software package, which is designed for large-scale parallel simulations of phase transformation processes and microstructure formation in multicomponent and multiphase material systems (Karlsruhe Institute of Technology, Germany).

4.7. Cell Culture

HeLa CCL2 and HEK 293T cells were cultured in Dulbecco's Modified Eagle Medium (DMEM) (Gibco, Life technologies, Germany), supplemented with 10% fetal bovine serum (Gibco, Life technologies, Germany) and 1% penicillin/streptomycin (Life technologies, USA). Cells were split every 2-3 days until a cell density of 2×10^5 cells/ml was achieved.

4.8. Cell Culture on DMA

Before seeding cells on DMA, slides were sterilized with ethanol for 10 minutes and allowed to dry for 45 minutes under a clean bench. The cells were then dispensed onto the DMA at a density of 5×10^4 cells/ml (~15 cells/drop) in 300 nL per spot. Subsequently, the DMA was placed in a cell incubator. To prevent evaporation during culture, a wet humidifier pad was inserted into the lid of the Petri dish, and the Petri dish was filled with 10 ml of PBS.

4.9. 3D Cell Culture on DMA

To minimize cell adhesion on the DMA, each spot on the DMA slide was coated with 50 nL of Anti-Stick Rinse Solution (Stemcell Technologies Inc., Canada). Before coating, the DMA slides were immersed in ethanol for 10 minutes to ensure their sterility. Afterward, the DMA slides were placed on a clean bench to dry for 10 minutes. Subsequently, the slide spots were primed with 100 nL of anti-adhesion rinsing solution using the I-DOT One non-contact liquid dispenser. Following this, the DMA slides were again left to dry on a clean bench for another 10 minutes before being used for 3D cell culture.

For 3D cell culture, 200 nL droplets containing a suspension of HEK 293 cells at a density of 1×10^6 cells/ml (~200 cells/droplet) were dispensed onto the DMA. To facilitate 3D spheroid formation, the DMA slide was immediately inverted after printing and placed on a specially designed 3D printed table, allowing the cell culture inside to form hanging droplets. The cells were then cultured for 48 hours to form spheroids. To prevent evaporation during culture, a wet humidifier pad was inserted into the lid of the Petri dish, and the Petri dish was filled with 10 ml of PBS.

4.10. mRNA Extraction

The Cells-to-cDNA protocol was adapted and modified to accommodate suspension cells in this study. The original protocol, designed for adherent cells (Hela-CCL2) , was adjusted to effectively synthesize cDNA from 400 SU-DHL-4 suspension cells printed per spot on the 672 spot DMA slide. The modifications incorporated into the protocol ensured the successful capture and processing of suspension cells, allowing for accurate cDNA synthesis and downstream analysis. The cells undergo lysis, followed by mRNA extraction and conversion into single-stranded cDNA for each spot. Subsequently, the collected samples are amplified using Terra PCR master mix (Takara Bio, Japan) to generate double-stranded cDNA. Quality control of the cDNA is performed, and the concentration of the obtained cDNA is measured using the NanoDrop One microvolume UV-Vis spectrophotometers (Thermo fisher scientific Inc., USA) and checked for the cDNA quality via Agilent Bioanalyzer (Agilent technologies Inc., USA). As a proof of concept, this experimental setup is designed to showcase the feasibility of the ANDeS. The previously synthesized cDNA is reprinted via a universal liquid dispenser (I-DOT, Dispendix GmbH, Germany) per spot with a total volume of 350 nL. Then

cDNA is collected using ANDeS and subsequently quantified to assess the expression of a specific gene of interest via qPCR.

4.11. qPCR Analysis

The cDNA droplets were collected from the capillary into a PCR microtube by using the ANDeS syringe pump. The capillary was attached to the microscope (Olympus CKX31, Japan) to monitor the movement of the droplets within the capillary ensuring that the droplets were collected completely in the previously chosen PCR tube. The qPCR was performed according to the manufacturer's protocol on a StepOne Real-time PCR system (Life Technologies GmbH, Germany). The GAPDH F & R primers (IDT) were utilized for this purpose. The Gotaq qPCR master mix (Promega GmbH, Germany), and the Biorad Thermal Cycler C1000 Touch™ (Thermo fisher scientific Inc., USA) was employed for the PCR amplification. The collected sample, with a total volume of 350 nL, is transferred into a qPCR tube along with the reagent mix to evaluate the expression of the GAPDH gene.

4.12. Droplet Height Measurement

Droplet height measurements were conducted using a DSA25 Drop Shape Analyzer (Krüss, Germany). Initially, 300 nL of deionized water was dispensed over the spots of a DMA.

4.13. Automated imaging and image analysis

The DMA slide was placed in a four-well plate (Thermo Scientific, USA), which was fixed in a standard microtiter plate holder for microscopy. Imaging was performed with the Keyence BZ-X810 microscope (Keyence, Japan). The stitching function was used to image the entire slides. Z-stacks of 50 slices were made to take into account cells in suspension in slightly different focal planes, as well as spheroids. Images of each spot were taken at 10× and 20× magnification, brightfield and fluorescence. The image analysis, such as cell counting and fluorescence detection, was carried out using ImageJ/Fiji (National Institutes of Health Inc, USA) and the software Gridscreener.

4.14. Statistical analysis

The measurement error for figure 25 was assessed by manually taking 10 measurements of a sample with predetermined drop height and length, respectively, using ImageJ/Fiji (National Institutes of Health Inc, USA). The confidence interval (95%; 1.960 $\sigma_{\bar{x}}$) was calculated using the values of the mean and standard deviation of the experimental samples taken on each case.

The droplet heights were transformed using the geometric approximation described in section 2.1 using RStudio: Integrated Development Environment for R (Posit Inc, USA).

The measurement error for figure 26 and 27 was assessed by manually taking 10 measurements of a sample with predetermined drop height and length, respectively, using ImageJ/Fiji (National Institutes of Health Inc, USA). The confidence interval (95%; 1.960 $\sigma_{\bar{x}}$) was calculated using the values of the mean and standard deviation of the experimental samples taken on each case. In figure 27 and 28 the mean and standard deviation were calculated from the raw data obtained from the StepOne Real-time PCR system (Life Technologies GmbH, Germany). The sample contamination percentages in figure 27 and the empirical model to describe $Flow$ (figure 24) were calculated using RStudio: Integrated development environment for R (Posit Inc, USA). The calculations and plots were computed using GraphPad Prism (Dotmatics Inc, USA).

4.15. Desing of Sandwiching Adapter

An alignment frame was designed and fabricated to facilitate the alignment and sandwiching of the DMA slides. This frame was designed to hold the slides in place, preventing any movement during the sandwiching process. It ensured precise alignment of both slides in the XY plane relative to each other, guaranteeing accuracy during the procedure without the need for adjustments. The frame has a spacer to create a distance between the slides in the z-axis, allowing for consistent sandwiching with a predetermined distance of 0.4 mm between the slides (when using 672 spots DMA). Additionally, the design ensured compatibility with microscopy by maintaining no distance between the bottom surface of the frame and the lower DMA slide. This feature enabled direct microscopy within the frame, facilitating observation and analysis. This alignment frame was designed with Autodesk Fusion 360 (Autodesk, USA) and sliced on the Chitubox slicer (CBD Technology Co., China). The chosen printing parameters were a base layer exposure time of 20 s for the first 5 layers and a body layer exposure time of 2.5 s. The chosen layer height was 50µm per layer. The model was positioned upright on the build plate. Its Y-Z face was placed parallel to the build plate, with the X-axis vertical and perpendicular to the build plate. (X = Width, Y = Length, Z = Thickness) The DLP 3D printer used for fabrication was the Anycubic Photon D2 (Anycubic, China) with Siraya Tech Blu-Tough resin (Siraya, Taiwan). After printing, the model was washed in 70% ethanol for 10 minutes to remove uncross linked resin and finally post-cured in a 405 nm light for 20

minutes (Anycubic Wash and Cure 3.0 (Anycubic, China)) to ensure a high and homogeneous degree of crosslinking throughout the model.

4.16. Parallel Medium Replenishment on Individual Droplets

The HEMA-EDMA slide underwent sterilization using 70% alcohol and was left to air-dry under a clean bench for approximately 10 minutes. Subsequently, the DMA slide containing spheroids was secured beneath the sandwiching adapter, while the HEMA-EDMA slide was positioned above it, forming a “sandwich” structure with the DMA slide and droplets in between. Gentle pressure applied to the HEMA-EDMA facilitated the transfer of culture medium from the DMA with spheroids to the HEMA-EDMA slide. Afterwards, the DMA was placed on the I-DOT One non-contact dispenser to add 150 nL of medium on top. Finally, it was returned to the petri dish containing the humidity pads and taken to the cell incubator.

4.17. Parallel Manipulation of Cell Spheroids

Cell spheroids were cultured on two DMA plates using the experimental approach described previously. One DMA plate was positioned below the sandwiching adapter, while the other was placed above it, enabling the droplets from both DMA plates to come into contact. This setup facilitated the transfer of cells from the DMA plate positioned on top to the one secured below, driven by gravity.

4.18. Collection of Spheroids

Following incubation, the merged spheroids were transferred into a 10 cm culture dish containing 10 mL of medium. The DMA was carefully placed with the side containing the spheroids facing the liquid surface of the medium. The DMA was gently placed by hand onto the medium's surface, allowing the spheroids to pass from the droplets on the DMA into the dish by gravity within seconds. After waiting for the spheroids to settle, the supernatant was carefully removed. The spheroids were then transferred into the wells of a 384-well plate using a 1 mL pipette for further observation.

4.19. Design of the Automated Nanoliter Droplet Selection and Collection Device

The nano droplet manipulator is a Cartesian plane motion system composed of open-source linear rails, carriages and transmissions (OpenBuilds Inc., New Jersey, USA), to which a syringe pump removed from a Micro Fraction Collector (Dionex Softron GmbH, Germering,

Germany) was integrated to the system. This pump is equipped with a 100 µL 700 Series Syringe (Hamilton Inc., Reno, USA) coupled by applying reducing unions to a fused silica capillary (75 µm i.d., 360 µm o.d.; CS-Chromatographie Service GmbH, Langerwehe, Germany), which is fitted to the Z-axis using a 3D printer hot-end extruder (400 µm i.d; Shenzhen Redrex Technology Co., Ltd., Shenzhen, China) serving as a pipetting nozzle.

Nema 17 stepper (OpenBuilds Inc, New Jersey, USA) motors drive the 8 mm metric acme lead screws (OpenBuilds Inc, New Jersey, USA) of each axis and supply rotary power to the syringe pump assembly. These motors have a step angle of 1.8° per revolution, equivalent to 200 steps for one complete revolution. A4988 stepper motor drivers (Pololu Corporation, Nevada, USA) synchronize the rotation of each motor according to the pace and direction signals sent from the Raspberry Pi 4 model B (Raspberry Pi Foundation, Cambridge, England) through the Reprap Arduino Mega Pololu Shield 1.4 (ICQUANZX, Hong Kong, China).

The DMAs holder and adaptations were designed using Autodesk Fusion 360 (San Rafael, California) and produced on 3D printers by Creabis GmbH, Germany.

4.20. Motion Characterization

To determine the motion characteristics of ANDeS, each axis was tested by moving from a given starting position, then moving 100 mm for the X and Y axes and 50 mm for the Z axis. The movement from the start point to the end point and vice versa was measured with a Mitutoyo 530-122 vernier caliper with a resolution of 0.02 mm (Mitutoyo, Kawasaki, Japan).

4.21. Droplet Collection and Transfer

The droplet microarray DMA slides were purchased from Aquarray GmbH, Eggenstein-Leopoldshafen, Germany. All the steps of automatic droplet printing were carried out using a universal liquid dispenser (I-DOT, Dispendix GmbH, Germany). The droplets were automatically collected and relocated by ANDeS through a fused silica capillary (75µm i.d., 360µm o.d.; CS-Chromatographie Service GmbH, Langerwehe, Germany). The drop height videos and pictures were taken with a x4 objective (Nikon x4 Plan Apo NA 0.20/20 mm) at 8-bit resolution. To measure the samples inside the capillaries, a Keyence BZ-9000 microscope (Keyence, Osaka, Japan) was used. The data analysis was carried out using ImageJ/Fiji (National Institutes of Health Inc, USA), GraphPad Prism (Dotmatics Inc, USA) and RStudio:

Integrated development environment for R (Posit Inc, USA). The experimental times were taken with a digital stopwatch (A1000RCG-8B, Casio, Japan).

The images with color drops were made with drops of blue pen ink (Pelikan 4001, Pelikan Holding AG, Germany).

4.22. Sample Transport and Storage

The sample storage, preservation at 5 °C and transport were conducted by collecting the samples within the capillary, which was closed afterwards using silicone septum (3mm, 9mm Ø, CS-Chromatographie Service GmbH, Germany) as plugs to avoid evaporation or leaking.

4.23. Creation of Figures

The creation of the figures was done with Biorender.com.

5. References

1. Krakos, A., *Lab-on-chip technologies for space research — current trends and prospects.* Microchimica Acta, 2023. **191**(1): p. 31.
2. Barcelos, M.C., et al., *The colors of biotechnology: general overview and developments of white, green and blue areas.* FEMS microbiology letters, 2018. **365**(21): p. fny239.
3. Dunn, D.A. and I. Feygin, *Challenges and solutions to ultra-high-throughput screening assay miniaturization: Submicroliter fluid handling.* Drug Discovery Today, 2000. **5**: p. S84-S91.
4. Freese, T., et al., *The relevance of sustainable laboratory practices.* RSC Sustainability, 2024. **2**(5): p. 1300-1336.
5. Clomburg, J.M., A.M. Crumbley, and R. Gonzalez, *Industrial biomanufacturing: The future of chemical production.* Science, 2017. **355**(6320): p. aag0804.
6. Estevez-Torres, A., et al., *Carbon footprint and mitigation strategies of three chemistry laboratories.* Green Chemistry, 2024. **26**(5): p. 2613-2622.
7. Capet, X. and O. Aumont, *Decarbonization of academic laboratories: On the trade-offs between CO2 emissions, spending, and research output.* Cleaner Environmental Systems, 2024. **12**: p. 100168.
8. Dittrich, P.S. and A. Manz, *Lab-on-a-chip: microfluidics in drug discovery.* Nature Reviews Drug Discovery, 2006. **5**(3): p. 210-218.
9. Duncombe, T.A., A.M. Tentori, and A.E. Herr, *Microfluidics: reframing biological enquiry.* Nat Rev Mol Cell Biol, 2015. **16**(9): p. 554-67.
10. More, D., et al., *An Update on Current Trend in Sample Preparation Automation in Bioanalysis: strategies, Challenges and Future Direction.* Critical Reviews in Analytical Chemistry: p. 1-25.
11. Mark, D., et al., *Microfluidic lab-on-a-chip platforms: requirements, characteristics and applications.* Chemical Society Reviews, 2010. **39**(3): p. 1153-1182.
12. Whitesides, G.M., *The origins and the future of microfluidics.* Nature, 2006. **442**(7101): p. 368-373.
13. Du, G.-S., et al., *Cell-Based Drug Combination Screening with a Microfluidic Droplet Array System.* Analytical Chemistry, 2013. **85**(14): p. 6740-6747.
14. Williams, S.M., et al., *Automated Coupling of Nanodroplet Sample Preparation with Liquid Chromatography–Mass Spectrometry for High-Throughput Single-Cell Proteomics.* Analytical Chemistry, 2020. **92**(15): p. 10588-10596.
15. Shembekar, N., et al., *Droplet-based microfluidics in drug discovery, transcriptomics and high-throughput molecular genetics.* Lab on a Chip, 2016. **16**(8): p. 1314-1331.
16. Popova, A.A., et al., *Miniaturized Drug Sensitivity and Resistance Test on Patient-Derived Cells Using Droplet-Microarray.* SLAS TECHNOLOGY: Translating Life Sciences Innovation, 2020. **26**(3): p. 274-286.
17. Weibel, D.B., W.R. Diluzio, and G.M. Whitesides, *Microfabrication meets microbiology.* Nat Rev Microbiol, 2007. **5**(3): p. 209-18.
18. Pattanayak, P., et al., *Microfluidic chips: recent advances, critical strategies in design, applications and future perspectives.* Microfluid Nanofluidics, 2021. **25**(12): p. 99.
19. Moragues, T., et al., *Droplet-based microfluidics.* Nature Reviews Methods Primers, 2023. **3**(1): p. 32.
20. Pattanayak, P., et al., *Microfluidic chips: recent advances, critical strategies in design, applications and future perspectives.* Microfluidics and Nanofluidics, 2021. **25**(12): p. 99.
21. Hajam, M.I. and M.M. Khan, *Microfluidics: a concise review of the history, principles, design, applications, and future outlook.* Biomaterials Science, 2024. **12**(2): p. 218-251.
22. Ma, L., et al., *Droplet Microfluidic Devices: Working Principles, Fabrication Methods, and Scale-Up Applications.* Small Methods, 2024. **n/a**(n/a): p. 2301406.
23. Vladisaljević, G.T., *Droplet Microfluidics for High-Throughput Screening and Directed Evolution of Biomolecules.* Micromachines, 2024. **15**(8): p. 971.
24. Huang, E., et al., *Programmable droplet microfluidics for complex multistep bioassays.* Interdisciplinary Medicine, 2024. **2**(1): p. e20230026.
25. Zhu, P., X. Tang, and L. Wang, *Droplet generation in co-flow microfluidic channels with vibration.* Microfluidics and Nanofluidics, 2016. **20**(3): p. 47.
26. Shang, L., Y. Cheng, and Y. Zhao, *Emerging Droplet Microfluidics.* Chemical Reviews, 2017. **117**(12): p. 7964-8040.
27. Lee, J.M., et al., *Generation of tumor spheroids using a droplet-based microfluidic device for photothermal therapy.* Microsyst Nanoeng, 2020. **6**: p. 52.
28. Dimitriou, P., et al., *Droplet Microfluidics for Tumor Drug-Related Studies and Programmable Artificial Cells.* Glob Chall, 2021. **5**(7): p. 2000123.

29. Stucki, A., et al., *Droplet Microfluidics and Directed Evolution of Enzymes: An Intertwined Journey.* Angewandte Chemie International Edition, 2021. **60**(46): p. 24368-24387.
30. Lee, J.M., et al., *Generation of tumor spheroids using a droplet-based microfluidic device for photothermal therapy.* Microsystems & Nanoengineering, 2020. **6**(1): p. 52.
31. Simon, M.G. and A.P. Lee, *Microfluidic Droplet Manipulations and Their Applications*, in *Microdroplet Technology: Principles and Emerging Applications in Biology and Chemistry*, P. Day, A. Manz, and Y. Zhang, Editors. 2012, Springer New York: New York, NY. p. 23-50.
32. Saupe, M., et al., *Flexible Toolbox of High-Precision Microfluidic Modules for Versatile Droplet-Based Applications.* Micromachines, 2024. **15**(2): p. 250.
33. Han, W., et al., *A Perspective Review of Droplets and Bubbles Formation in Microfluidics.* Microgravity Science and Technology, 2024. **36**(3): p. 35.
34. Strutt, R., et al., *Open microfluidics: droplet microarrays as next generation multiwell plates for high throughput screening.* Lab Chip, 2024. **24**(5): p. 1064-1075.
35. Lin, X., et al., *High Throughput Blood Analysis Based on Deep Learning Algorithm and Self-Positioning Super-Hydrophobic SERS Platform for Non-Invasive Multi-Disease Screening.* Advanced Functional Materials, 2021. **31**(51): p. 2103382.
36. Song, Y., et al., *Mini-pillar microarray for individually electrochemical sensing in microdroplets.* Biosensors and Bioelectronics, 2020. **149**: p. 111845.
37. Aussillous, P. and D. Quéré, *Liquid marbles.* Nature, 2001. **411**(6840): p. 924-927.
38. Wang, S., et al., *Bioinspired Surfaces with Superwettability: New Insight on Theory, Design, and Applications.* Chemical Reviews, 2015. **115**(16): p. 8230-8293.
39. Strutt, R., et al., *Open microfluidics: droplet microarrays as next generation multiwell plates for high throughput screening.* Lab on a Chip, 2024. **24**(5): p. 1064-1075.
40. Feng, W., E. Ueda, and P.A. Levkin, *Droplet Microarrays: From Surface Patterning to High-Throughput Applications.* Advanced Materials, 2018. **30**(20): p. 1706111.
41. Feng, W., et al., *Surface Patterning via Thiol-Yne Click Chemistry: An Extremely Fast and Versatile Approach to Superhydrophilic-Superhydrophobic Micropatterns.* Advanced Materials Interfaces, 2014. **1**(7): p. 1400269.
42. Paulssen, D., et al., *Formation of Liquid–Liquid Micropatterns through Guided Liquid Displacement on Liquid-Infused Surfaces.* Advanced Materials Interfaces, 2018. **5**(18): p. 1800852.
43. Chang, B., et al., *Nanoliter deposition on star-shaped hydrophilic–superhydrophobic patterned surfaces.* Soft Matter, 2018. **14**(36): p. 7500-7506.
44. Bruchmann, J., et al., *Patterned SLIPS for the Formation of Arrays of Biofilm Microclusters with Defined Geometries.* Adv Healthc Mater, 2017. **6**(1).
45. Cui, H., et al., *Repurposing FDA-Approved Drugs for Temozolomide-Resistant IDH1 Mutant Glioma Using High-Throughput Miniaturized Screening on Droplet Microarray Chip.* Advanced Healthcare Materials, 2023. **12**(24): p. 2300591.
46. Popova, A.A., et al., *Facile One Step Formation and Screening of Tumor Spheroids Using Droplet-Microarray Platform.* Small, 2019. **15**(25): p. e1901299.
47. Cui, H., et al., *High-throughput formation of miniaturized cocultures of 2D cell monolayers and 3D cell spheroids using droplet microarray.* Droplet, 2023. **2**(1): p. e39.
48. Cui, H., et al., *Assembly of Multi-Spheroid Cellular Architectures by Programmable Droplet Merging.* Advanced Materials, 2021. **33**(4): p. 2006434.
49. Popova, A.A., et al., *Fish-Microarray: A Miniaturized Platform for Single-Embryo High-Throughput Screenings.* Advanced Functional Materials, 2018. **28**(3): p. 1703486.
50. Jothi Prakash, C.G. and R. Prasanth, *Approaches to design a surface with tunable wettability: a review on surface properties.* Journal of Materials Science, 2021. **56**(1): p. 108-135.
51. Mądry, K. and W. Nowicki, *Wetting between Cassie-Baxter and Wenzel regimes: a cellular model approach.* Eur Phys J E Soft Matter, 2021. **44**(11): p. 138.
52. Geyer, F.L., et al., *Superhydrophobic–Superhydrophilic Micropatterning: Towards Genome-on-a-Chip Cell Microarrays.* Angewandte Chemie International Edition, 2011. **50**(36): p. 8424-8427.
53. Benz, M., et al., *A combined high-throughput and high-content platform for unified on-chip synthesis, characterization and biological screening.* Nat Commun, 2020. **11**(1): p. 5391.
54. Young, T., *III. An essay on the cohesion of fluids.* Philosophical Transactions of the Royal Society of London, 1805. **95**: p. 65-87.
55. Siqveland, L.M. and S.M. Skjæveland, *Derivations of the Young-Laplace equation.* Capillarity, 2021. **4**(2): p. 23-30.
56. Malek, S.M.A., et al., *Evaluating the Laplace pressure of water nanodroplets from simulations.* Journal of Physics: Condensed Matter, 2018. **30**(14): p. 144005.

57. Wu, L., et al., *Designing Laplace Pressure Pattern for Microdroplet Manipulation.* Langmuir, 2018. **34**(2): p. 639-645.
58. Popova, A.A., et al., *Droplet-microarray on superhydrophobic–superhydrophilic patterns for high-throughput live cell screenings.* RSC Advances, 2016. **6**(44): p. 38263-38276.
59. Zhang, P., et al., *Printhead on a chip: empowering droplet-based bioprinting with microfluidics.* Trends in Biotechnology, 2024. **42**(3): p. 353-368.
60. Wiedmann, J.J., et al., *Nanoliter Scale Parallel Liquid–Liquid Extraction for High-Throughput Purification on a Droplet Microarray.* Small, 2023. **19**(9): p. 2204512.
61. Höpfner, J., M. Brehm, and P.A. Levkin, *Palladium-Catalyzed Combinatorial Synthesis of Biphenyls on Droplet Microarrays at Nanoliter Scale.* Small, 2024. **20**(4): p. 2304325.
62. Chakraborty, S., et al., *"Cells-to-cDNA on Chip": Phenotypic Assessment and Gene Expression Analysis from Live Cells in Nanoliter Volumes Using Droplet Microarrays.* Advanced Healthcare Materials, 2022. **11**(12): p. 2102493.
63. Sun, Q., et al., *Surface charge printing for programmed droplet transport.* Nat Mater, 2019. **18**(9): p. 936-941.
64. Zhu, Y., et al., *Nanodroplet processing platform for deep and quantitative proteome profiling of 10–100 mammalian cells.* Nature Communications, 2018. **9**(1): p. 882.
65. Popova, A.A., et al., *Droplet-Array (DA) Sandwich Chip: A Versatile Platform for High-Throughput Cell Screening Based on Superhydrophobic–Superhydrophilic Micropatterning.* Advanced Materials, 2015. **27**(35): p. 5217-5222.
66. Leduc, A., et al., *Massively parallel sample preparation for multiplexed single-cell proteomics using nPOP.* bioRxiv, 2023.
67. Erbil, H.Y., G. McHale, and M.I. Newton, *Drop Evaporation on Solid Surfaces: Constant Contact Angle Mode.* Langmuir, 2002. **18**(7): p. 2636-2641.
68. Schönfeld, F., et al., *Evaporation dynamics of sessile liquid drops in still air with constant contact radius.* International Journal of Heat and Mass Transfer, 2008. **51**(13): p. 3696-3699.
69. Yu, Y.-S., Z. Wang, and Y.-P. Zhao, *Experimental and theoretical investigations of evaporation of sessile water droplet on hydrophobic surfaces.* Journal of Colloid and Interface Science, 2012. **365**(1): p. 254-259.
70. Wu, Y., *Droplet wetting on chemically and mechanically structured surfaces*. 2021, Karlsruher Institut für Technologie (KIT).
71. Popova, A.A., et al., *Simple assessment of viability in 2D and 3D cell microarrays using single step digital imaging.* SLAS Technology, 2022. **27**(1): p. 44-53.
72. De Angelis, F., et al., *Breaking the diffusion limit with super-hydrophobic delivery of molecules to plasmonic nanofocusing SERS structures.* Nature Photonics, 2011. **5**(11): p. 682-687.
73. Jung and H.-Y. Kwak, *Separation of Microparticles and Biological Cells Inside an Evaporating Droplet Using Dielectrophoresis.* Analytical Chemistry, 2007. **79**(13): p. 5087-5092.
74. Seifermann, M., et al., *High-Throughput Synthesis and Machine Learning Assisted Design of Photodegradable Hydrogels.* Small Methods, 2023. **7**(9): p. 2300553.
75. Liu, Y., et al., *Droplet Microarray Based Screening Identifies Proteins for Maintaining Pluripotency of hiPSCs.* Advanced Healthcare Materials, 2022. **11**(18): p. 2200718.
76. Lei, W., et al., *Droplet Microarray as a Powerful Platform for Seeking New Antibiotics Against Multidrug-Resistant Bacteria.* Advanced Biology, 2022. **6**(12): p. 2200166.
77. RamalloGuevara, C., et al., *Fast Nanoliter-Scale Cell Assays Using Droplet Microarray–Mass Spectrometry Imaging.* Advanced Biology, 2021. **5**(3): p. 2000279.
78. Brehm, M., et al., *Nanomolar Synthesis in Droplet Microarrays with UV-Triggered On-Chip Cell Screening.* Small, 2020. **16**(10): p. 1905971.
79. Zhang, H., et al., *High-Density Droplet Microarray of Individually Addressable Electrochemical Cells.* Analytical Chemistry, 2017. **89**(11): p. 5832-5839.
80. Gómez, J.E.U., et al., *ANDeS: An automated nanoliter droplet selection and collection device.* SLAS Technology, 2024. **29**(1): p. 100118.
81. Bachler, S., et al. *Microfluidic platform enables tailored translocation and reaction cascades in nanoliter droplet networks*. Communications biology, 2020. **3**, 769 DOI: 10.1038/s42003-020-01489-w.
82. Woo, J., et al., *High-throughput and high-efficiency sample preparation for single-cell proteomics using a nested nanowell chip.* Nature Communications, 2021. **12**(1): p. 6246.
83. Küster, S.K., et al., *Screening for Protein Phosphorylation Using Nanoscale Reactions on Microdroplet Arrays.* Angewandte Chemie International Edition, 2015. **54**(5): p. 1671-1675.
84. Ruszczak, A., et al., *Physicochemical Properties Predict Retention of Antibiotics in Water-in-Oil Droplets.* Analytical Chemistry, 2023. **95**(2): p. 1574-1581.

85. Li, Z.-Y., et al., *Nanoliter-Scale Oil-Air-Droplet Chip-Based Single Cell Proteomic Analysis.* Analytical Chemistry, 2018. **90**(8): p. 5430-5438.
86. Kelly, R.T., *Single-cell Proteomics: Progress and Prospects.* Mol Cell Proteomics, 2020. **19**(11): p. 1739-1748.
87. Khilifi, D., et al., *STUDY OF THE PHENOMENON OF THE INTERACTION BETWEEN SESSILE DROPS DURING EVAPORATION.* THERMAL SCIENCE, 2019. **23**(2): p. 1105-1114.
88. Schofield, F.G.H., et al., *The shielding effect extends the lifetimes of two-dimensional sessile droplets.* Journal of Engineering Mathematics, 2020. **120**(1): p. 89-110.
89. Chen, H., et al., *Predicting the lifetimes of evaporating droplets in ordered arrays.* Physics of Fluids, 2022. **34**(8): p. 082010.
90. Nguyen, T.A.H. and A.V. Nguyen, *On the Lifetime of Evaporating Sessile Droplets.* LANGMUIR, 2012. **28**(3): p. 1924-1930.
91. Sáenz, P.J., et al., *Dynamics and universal scaling law in geometrically-controlled sessile drop evaporation.* NATURE COMMUNICATIONS, 2017. **8**.
92. Yue, P., et al., *A diffuse-interface method for simulating two-phase flows of complex fluids.* Journal of Fluid Mechanics, 2004. **515**: p. 293-317.
93. Wu, Y.A.-O., et al., *How do chemical patterns affect equilibrium droplet shapes?* (1744-6848 (Electronic)).
94. Cahn, J.W. and J.E. Hilliard, *Free Energy of a Nonuniform System. I. Interfacial Free Energy.* The Journal of Chemical Physics, 1958. **28**(2): p. 258-267.
95. Mostinsky, I., *Diffusion Coefficient. A-to-Z Guide to Thermodynamics.* Heat and Mass Transfer, and Fluids Engineering, http://www.thermopedia. com/de/content/696, 2006.
96. Smith, J., W. McCabe, and e. Peter Harriott, *Unit Operations of Chemical Engineering*. 2004: McGraw-Hill Education.
97. Yujin, S., et al., *Direct measurements of adhesion forces of water droplets on smooth and patterned polymers.* Surface Innovations, 2018. **6**(1–2): p. 93-105.
98. Popova, A.A., et al., *Evaluation of the Droplet-Microarray Platform for High-Throughput Screening of Suspension Cells.* SLAS Technol, 2017. **22**(2): p. 163-175.
99. Nagy, N., *Contact angle determination on hydrophilic and superhydrophilic surfaces by using r–θ-type capillary bridges.* Langmuir, 2019. **35**(15): p. 5202-5212.
100. Millet, O. and G. Gagneux, *A direct relation between bending energy and contact angles for capillary bridges.* Comptes Rendus. Mécanique, 2023. **351**(S2): p. 125-137.
101. Wang, Y., S. Michielsen, and H.J. Lee, *Symmetric and asymmetric capillary bridges between a rough surface and a parallel surface.* Langmuir, 2013. **29**(35): p. 11028-11037.
102. Mandsberg, N.K., J.A. Serna, and P.A. Levkin, *CART: Carrier-Based Actuatable and Reprogrammable Transport.* Advanced Functional Materials, 2024: p. 2406635.
103. Bezdenejnykh, N., J. Meseguer, and J. Perales, *Experimental analysis of stability limits of capillary liquid bridges.* Physics of Fluids A: Fluid Dynamics, 1992. **4**(4): p. 677-680.
104. Ayan, B., et al., *Aspiration-assisted freeform bioprinting of pre-fabricated tissue spheroids in a yield-stress gel.* Communications Physics, 2020. **3**(1): p. 183.
105. Daly, A.C., M.D. Davidson, and J.A. Burdick, *3D bioprinting of high cell-density heterogeneous tissue models through spheroid fusion within self-healing hydrogels.* Nature Communications, 2021. **12**(1): p. 753.
106. Jafari, J., et al., *Remote Control in Formation of 3D Multicellular Assemblies Using Magnetic Forces.* ACS Biomater Sci Eng, 2019. **5**(5): p. 2532-2542.
107. Byun, H., et al., *Magnetism-controlled assembly of composite stem cell spheroids for the biofabrication of contraction-modulatory 3D tissue.* Biofabrication, 2021. **14**(1).
108. Kuo, C.-T., et al., *Three-dimensional spheroid culture targeting versatile tissue bioassays using a PDMS-based hanging drop array.* Scientific Reports, 2017. **7**(1): p. 4363.
109. Place, E.S., N.D. Evans, and M.M. Stevens, *Complexity in biomaterials for tissue engineering.* Nature materials, 2009. **8**(6): p. 457-470.
110. Haraguchi, Y., et al., *Fabrication of functional three-dimensional tissues by stacking cell sheets in vitro.* Nature protocols, 2012. **7**(5): p. 850-858.
111. Brassard, J.A. and M.P. Lutolf, *Engineering stem cell self-organization to build better organoids.* Cell stem cell, 2019. **24**(6): p. 860-876.
112. Laschke, M.W. and M.D. Menger, *Life is 3D: boosting spheroid function for tissue engineering.* Trends in biotechnology, 2017. **35**(2): p. 133-144.
113. Birey, F., et al., *Assembly of functionally integrated human forebrain spheroids.* Nature, 2017. **545**(7652): p. 54-59.

114. Luo, J., et al., *Topography-Induced Cell Self-Organization from Simple to Complex Aggregates.* Small, 2019. **15**(15): p. 1900030.
115. Mirsaidov, U., et al., *Live cell lithography: using optical tweezers to create synthetic tissue.* Lab on a Chip, 2008. **8**(12): p. 2174-2181.
116. Zwi-Dantsis, L., et al., *Remote magnetic nanoparticle manipulation enables the dynamic patterning of cardiac tissues.* Advanced Materials, 2020. **32**(6): p. 1904598.
117. Nichol, J.W. and A. Khademhosseini, *Modular tissue engineering: engineering biological tissues from the bottom up.* Soft matter, 2009. **5**(7): p. 1312-1319.
118. Pedde, R.D., et al., *Emerging biofabrication strategies for engineering complex tissue constructs.* Advanced Materials, 2017. **29**(19): p. 1606061.
119. Cui, H., et al., *Assembly of Multi-Spheroid Cellular Architectures by Programmable Droplet Merging.* Adv Mater, 2021. **33**(4): p. e2006434.
120. Caraguel, C.G.B., et al., *Selection of a Cutoff Value for Real-Time Polymerase Chain Reaction Results to Fit a Diagnostic Purpose: Analytical and Epidemiologic Approaches.* Journal of Veterinary Diagnostic Investigation, 2011. **23**(1): p. 2-15.
121. Meyer, J.N., *QPCR: a tool for analysis of mitochondrial and nuclear DNA damage in ecotoxicology.* Ecotoxicology, 2010. **19**(4): p. 804-811.
122. Tian, Y., et al., *Development of a reverse-transcription droplet digital PCR method for quantitative detection of Cucumber green mottle mosaic virus.* Heliyon, 2023. **9**(2): p. e12643.